2015

Flow induced vibration on piezoelectric structures : theory, characterization, and application

Felix E. Ewere

FLOW-INDUCED VIBRATION ON PIEZOELECTRIC STRUCTURES: THEORY, CHARACTERIZATION, AND APPLICATION

by

FELIX E. EWERE

A DISSERTATION

Submitted in partial fulfillment of the requirements
for the degree of Doctor of Philosophy
in
The Department of Mechanical and Aerospace
to
The School of Graduate Studies
of
The University of Alabama in Huntsville

HUNTSVILLE, ALABAMA

2015

In presenting this dissertation in partial fulfillment of the requirements for a doctoral degree from The University of Alabama in Huntsville, I agree that the Library of this University shall make it freely available for inspection. I further agree that permission for extensive copying for scholarly purposes may be granted by my advisor or, in his/her absence, by the Chair of the Department or the Dean of the School of Graduate Studies. It is also understood that due recognition shall be given to me and to The University of Alabama in Huntsville in any scholarly use which may be made of any material in this dissertation.

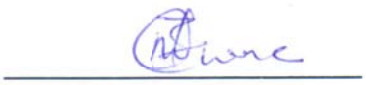

(Student)

11/01/2015

(Date)

DISSERTATION APPROVAL FORM

Submitted by Felix Ewere in partial fulfillment of the requirements for the degree of Doctor of Philosophy in Mechanical Engineering and accepted on behalf of the Faculty of the School of Graduate Studies by the dissertation committee.

We, the undersigned members of the Graduate Faculty of The University of Alabama in Huntsville, certify that we have advised and/or supervised the candidate on the work described in this dissertation. We further certify that we have reviewed the dissertation manuscript and approve it in partial fulfillment of the requirements for the degree of Doctor of Philosophy in Mechanical Engineering.

10/26/15
Dr. Gang Wang (Date) Committee Chair

10/26/15
Dr. Abdelkader Frendi (Date)

10/26/15
Dr. D. Brian Landrum (Date)

10/26/15
Dr. Q.H. Ken Zuo (Date)

Huang Wenzhang 10/27/15
Dr. Wenzhang Huang (Date)

11/3/15
Dr. Keith Hollingsworth (Date) Department Chair

11/06/15
Dr. Shankar Mahalingam (Date) College Dean

11/13/15
Dr. David Berkowitz (Date) Graduate Dean

ABSTRACT

The School of Graduate Studies
The University of Alabama in Huntsville

Degree: Doctor of Philosophy

College/Department: Engineering/Mechanical and Aerospace Engineering

Name of Candidate: Felix E. Ewere

Title: Flow-Induced Vibration on Piezoelectric Structures:
Theory, Characterization, and Application

Harvesting energy using piezoelectric transduction has focused on vibration-based types that rely on ambient vibrations. The challenge is to identify a consistent vibration source which is essential for uninterrupted power. Wind energy can provide a reliable and sustained source of vibration to achieve these energy harvesting goals if flow-induced vibration on piezoelectric structures is carefully explored. In this dissertation, flow-induced vibration on piezoelectric structures is investigated based on the galloping piezoelectric energy harvester (GPEH) concept. A GPEH is composed of a cantilevered piezoelectric beam with a tip bluff body. Self-excited vibration is induced when the tip bluff body is subjected to airflow. Then, the piezoelectric materials can convert the mechanical energy into electrical energy.

In order to understand the underlying physics, nonlinear coupled aero-electro-mechanical models are developed in which both geometric and material

nonlinearities are considered. Dimensionless formulation is adopted so that it is convenient to conduct scaling and performance comparison of different galloping piezoelectric devices. Analytical approximate approach is employed to solve the nonlinear coupled equations using the Krylov-Bogoliubov method. This ensures that system parameters such as galloping velocity, limit cycle oscillation (LCO) amplitude, transient period, and harvested energy are determined accordingly and presented in an explicit form. Additionally, numerical studies are conducted using COMSOL Multiphysics.

Several GPEH prototypes were fabricated. The baseline prototype is composed of a bimorph piezoelectric cantilever beam with a square cross-section bluff body. Subsequently, improved designs including addition of an impact bump stop to improve fatigue life and a bio-inspired tip bluff body borrowed from tubercles on flippers of the humpback whale. Comprehensive tests were conducted in a subsonic wind tunnel to determine system damping, electrical response, and LCO amplitude data. An optimal bump stop configuration was determined from tests that showed a significant reduction in LCO amplitude but with less effect on harvested voltage. Also, results from tests with the bio-inspired bluff body reveal the protuberances can be used as a passive control scheme to tune galloping velocity which hitherto depended on system damping and the shape of the bluff body cross-section.

Moreover, measured data was used to validate model predictions. Finally, an airflow sensor prototype was developed to demonstrate an application of the GPEH concept.

In summary, flow-induced vibration on piezoelectric structures is characterized in which model predictions on the GPEH were validated by experimental data with good agreement. It is expected that the current findings will advance the state-of-the-art of piezoelectric energy harvesting and lead to an innovative airflow sensor system.

Abstract Approval:

Committee Chair _____ 11/5/2015
Dr. Gang Wang (Date)

Departmental Chair _____ 11/5/15
Dr. Keith Hollingsworth (Date)

Graduate Dean _____ 11/13/15
Dr. David Berkowitz (Date)

ACKNOWLEDGEMENTS

I would like to sincerely and wholeheartedly thank my advisor, Dr. Gang Wang, for his kindness, guidance and encouragement throughout this process. His passion for research and promptness while reviewing my works is highly commendable. His personal concerns toward my well-being and candor are especially appreciated.

I would also like to thank my dissertation committee members; Drs. Abdelkader Frendi, D. Brian Landrum, Q.H. Ken Zuo, and Wenzhang Huang for making time in their busy schedules to serve on my committee. Their insightful comments and enthusiasm toward my research assisted immensely during my PhD work.

I was privileged to work with astute colleagues and a few undergraduate researchers in the Adaptive Structures Laboratory. I enjoyed the tough times and moments of "eureka" we shared. For this and for your assistance, I am very grateful.

I render heartfelt gratitude to members of the Ewere and Nwokejiezi families for their support and undying devotion towards my welfare. I also appreciate the care and concern from my friends through the years and the ones I have come to know in Huntsville. Thank you indeed.

Above all, I give thanks to the Almighty God - the source of everything in my life.

Finally, I offer an unreserved appreciation for the support from the College of Engineering and the Department of Mechanical and Aerospace Engineering. Thanks to the staff of MAE department; especially Ms. Claudia Meyering, for her charisma and support all through my graduate studies. I also thank Dr. Olufemi Agboola for introducing me to The University of Alabama in Huntsville.

TABLE OF CONTENT

LIST OF FIGURES

Figure **Page**

LIST OF TABLES

Table **Page**

NOMENCLATURE

b = width of base beam [m]

b_p = width of one piezoelectric layer [m]

d_{31} = piezoelectric constant [m/volt]

h = length of bluff body cross-section [m]

h_b = thickness of base beam [m]

h_p = thickness of one piezoelectric layer [m]

k_{31} = electromechanical coupling coefficient

l = height of bluff body [m]

m_b = mass per unit length of beam [kg/m]

m_p = mass per unit length of one piezoelectric layer [kg/m]

t = time [s]

w = beam transverse displacement [m]

C_p = capacitance of one piezoelectric layer [Farad]

D_3 = electric displacement in top piezoelectric layer across thickness [Coul./m^2]

$\bar{D}_3$ = electric displacement in bottom piezoelectric layer across thickness [Coul./m^2]

E_3 = electrical field intensity in top piezoelectric layer across thickness [Volt/m]

$\bar{E}_3$ = electrical field intensity in bottom piezoelectric layer across thickness [Volt/m]

E_b = base beam Young's modulus [Pa]

L = length of base beam [m]

L_b = length of piezoelectric section [m]

M_{tip} = Mass of bluff body [kg]

Q = charge [Coulomb]

S_{11}^E = piezoelectric compliance [m^2/N]

Y = reduced displacement

Y_0 = limit cycle oscillation amplitude

ξ = damping ratio

ε_{33}^S = piezoelectric permittivity measured at constant strain [Farad/m]

ε_{33}^T = piezoelectric permittivity measured at constant stress [Farad/m]

ε_b = normal strain of base beam

$\varepsilon_{p1}, \varepsilon_{p2}$ = normal stress in top and bottom piezoelectric layer, respectively

ρ_b = density of base beam [kg/m^3]

ρ_p = density of piezoelectric material [kg/m^3]

σ_{xx} = normal stress of base beam [Pa]

σ_{p1}, σ_{p2} = normal stress in top and bottom piezoelectric layer, respectively [Pa]

Θ = piezoelectric coupling term [volt/m]

ω = natural frequency [Hz]

Ω = galloping frequency [Hz]

τ = reduced time = ωt

η = mass parameter

β = non dimensional piezoelectric coupling term

α = non dimensional electric load

$\dot{(\,)}$ = $\frac{\partial(\,)}{\partial t}$

To the loving memory of the woman who gave me life:

Gladys Ulumma Ewere

Mother, Mentor, and role Model

It is the harmony of the diverse parts, their symmetry, their happy balance; in a word it is all that introduces order, all that gives unity, that permits us to see clearly and to comprehend at once both the ensemble and the details

- Henri Poincaré

Chapter 1: Introduction

1.1 Motivation and Objectives

The present dissertation explores the controlled use of aeroelastic instabilities on piezoelectric structures and its applications. Using piezoelectric materials as transducers to interchange electrical energy and mechanical strain have received numerous research interests in recent years due to its unique advantages over electromagnetic and electrostatic transduction in the micro (small) scale for powering micro-electromechanical systems (MEMS) devices and wireless sensors [1-3]. Available ambient vibrations as the source of mechanical energy have been used as seen in vibration-based energy harvesters (VBEH) [4-6]. However, such ambient sources of vibration, vital to achieve this energy harvesting goal are not always available. Thus to identify a reliable and sustained vibration source becomes a significant issue in real engineering applications. Wind energy could be an alternative reliable source if flow-induced vibration on structures is carefully explored [7].

This flow-induced piezoelectric energy harvesting system requires a multi-physics approach needed to characterize both mechanical and electrical responses. Ultimately, wind – a renewable source of energy – will be converted to electrical

energy which requires the coupling of three thrust areas as shown in Figure 1.1. Elastic forces derived from structures excited by aerodynamic forces are converted to electrical forces using piezoelectric materials. The challenge is to investigate the interaction of the coupled system and optimize the output for real engineering applications.

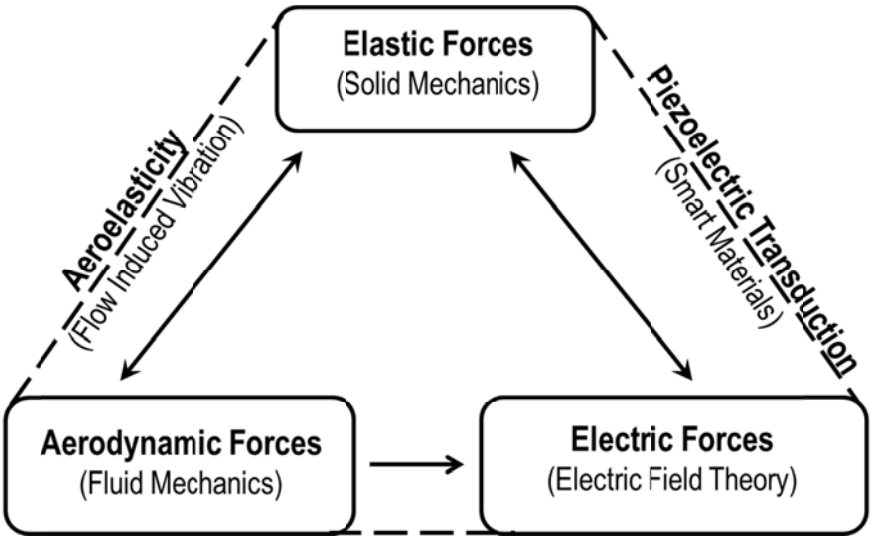

Figure 1.1: Thrust research areas

Therefore, this research work is motivated by the need for the development of a practical flow-induced piezoelectric energy harvester. The goal is to provide a reliable and self-sustained vibration source of power in remote areas for various applications by exploiting wind energy. Additionally, the characterized electrical signals can be used to relate the airflow initiating a sensing scheme that can determine fluid flow magnitude and direction from an array of sensors.

The objectives of this research work are listed below:

a. To fundamentally understand the underlying physics of flow-induced vibration on piezoelectric structures.
b. To characterize the behavior of the coupled system. Both analytical and numerical models are developed to study the behavior of this coupled system.
c. To develop prototypes and conduct comprehensive wind tunnel tests to evaluate fabricated prototype performance and validate model predictions.
d. To demonstrate the concept in engineering applications as an energy harvesting device and an airflow sensor.

1.2 State-of-the-art

1.2.1 Vibration-Based Energy Harvesters (VBEHs)

Vibration-based energy harvesters coupled with smart materials have concentrated on piezoelectric materials because of their high energy density. There have been numerous developmental efforts on using a cantilevered beam as the vibrating structure upon which the piezoelectric element is bonded. These devices range from MEMS scale [8-11] to macro-scale sizes [4-5, 12-13]. Erturk and Inman

provide a comprehensive discussion on the design, modeling, and experimentation of such vibration-based piezoelectric energy harvesters [6]. In practice, to maximize power output, a tip mass is attached to the free end of the cantilever to tune the natural frequency of the harvester to that of the excitation frequency. Tip mass effects on mode shapes and natural frequencies have been considered in reference [14-16].

As reviewed by Erturk and Inman [6], three approaches are typically used for the analysis of such VBEHs: (a) lumped parameter model, (b) the Rayleigh–Ritz method, and (c) distributed parameter model. Several efforts were pursued to yield an analytical representation based on the Euler–Bernoulli beam theory and linear piezoelectric constitutive equation [17-19]. Conventional finite element models (CFEMs) have also been developed for VBEHs [20-21]. However, the focus was on actuation using piezoelectric materials. A spectral finite element model (SFEM) for bimorph VBEHs was developed by Wang [22] based on both the Euler–Bernoulli and Timoshenko beam theories, in which the application and validation of each beam theory was demonstrated based on the beams slenderness ratio.

Mak *et al.* incorporated an impact bump stop into a cantilever VBEH to reduce the beam amplitude and the resulting bending stress [23]. This design results in a proportional reduction in both displacement and harvested voltage. To address the

limitation of harvesting energy only at the linear resonance, further improvements adopted include the use of external magnets and multiple bimorphs with different operating frequencies for enhanced broadband frequency response [24-26]. Therefore, it is very promising to provide a new way of powering small electronic components and remote sensors in mechanical, aerospace, civil, medical, and other applications using these vibration-based piezoelectric energy harvesters.

1.2.2 Flow-induced energy harvesters

Flow-induced vibration is able to provide an alternative vibration source in piezoelectric energy harvesting applications. Mehmood *et al.* investigated a piezoelectric energy harvester with a circular cylinder undergoing vortex-induced vibrations [27]. Numerical simulations were performed for different Reynolds numbers (Re) which covers the pre-synchronization, synchronization, and post-synchronization regimes. Other vortex-induced piezoelectric harvesting with circular cylinders has been discussed as well [28-29]. Bryant and Garcia proposed a novel device driven by aeroelastic flutter vibrations; the harvester composed of a piezoelectric beam with a flap undergoing limit cycle oscillations (LCOs) [30]. A piezoelectric airfoil was designed and tested by Erturk *et al.* [31], in which linear flutter velocity was predicted using a simple model with pitch and plunge degrees of freedom. De Marqui *et al.* developed a finite element model for a cantilevered

plate with surface bonded piezoelectric materials under airflow excitations [32]. Other aeroelastic flutter based piezoelectric harvesters have been discussed in literature [33-34].

Galloping piezoelectric energy harvesters (GPEHs) with D section and equilateral triangle tip bluff bodies were developed by Sirohi and Mahadik [35-36]. Numerical predictions were validated by experimental data and the equilateral triangular section shows better performance. To capture the output power trend for the GPEH with equilateral triangle cross-section, nonlinear analysis was performed by Abdelkefi *et al.* [37]. Their model coupled with a nonlinear spring showed best agreement with results of experiments performed by Sihori and Mahadik. Abdelkefi *et al.* also investigated a GPEH with square bluff body and the effects of Reynolds number on harvested power and onset of galloping were characterized [38]. It was shown that the harvested power at higher Reynolds number (i.e., Re $>$ 200) can be optimized by properly choosing the matching electrical load. Zhao *et al.* compared the effect of different tip mass sections on a GPEH [39]. Experiments were conducted for a square, 3/2 rectangle, 2/3 rectangle and equilateral triangle sections of equal weight and exposed length to incident wind. Harvested power based on these comparable geometries showed that the square section give the best performance.

All of the above research efforts build a solid foundation to understand the aero-electro-mechanical coupled energy harvester system. However, numerical solution approaches have been employed to predict the system performance in these works [16,35,37].

Thus, an analytical prediction model enables the efficient design and analysis of such flow-induced piezoelectric energy harvesters and also captures the underlying physics.

1.3 The proposed concept

In this dissertation, the galloping piezoelectric energy harvester (GPEH) concept is explored to understand the underlying physics of this coupled aero-electro-mechanical system. Both baseline GPEH and improved designs are proposed. The baseline GPEH is composed of a cantilever beam, surfaced bonded piezoelectric layers, and a square cross-section tip bluff body. The tip bluff body is used to induce the vibration when it is subjected to airflow. Then the mechanical strain on the piezoelectric beam is converted to electrical energy by the piezoelectric materials.

Similar to the stop bump applied by Mak *et al.* [23], to improve on baseline GPEH, an impact bump stop is introduced to alleviate beam stress. The goal is to

extend the beam fatigue life while harvesting similar power as the baseline and study its effects on harvested power and beam deflection.

Recently, focus on the bio-inspired passive control method inspired by the humpback whale flipper with rounded tubercles interspaced along its leading edge has increased [40-42]. Research works on the effects of protuberances on the leading edge of an airfoil aerodynamics have shown good performances even though detailed understanding of the underlying physics is still lacking. Increased lift, reduced drag, and delay of stall have been noticed to be why the whale can perform swift maneuvers easily [40-42].

In contrast, tubercles which are analogous to a wavy-leading edge on a bluff body have been studied primarily to reduce lift and drag forces thereby eliminate flow-induced vibration on structures [43-47]. Bearman and Owen performed experiments on rectangular cross-section bodies with spanwise sinusoidal form [43]. Tests were conducted at high Reynolds number of 4000 with a relative 30% reduction in drag noticed due to increased mean base pressure when compared to the equivalent straight body. Also drag reduced with increasing wave steepness and similar results obtained for bluff body with front only and both front and rear wavy surfaces indicate wavy trailing edges had minimal influence on the results. Extensive numerical study of a square cross-section prism with a spanwise waviness was

carried out by Darekar and Sherwin [44]. A parallel spectral element code was used to perform both two and three dimensional steady and unsteady simulations. Successive flow regimes defined as a function of dimensionless length scales were used to show progressive drag and lift reduction with reduced time and frequency. However, at low Reynolds number < 30 the same drag level for wavy and non-wavy cylinder was noticed. This spanwise waviness is also observed to suppress vortex shedding due to additional components of vorticity that appear in regions close to the inflection points of the wavy stagnation face where the spanwise vorticity is weakened.

Therefore, a bio-inspired tip bluff body is introduced to explore the effects of spanwise waviness on exploiting wind energy from galloping aeroelastic instability. Finally an airflow sensing scheme is developed to further demonstrate the application of the GPEH concept.

1.4 Original Contributions

This research work involves the fundamental understanding of flow-induced vibration on piezoelectric structures which requires a multi-disciplinary approach to conduct analysis, fabrication, and evaluation of the proposed GPEH concept. To this end, the original contributions of this study include:

i. Developed nonlinear coupled aero-electro-mechanical model for a galloping piezoelectric energy harvester;

ii. Derived analytical approximate solutions in which compact closed form representations allows for an efficient design and analysis;

iii. Carried out numerical verification analysis using COMSOL Multiphysics software;

iv. Fabricated various GPEH prototypes including baseline and improved prototypes with an impact bump stop and a bio-inspired bluff body;

v. Conducted comprehensive wind tunnel tests to evaluate fabricated prototypes in which voltage and LCO amplitude data were collected and also used to validate model predictions;

vi. Demonstrated the use of the GPEH concept as an energy harvesting device and also as a novel airflow sensing scheme to determine airflow magnitude and direction.

Current findings are expected to further the state of the art of piezoelectric energy harvesting. Reduced power requirements of small electronic components means this aero-electro-mechanical device can be used in such remote areas as; monitor cameras at the border and attached to birds for migration monitoring. Another potential application is using the consequent mechanical effects of

airflow on bluff body to relate air velocity. For example the miniature GPEH with the bio-inspired bluff body can be adopted as an airflow sensor which can provide both magnitude and direction measurements if an array of these sensors are deployed. These low-cost sensors can help with tornado monitoring where the destructive nature of high winds requires easily replaceable sensors at minimal cost.

1.5 Organization

The dissertation is organized as follows. Chapter 2 reviews piezoelectric beam energy harvesting concepts including the theory of piezoelectricity, piezoelectric materials, beam structural model and beam kinematics, flow-induced vibration and the bluff body aerodynamics. The GPEH model development is presented in Chapter 3 to discuss the governing equations and associated analytical approximate solutions. The developed GPEH model is able to predict harvested voltage, LCO amplitude, power, current, transient period, initiation of galloping, and the hysteresis response. Furthermore, both geometric and material nonlinearities are included in the model to improve the model prediction capability in order to capture beam large deflection and high electrical response in piezoelectric materials. Chapter 4 discusses GPEH prototype development and experimental setup. Comprehensive wind tunnel tests were conducted to characterize the

performance of various GPEH prototypes. Those measurements will be used to validate our model predictions as discussed in Chapter 5 for both numerical simulations using COMSOL Multiphysics software and analytical predictions. The applications of the proposed GPEH concept are discussed in Chapter 6. Sub-scaled prototypes are developed to demonstrate energy harvesting and airflow sensing applications. Finally, some concluding remarks and recommendations are given in Chapter 7.

Chapter 2: Background and Theory

The chapter presents a brief introduction to piezoelectric energy harvesting. The piezoelectric phenomenon is described and common piezoelectric materials are discussed. Both linear and nonlinear piezoelectric theories are presented. In order to capture the coupled system, structural and aerodynamic models are required. Subsequently, the beam model and kinematics are presented. Finally, a brief discussion on flow-induced vibration and bluff body aerodynamics is presented.

2.1 Piezoelectric Energy Harvesting

2.1.1 Piezoelectricity

Piezoelectricity means "pressure electricity", which is used to describe the coupling between mechanical and electrical behaviors of a material first discovered in quartz and Rochelle salt in 1880 by the brothers Jacques and Pierre Curie [48]. These crystals become electrically polarized when subjected to mechanical force known as the direct effect and when exposed to an electric field they become strained known as the indirect effect. Above the Curie point the crystals exhibit a simple cubic symmetry with no dipole moment while at temperatures below the Curie point they become anisotropic taking a tetragonal or rhombohedral symmetry with dipole moment. The dipoles in a macroscopic crystalline structure

are initially randomly oriented giving rise to a zero net polarization and negligible piezoelectric effect. Therefore, the material is given a polarizing treatment to initiate a state where the dipoles are oriented in the same direction known as the poling direction. This is done by exposing the ferroelectric material to a strong, direct current electric field below the Curie point which causes it to elongate. When the electric field is removed the domains now have the remanent (permanent) polarization and the dipoles are locked in near alignment [see Figure 2.1]. Therefore, mechanical compression or tension on the poled element changes the dipole moment creating a voltage. This generator action is used in fuel igniting devices, solid state batteries and as sensors. When a voltage is applied, the poled piezoelectric element will lengthen or shorten depending on the polarity of the applied voltage. This motor action is adapted to sound generating devices and as actuators.

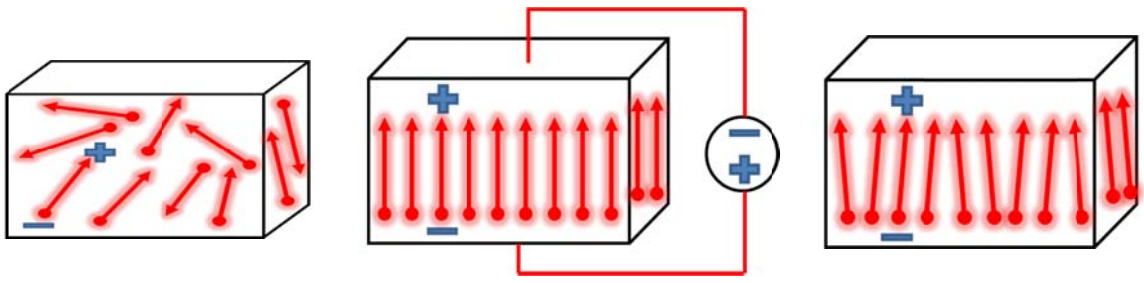

a **b** **c**

Figure 2.1: Poling process

2.1.2 Piezoelectric Materials

Piezoelectric materials occur mainly as crystals, polymers or ceramics. Crystals like Quartz (SiO2), Rochelle salt ($NaKC_4H_4O_6.4H_2O$) and the perovskite family with general formula XYO_3 have been investigated and used in numerous engineering applications especially as high quality electromechanical filters for high frequency use and in high environmental temperatures [49-51]. Natural organic substances like rubber, wool and hair are piezoelectric but with unsatisfactory properties to be used as electromechanical transducers. However strong piezoelectricity was found in the polymer $(\text{-}CH_2\text{-}CF_2\text{-})_n$ Polyvinylidene fluoride (PVDF) discovered by Heiji Kawai in 1969 [52]. This thin film flexible material shows large compliance which is suitable for headphones and speakers. Discovery of piezoelectric ceramics was the start of the modern history of piezoelectricity attributed to Shepard Roberts [49]. In 1947 he discovered that the ceramics of $BaTiO_3$ are piezoelectric under high DC field and in the state of remanent polarization. Research into ferroelectricity in ceramics of the perovskite family began with different compositions attempted, such as substitution of Ba with Pb; Sr, or Ca and Ti with Zr or Sn. A turning point was in 1954 when Bernard Jaffe and others found excellent piezoelectric performance in ceramics with composition near $Pb[Zr_{0.55}Ti_{0.45}]O_3$ [53]. A lead Zirconium Titanate (PZT) ceramic ($Pb[Zr_xTi_{1-}$

$_x]O_3$) (0≤x≤1)) first discovered at the Toyko Institute of Technology offer significantly better piezoelectric coefficients than PVDF and is the choice material used in this research work. PZT-5A and PZT-5H are the most commonly used engineering piezoelectric ceramic. This synopsis (2.1.1 & 2.1.2) is meant as an introduction into piezoelectric materials and is not sufficient to fully describe the field. Greater details will be found in literature [see reference 48- 53]

2.1.3 Energy Harvesting Application

Research on scavenging energy using piezoelectric transducers has received a lot of attention recently because advances in technology have led to reduced power needs of electronic components in the macro and micro scale. The basic concept is to convert ambient energy (usually vibration) to electricity via piezoelectric transduction. This power harvesting system can then be used to replace conventional power systems like batteries that have a limited operational life. Early pioneer Umeda *et al.* investigated the power generated due to impact when a free falling steel ball hits the top of a plate with a piezo-ceramic wafer attached to the bottom [54]. Their study used an electrical equivalence model to simulate the energy generated and also calculate the potential of the piezo-ceramic to transform mechanical energy into electrical power due to impact. Several other designs have been proposed for energy harvesting in literature [55-56]. The simplest

configuration is to use a cantilever as the core vibrating structure upon which these piezoelectric element are bonded as used in vibration based energy harvesters (VBEHs) [4-5]. Normally, the piezoelectric charge constants d_{31} and d_{33} are the two common modes used to couple polarization and mechanical strain for energy harvesting. Usually, the z axis (3 axis) is the poling direction; so the d_{31} mode will induce strain in direction 1 per unit electric field in direction 3 (thickness) while d_{33} mode means induced strain in direction 3 per unit electric field in direction 3 [see Figure 2.2]. In addition the surface bonded piezoelectric material can be a unimorph or bimorph. In the bimorph configuration, the top and bottom piezoelectric layers have identical geometry but can have different poling directions, that is, both series and parallel electrical arrangements are allowed [6]. The harvested AC power is rectified and stored in a capacitor [57-58] or used to recharge a discharged battery [59] until sufficient amount can be recovered to power the electronic device.

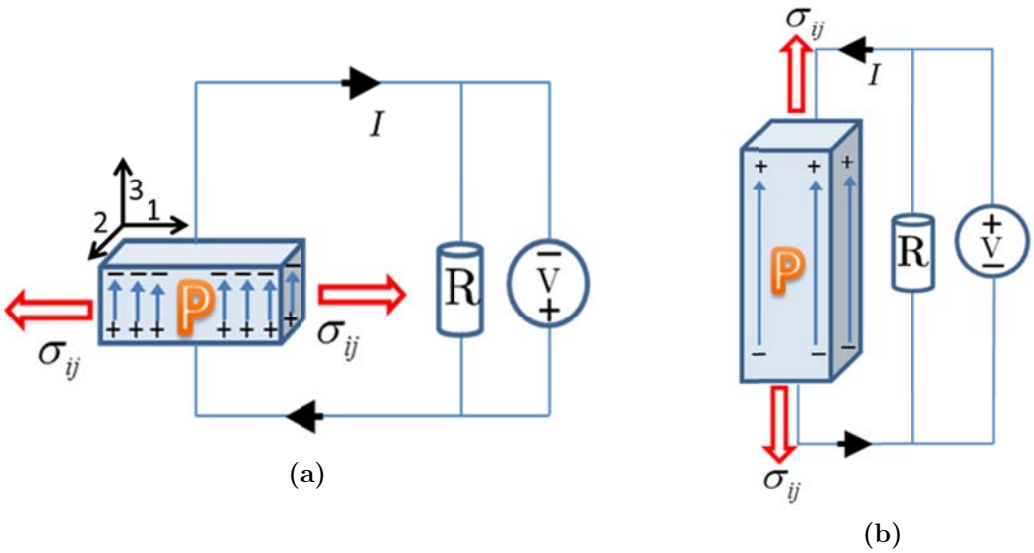

Figure 2.2: Direct effect (a) d_{31} (b) d_{33}

2.2 Theory of Piezoelectricity

2.2.1 Linear Piezoelectric Constitutive Theory

Generally, the linear conversion phenomenon is defined as one produced by the variation of two physical state variables that are linearly coupled [49]. Defining such variables as A *and* B, the free energy of the system can be defined uniquely by the homogenous quadratic equation as;

$$f(A,B) = \frac{1}{2}a_{11}A^2 + a_{12}AB + \frac{1}{2}a_{22}B^2 \tag{2.1}$$

The existence of the interaction is assumed by the non-vanishing aspect;

$$a_{12} = \left[\frac{\partial^2 f}{\partial A \partial B}\right]_{A,B=0} \tag{2.2}$$

Where A, B are extensive variables and $A = B = 0$ is an equilibrium

If we denote the intensive variables by X *and* Z respectively, then the exact differential becomes;

$$df = XdA + ZdB \tag{2.3}$$

Where $$X = \frac{\partial f}{\partial A} \quad and \quad Z = \frac{\partial f}{\partial B} \tag{2.4}$$

This leads to the constitutive relations given by a set of two equations;

$$X = a_{11}A + a_{12}B \quad and \quad Z = a_{12}A + a_{22}B \tag{2.5}$$

a_{11}, a_{22} are principal constants; therefore the coupling coefficient k is defined as;

$$k = \frac{a_{12}^2}{a_{11}a_{22}} \tag{2.6}$$

Note that the constitutive equation (2.5) although expressed with A, B as independent variables can be explicitly expressed with different sets of independent variables by simple arrangement. It can also be derived from a Taylor's expansion of X *and* Z with respect to A *and* B.

As given in Tiersten [60], the form of the electric enthalpy density, H in the linearized theory of piezoelectricity is;

$$H = \frac{1}{2}c_{ijkl}^{E} S_{ij} S_{kl} - e_{kij} E_k S_{ij} - \frac{1}{2}\varepsilon_{ij}^{S} E_i E_j \tag{2.7}$$

Where S_{ij} is the strain tensor, E_i is the electric field tensor, c_{ijkl}^{E}, e_{kij} and ε_{ij}^{S} are the elastic, piezoelectric and permittivity constants respectively. In general there are 21 independent elastic constants, 18 independent piezoelectric constants, and 6

independent dielectric constants. Also since $H = H(S_{ij}, E_i)$ from (2.4), the intensive variables (stress tensor and electric displacement tensor) are derived as follows;

$$\sigma_{ij} = \frac{\partial H}{\partial S_{ij}}, \qquad D_i = -\frac{\partial H}{\partial E_i} \tag{2.8}$$

This satisfies the necessary and sufficient condition for the existence of H , i.e.

$$\frac{\partial^2 H}{\partial S_{ij}\partial E_i} = \frac{\partial \sigma_{ij}}{\partial E_i} = -\frac{\partial D_i}{\partial E_i \partial S_{ij}} = \frac{\partial^2 H}{\partial E_i \partial S_{ij}} \tag{2.9}$$

Therefore, the fundamental form (e-form) of the linear constitutive equations for the unbounded piezoelectric continuum is obtained using (2.8) as,

$$\begin{aligned} \sigma_{ij} &= c^E_{ijkl} S_{kl} - e_{kij} E_k \quad - \quad \textit{Inverse effect} \\ D_i &= e_{ikl} S_{kl} + \varepsilon^s_{ik} E_k \quad - \quad \textit{Direct effect} \end{aligned} \tag{2.10}$$

As sensors, piezoelectric materials use the direct piezoelectric effect which is observed from Equation 2.10. If the applied external electric field is zero i.e. $E_k = 0$ the stress field causes an electric displacement to be generated. The converse happens in the inverse effect when the applied stress field is zero i.e. $S_{kl} = 0$; the electric field causes a stress field to be generated.

Alternate forms used for approximations under certain limiting circumstances are shown below;

$$\begin{aligned} S_{ij} &= s^E_{ijkl} \sigma_{kl} + d_{kij} E_k \\ D_i &= d_{ikl} \sigma_{kl} + \varepsilon^\sigma_{ik} E_k \end{aligned} \qquad \textit{(d-form)} \tag{2.11}$$

and

$$S_{ij} = s^{D}_{ijkl}\sigma_{kl} + g_{kij}D_k \qquad \textit{(g-form)} \qquad (2.12)$$
$$E_i = -g_{ikl}\sigma_{kl} + \beta^{\sigma}_{ik}D_k$$

and

$$\sigma_{ij} = c^{D}_{ijkl}S_{kl} - h_{kij}D_k \qquad \textit{(h-form)} \qquad (2.13)$$
$$E_i = -h_{ikl}S_{kl} + \beta^{s}_{ik}D_k$$

Where $d_{kij}, g_{kij}, h_{kij}$ are alternative forms of the piezoelectric constants, S^{E}_{ijkl} and S^{D}_{ijkl} are elastic compliance constants, and β^{σ}_{ik} and β^{S}_{ik} are the impermeability constants. The superscripts E, S, σ, D denote constants evaluated at constant electric field, constant strain, constant stress and constant electric displacement. Further details can be found in the IEEE standard 1987 [61].

2.2.2 Nonlinear Piezoelectric Constitutive Relations

An alternative one dimensional form of the electric enthalpy density (2.7) in the linear case in shown (2.14) [62];

$$H = \frac{1}{2}c^{E}_{11}S^{2}_{11} - c^{E}_{11}d_{31}S_{11}E_3 - \frac{1}{2}\left(\varepsilon^{T}_{33} - c^{E}_{11}d^{2}_{31}\right)E_3{}^{2} \qquad (2.14)$$

This form is gotten by substituting (2.15) and (2.16) below into (2.7);

$$e_{31} = d_{31}c^{E}_{11} \qquad (2.15)$$

$$\varepsilon^{S}_{33} = \left(\varepsilon^{T}_{33} - d^{2}_{31}c^{E}_{11}\right) \qquad (2.16)$$

Therefore (2.17) and (2.18) can be derived from (2.8);

$$\sigma_{11} = c^{E}_{11}S_{11} - c^{E}_{11}d_{31}E_3 \qquad (2.17)$$

$$D_3 = c_{11}^E d_{31} S_{11} + \left(\varepsilon_{33}^T - c_{11}^E d_{31}^2\right) E_3 \tag{2.18}$$

Results from experiments conducted by Nguyen [63] show that the nonlinear dependence of the elastic constant c_{ijkl}^E and the piezoelectric charge constant d_{kij} on strain S_{kl} in one dimension is approximated by;

$$c^E = c_{11}^E + c_{111}^E S_{11} + c_{1111}^E S_{11}^2 \tag{2.19}$$

$$d = d_{31} + d_{311} S_{11} + d_{3111} S_{11}^2 \tag{2.20}$$

Substituting for c^E and d into (2.4) and assuming a linear relationship between D and E while retaining terms up to the third order, H becomes;

$$H = \frac{1}{2} c_{11}^E S_{11}^2 + \frac{1}{3} c_{111}^E S_{11}^3 + \frac{1}{4} c_{1111}^E S_{11}^4 - e_{31} S_{11} E_3 - \frac{1}{2} e_{311} S_{11}^2 E_3 - \frac{1}{3} e_{3111} S_{11}^3 E_3 - \frac{1}{2} \varepsilon_{33}^S E_3^2 \tag{2.21}$$

Therefore from (2.8) as before;

$$\sigma_{11} = c_{11}^E S_{11} - e_{31} E_3 + c_{111}^E S_{11}^2 + c_{1111}^E S_{11}^3 - e_{311} S_{11} E_3 - e_{3111} S_{11}^2 E_3 \tag{2.22}$$

$$D_3 = e_{31} S_{11} + \varepsilon_{33}^S E_3 + \frac{1}{2} e_{311} S_{11}^2 + \frac{1}{3} e_{3111} S_{11}^2 \tag{2.23}$$

$$\text{with} \quad e_{311} = c_{11}^E d_{311} + c_{111}^E d_{31} \tag{2.24}$$

$$\text{and} \quad e_{3111} = c_{11}^E d_{3111} + c_{1111}^E d_{31} + c_{111}^E d_{3111} \tag{2.25}$$

(2.22) and (2.23) are the nonlinear constitutive equations. Notice the linear form in the first two terms with additional terms to introduce nonlinearities. Stanton *et al.* [64] proposed nonlinear piezoelectric constitutive equations that are slightly

different. Their model ignored higher order coupling and electrical effects but includes elastic nonlinearities up to the fifth order.

2.3 Structural Model

2.3.1 Beam Theories

Initial efforts in literature were to obtain closed form solutions using the exact equations of elasticity. This have the major drawback that only very few problems can be solved exactly [65]. Four common engineering theories used for the dynamic analysis of transversely vibrating beams are shown in Table 2.1. The Euler-Bernoulli and Timoshenko beam theories are the most popular of these theories for analysis of cantilever beams.

The basic assumptions made by all models are as follows.

- One dimension (axial direction) is considerably larger than the other two.
- The material is linear elastic.
- The Poisson effect is neglected.
- The cross-sectional area is symmetric so that the neutral and centroidal axes coincide.
- Planes perpendicular to the neutral axis remain perpendicular after deformation.

- The angle of rotation is small so that the small angle approximation can be used.

The Euler Bernoulli model includes the strain energy due to bending and the kinetic energy due to lateral displacement which is sufficient for slender beams [66]. Timoshenko proposed a beam theory which adds the effect of shear as well as the effect of rotation to the Euler-Bernoulli beam. The Timoshenko model is a major improvement for non-slender beams and for high-frequency responses, where transverse (out-of-plane) shear deformation or rotary effects are not negligible [66]. In this theory, to simplify the derivation of the equations of motion, the shear strain is assumed to be uniform over a given cross section. In turn, a shear correction factor is introduced to account for this simplification, and its value depends on the shape of the cross section [65, 67-68]. A slender beam without high frequency responses is assumed here; therefore, the Euler Bernoulli beam model is adopted.

Table 2.1: Beam Theories

Beam Models	Bending Moment	Lateral Displacement	Shear Deformation	Rotary Inertia
Euler-Bernoulli	✓	✓	X	X
Rayleigh	✓	✓	X	✓
Shear	✓	✓	✓	X
Timoshenko	✓	✓	✓	✓

Han Benaroya *et al.*

2.3.2 Beam Kinematics

With small deformations a linear beam model would suffice as shown in Figure 2.3 [69]. Normal to the neutral axis will remain normal after bending (i.e. lines AB and A′B′) therefore the rotation of the cross-section ϑ can be tied to the rotation of the neutral axis

i.e. $$\vartheta = -\theta \tag{2.26}$$

and $$\theta = \frac{dw}{dx} \tag{2.27}$$

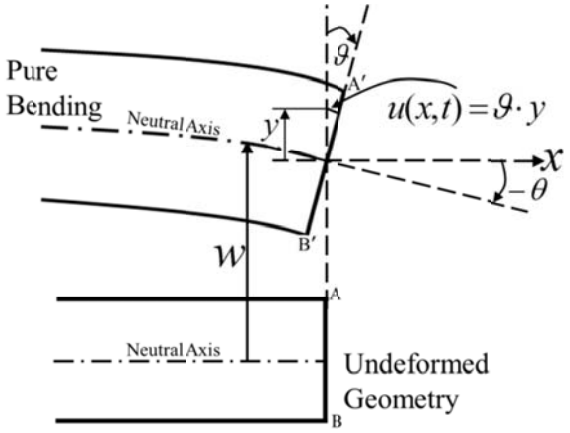

Figure 2.3: Schematic of beam under small deformation

The axial displacement becomes

$$u(x,t) = -y\theta = -y\frac{dw}{dx} \tag{2.28}$$

Under a pure bending motion, the strain in the y-direction is assumed to be negligible. Therefore the normal strain is defined as

$$\varepsilon_{xx} = \frac{du}{dx} = -y\frac{d^2w}{dx^2} = -y\theta' \tag{2.29}$$

When the deformations are moderately large, for accurate modeling, nonlinearities also need to be included. Figure 2.4 shows the beam kinematics before and after deformation [70-73]. The centerline of the beam is assumed to be initially lying along the x_0-axis and the beam oscillates in the (x_0,y) plane. The coordinate of a point along the beam refers to the undeformed body which is represented by x. A point can also be represented by s, the curvilinear coordinate along the beam. By applying beam centerline inextensible condition, i.e., $dx = ds$, one can define the zero stretching, λ, which relates axial displacement (u) with transverse displacement (w) along the beam centerline.

$$\lambda^2 = (1+u')^2 + (w')^2 = 1 \tag{2.30}$$

Note that $(\,)'$ denotes the derivative with respect to coordinate s.

The curvature is defined by

$$\kappa = \theta' = w''(1+u') - w'u'' \tag{2.31}$$

Here, $\theta(s,t)$ is the rotational angle with respect to the horizontal direction.

From (2.30), one can determine the axial displacement in terms of transverse displacement. It is approximated by

$$u' \approx -\frac{1}{2}w'^2 \tag{2.32}$$

For a cantilevered beam, the axial displacement is defined by

$$u(s,t) = -\frac{1}{2}\int_0^s w(\xi,t)^2 \, d\xi \tag{2.33}$$

(2.31) can be expanded by Taylor series, and the terms if $O(w^4)$ and higher orders are neglected as shown below.

$$\kappa = \theta' = w''\left(1 + \frac{1}{2}w'^2\right) + O(w^4) \tag{2.34}$$

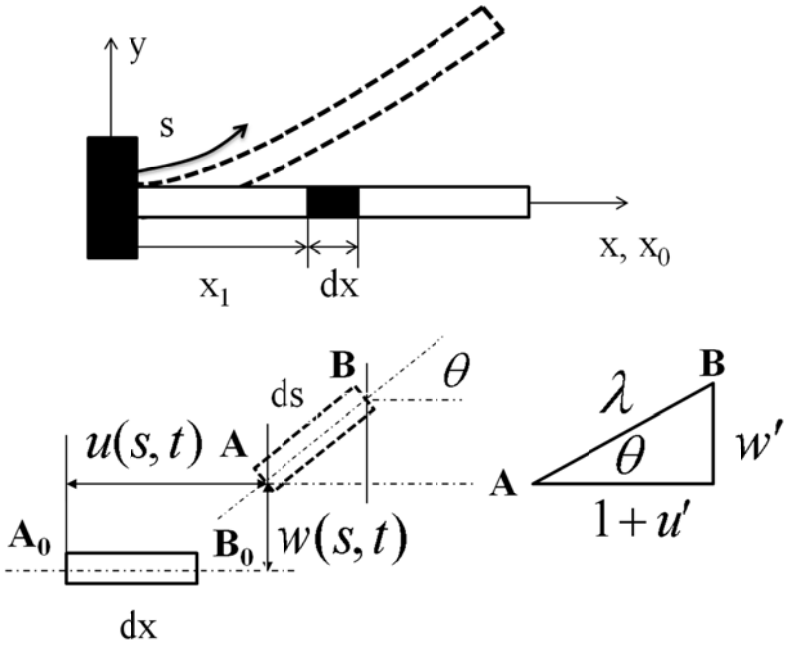

Figure 2.4: Schematic of a beam under geometrically nonlinear deformation

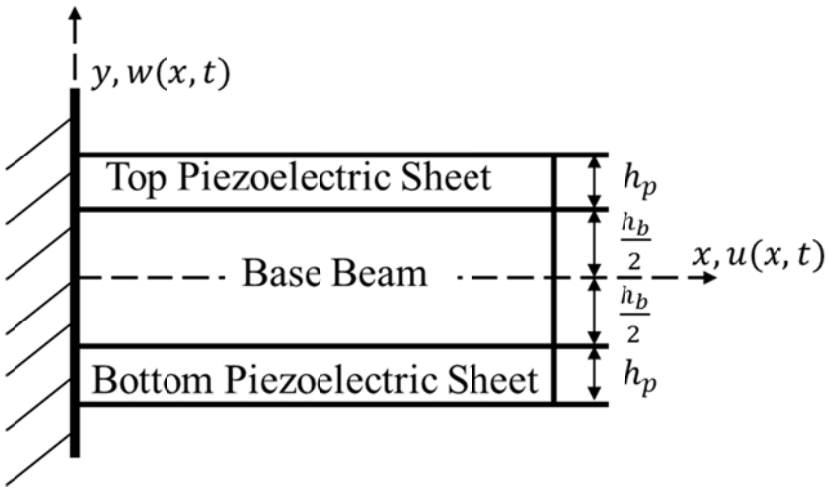

Figure 2.5: Bimorph piezoelectric beam

Finally in the bimorph case the normal strains are still determined as

$$\begin{cases} \varepsilon_{p1} = -y\theta' & \frac{h_b}{2} \le y \le \frac{h_b}{2} + h_p \\ \varepsilon_b = -y\theta' & -\frac{h_b}{2} \le y \le \frac{h_b}{2} \\ \varepsilon_{p2} = -y\theta' & -\frac{h_b}{2} - h_p \le y \le -\frac{h_b}{2} \end{cases} \tag{2.35}$$

2.4 Flow-Induced Vibration

2.4.1 Aeroelastic Instabilities

There is coupling between fluid flow and structure through the fluid force exerted on the body by the fluid, i.e., aerodynamic force. Aerodynamic forces cause the structure to deform. Subsequently, as the structure deforms, its orientation to the airflow changes and the aerodynamics forces may change. Moreover, the structure exerts an equal and opposite force on the fluid as the fluid exerts force on

the body. If the oscillating aerodynamic force tends to increase structural vibration, the structure is aerodynamically unstable and may result in very large amplitude vibration. In subsonic flow, structures shed vortices which can interact with the structure to cause vortex induced vibrations (VIV). The vortex street wakes tend to be similar regardless of the cross-sectional geometry and usually occur at a Strouhal number; S≈0.2 [7, 74-77]. The Strouhal number is defined below;

$$\frac{1}{S} = \frac{V}{f_s D} \tag{2.36}$$

Where f_s is vortex shedding frequency in hertz, V is the free stream flow velocity and D is the cylinder cross-section length perpendicular to the approaching flow. If the changing flow velocity ensures that f_s approaches the natural frequency (f_n) of an elastic circular cross-section structure. Resultant locked-in resonant oscillations can occur, leading to large amplitude vibrations at approximately;

$$\frac{V}{f_n D} \cong \frac{V}{f_s D} = \frac{1}{S} \cong 5 \tag{2.37}$$

This aeroelastic instability (VIV) has been used as the basis for fluid flow meters [78-79], but if not suppressed can lead to catastrophic failures as seen in marine cables and pipelines [80]. All structures with non-circular cross-sections can undergo galloping and flutter. While many flow-induced vibration is a result of vortex shedding, flutter results from the coupling of two structural modes which

mainly distinguishes it from galloping. Aeroelastic flutter is coupled torsion-plunge instability of airfoil structures while galloping is one degree of freedom instability of bluff structures in wind and currents [7]. Flutter of aircraft wings is evidently the most familiar example of this flow-induced vibration first experienced by Professor Samuel Langley monoplane in 1903. It remains a fundamental criterion for issuing aircrafts airworthiness certificates [7]. Some common types of flutter include; "divergence" or zero frequency flutter , control reversal, whirl flutter which affects rotor blades in engines and in rotorcrafts blades, stall flutter and buffeting – a high frequency random forced vibration caused by a sudden impulse from load increasing. Generally, aeroelastic instabilities are characterized by a critical set of flow conditions that define the stability boundary and the point when oscillations begin. Above this point the oscillations continues to grow as fluid flow transfers energy to the structure until the deflections become sufficient for system nonlinearities to create limit cycle oscillations or for uncontrollable "divergence" to occur leading to structural failure. Aeroelastic flutter is not an easily controllable phenomenon due to the inherent multiple coupled structural modes. Also, significant oscillations only occur in a small range of flow velocities and with limited oscillation amplitudes for vortex induced vibrations.

However, galloping occurs for an infinite range of flow velocities and does not have a self-limited characteristic beyond the critical flow velocity such that the amplitude of oscillation increases monotonically with flow velocity i.e. easily controllable. Therefore, with the goal being to extract wind energy for various applications, the aeroelastic instability – Transverse Galloping provides a reliable and effective solution. Note that a good selection of mechanical and geometrical properties is essential to gain optimal performance.

2.4.2 Bluff Body Shapes

A body is said to be bluff if its cross-section is such that the length in the flow direction is equal or close to its length in the perpendicular direction and as such flow separates from a large section of the body's surface [81]. The size and shape of a two dimensional bluff body subject to galloping oscillations are the most important parameters because the pressure loading that causes oscillations are principally on the after body surface [82-83]. Therefore a D-section bluff body will remain stable if the flat edge is downstream and gallop when the flat face is upstream and normal to the incident flow. In both cases the flow will separate at the edges but there's no after-body in the former to induce galloping. Different bluff body shapes have been explored in literature including D shape [36, 84-85], Isosceles triangle [82,86], Equilateral triangle [35], Rectangle [7,39,84,87], and

Square [39,82,87-90]. Novak and Tanaka conducted experiments on D-section, 2/3 rectangular and 3/2 rectangular shapes [84]. It was shown that the bluff bodies will gallop at lower velocities in turbulent flows compared to smooth flows. Increasing the mean angle of attack causes the stability of galloping prismatic bodies to transition from stable to unstable as demonstrated in the experiments conducted by Luo *et al.* [82].

Research efforts on galloping of square-section bluff bodies have had extended focus in literature mainly because of its symmetry, hysteresis behavior and performance [39,87,89-91]. Classical nonlinear analysis of the square prism in the phase plane as well as determination of the hysteresis region was presented by Parkinson and Smith [89]. Novak determined coefficients for the vertical aerodynamic force acting on the square bluff body for different modes of beam vibration and boundary conditions [90]. CFD analysis conducted by Luo *et al.* showed that the presence of intermitted shear layer attachment accounts for the hysteresis region [91] while Barrero *et al.* demonstrated analytically the role of inflection points in the hysteresis phenomenon [92].

2.5 Bluff Body Aerodynamic Model

2.5.1 Quasi-static Aerodynamics

When the characteristic timescale of flow is small compared to the characteristic timescale of oscillation as observed in transverse galloping, the quasi-steady hypothesis first established by Den Hartog is a good approximation [85,93]. Typically, to account for the aerodynamic forces introduced by the tip bluff body, an empirical vertical force coefficient is used to represent the resultant aerodynamic forces, which are determined by wind tunnel testing data [7]. The quasi-steady aerodynamic model assumes that the aerodynamic forces on the structure are solely dependent on the instantaneous relative velocity and angle of attack. This requirement is often met at higher reduced flow velocities such that;

$$U = \frac{V}{f_n D} > 20 \tag{2.38}$$

2.5.2 Bluff Body Aerodynamics

The baseline bluff body has a constant square cross-section in the axial direction; it implies determination of the aerodynamic force can be considered as two dimensional. As shown in Figure 2.6, the resultant vertical (transverse) aerodynamic force, F_y is defined by

$$F_y = -(C_D \sin\Psi + C_L \cos\Psi)\frac{1}{2}\rho h l V^2 \sec^2\Psi \quad = \frac{1}{2} C_{FY} \rho h l V^2 \tag{2.39}$$

$$C_{FY} = -(C_L + C_D \tan\Psi)\sec\Psi \tag{2.40}$$

Where C_D and C_L are the coefficient of drag and lift respectively.

Here V is incident wind velocity, ρ is air density, h is the side length of the section, and l is the length of bluff body. C_{FY} is the vertical aerodynamic force coefficient used to fit wind tunnel data (Figure 2.7), and is usually given by empirical formulas. It is approximated by a polynomial in $\tan\Psi = \frac{\dot{y}}{V}$ over the pertinent range of Ψ $(-16^{\circ} \le \Psi \le 16^{\circ})$ as:

$$C_{FY} = \sum_{i=0}^{\infty} A_i \left(\frac{\dot{y}}{V}\right)^i \tag{2.41}$$

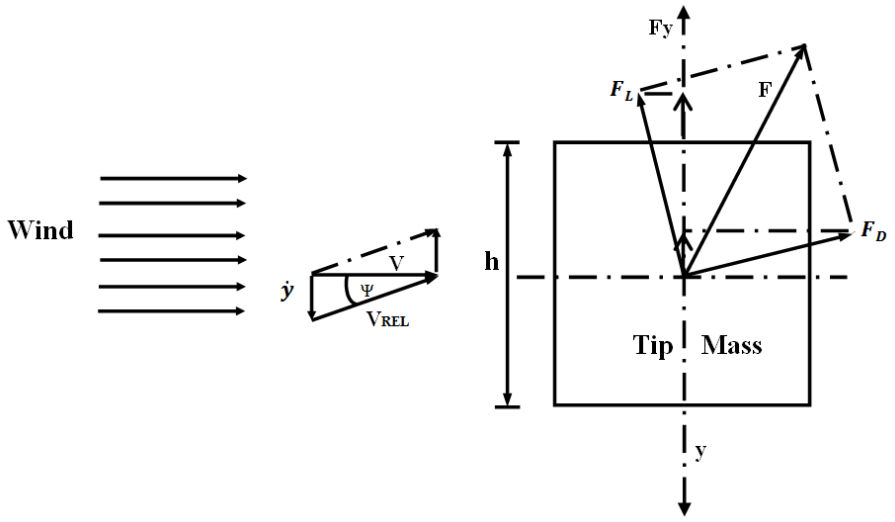

Figure 2.6:Schematic representation of aerodynamic force on tip mass

If the cross-section is symmetrical about a line through the center of the flow, only odd harmonics $A_1, A_3, A_5 \ldots$will be non-zero as will be shown in the case of the square section.

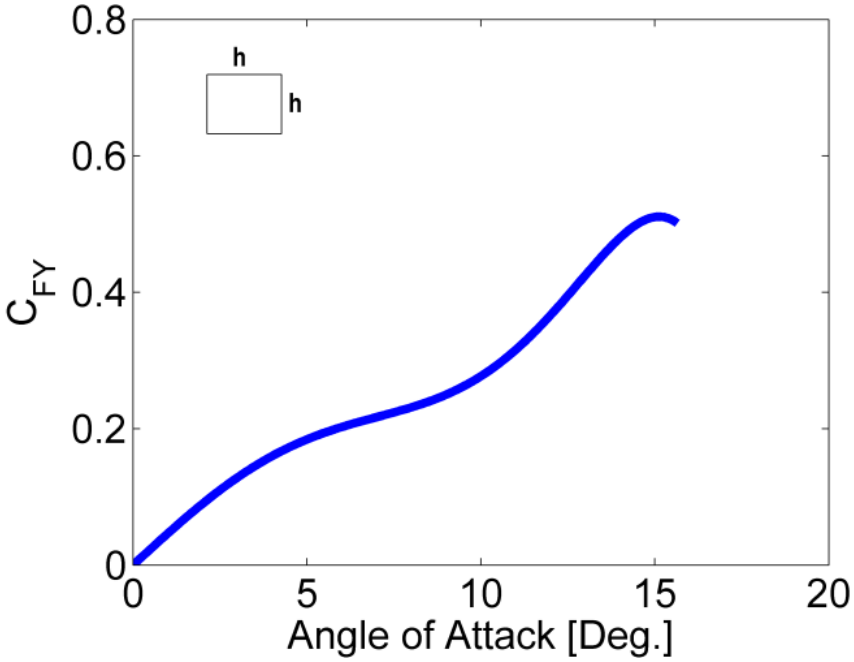

(a)

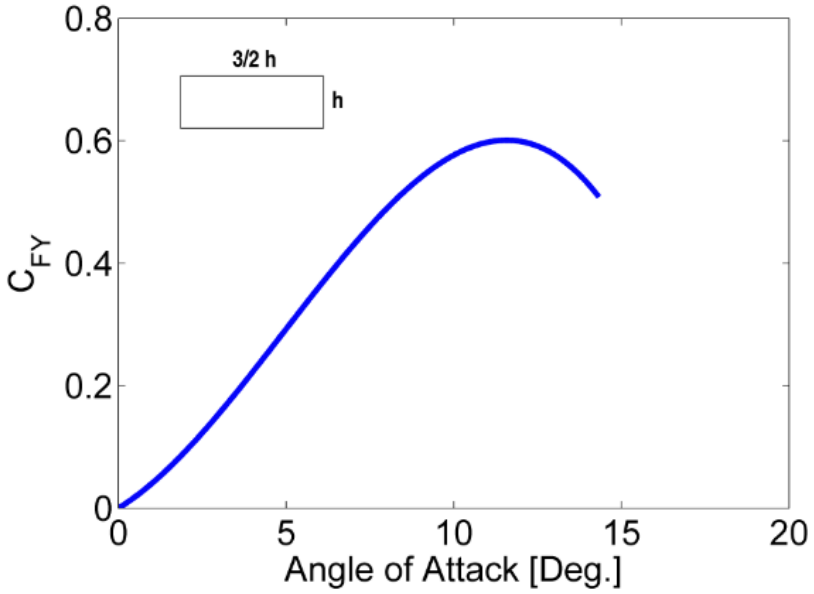

(b)

Figure 2.7: Aerodynamic vertical force coefficients under smooth flow for bluff body on a Cantilever: (a) Square (b) Rectangle

If the bluff body has a non-constant geometry in the lateral direction, 3D analysis will be required as seen in the case of a square bluff body with a wavy leading edge. Novak considered such problems for wind speed variation in the

lateral direction using an average lateral deflection coefficient (C_{FY}) [90]. Sullivan extended Novak's formulation to incorporate the variation of C_{FY} with the height of the bluff body; and validated the application of quasi-static aerodynamics to 3D analysis [94]. His formulation can be applied to incorporate the varying geometry in the lateral direction (z). Therefore, the aerodynamic force on the bluff body becomes;

$$F_y(z,\Psi) = C_{FY}(z,\Psi)\frac{\rho}{2}hV^2(z) \tag{2.42}$$

Where,

$$C_{FY}(z,\Psi) = \sum_{i=0}^{\infty} A_i(z)\left(\frac{\dot{y}(z)}{V(z)}\right)^i$$

(2.43) is used to express the dependence of A_i on the lateral dimension (z).

$$A_i(z) = \sum_{j=0}^{\infty} A_{i,j}\left(\frac{z}{h}\right)^i \tag{2.43}$$

Chapter 3: Coupled Aero-Electro-Mechanical Model Development

In order to characterize the performance of the GPEHs, two coupled aero-electro-mechanical models were developed. The first model assumes linear piezoelectricity and small deformation. Similar to the VBEH case, both piezoelectric beam kinetic energy and potential energy are determined. Subsequently, the bluff body aerodynamic force is introduced. The Krylov-Bogoliubov method is used to determine analytical approximate solutions of the coupled nonlinear aero-electro-mechanical equations. Both transient and steady state response are characterized. A nonlinear model was developed as well in order to capture large beam deflection and high electrical response in piezoelectric materials, in which both geometrically nonlinear structural deformation and nonlinear piezoelectricity are included. The same Krylov-Bogoliubov solution approach was applied to determine associated structural and electrical responses. Finally, model prediction results were presented. Results from this Chapter have resulted in a journal publication on the Journal of Intelligent Material System and Structures.

3.1 GPEH Model with Linear Motion and Linear Piezoelectricity

3.1.1 Energy and Virtual Work

The GPEH is composed of a cantilever beam, surfaced bonded piezoelectric layers, and a tip bluff body. The tip bluff body is used to induce the vibration when it is subjected to airflow. Figure 3.1 shows a cantilevered piezoelectric beam with a tip bluff body. For simplification, two identical piezoelectric layers are assumed but different poling directions are allowed in order to demonstrate both series and parallel arrangements of these two piezoelectric layers. Other key assumptions are:

- Linear piezoelectric constitutive relationship [6,61].
- Same transverse displacement across entire beam thickness
- Perfect bonding between piezoelectric layer and base beam, i.e., no slip
- Shear deformation and rotary inertia neglected, i.e., Euler-Bernoulli beam theory.

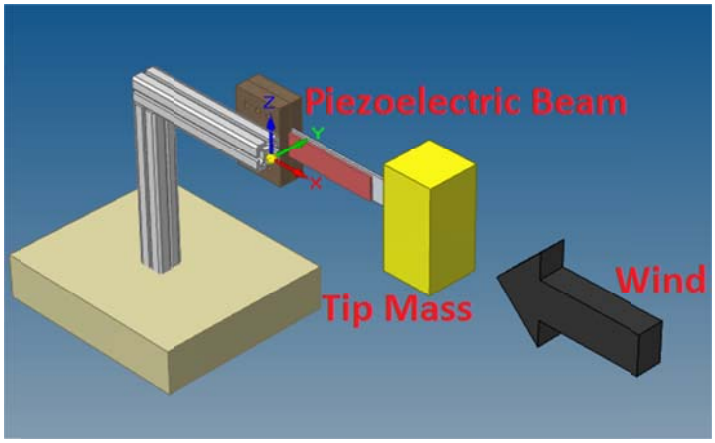

(a)

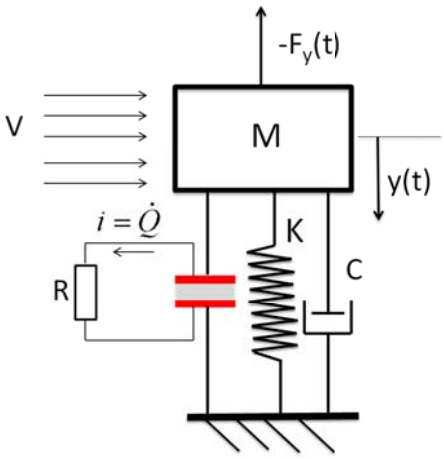

(b)

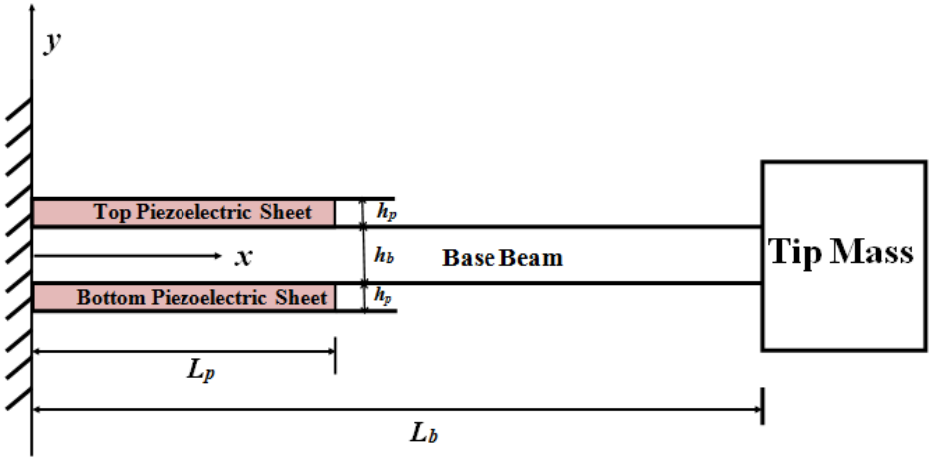

(c)

Figure 3.1: Model: (a) Galloping Piezoelectric Energy Harvester (GPEH) (b) Single Degree of freedom (SDOF) (c) GPEH schematic

The h-form is adopted

$$\begin{bmatrix} \sigma_{11} \\ E_3 \end{bmatrix} = \begin{bmatrix} C_{11}^D & -h_{31} \\ -h_{31} & \beta_{33}^D \end{bmatrix} \begin{bmatrix} S_{11} \\ D_3 \end{bmatrix} \tag{3.1}$$

Finally, the potential energy is given by:

$$U(\varepsilon, D) = \frac{1}{2}\int_{V_b}\left(\sigma_b \varepsilon_b\right) dV_b + \frac{1}{2}\int_{V_p}\left(\sigma_{p_1}\varepsilon_{p_1} + E_3 D_3\right) dV_p + \frac{1}{2}\int_{V_p}\left(\sigma_{p_2}\varepsilon_{p_2} + \bar{E}_3\bar{D}_3\right) dV_p \tag{3.2}$$

The subscript p and b denote piezoelectric layer and beam, respectively. The h-form adopted ensures both normal strain ε, and electrical displacement D, in the top and bottom piezoelectric layers are employed as independent variables as discussed by Ikeda [49], Sirohi and Mahadik [35] and Wang [22].

The kinetic energy of the bimorph piezoelectric beam is:

$$T = \frac{1}{2}\int_{Vb} \rho_b \dot{w}^2 dV_b + \frac{1}{2}\int_{V_p} 2\rho_p \dot{w}^2 dV_p + \frac{1}{2} M_{tip} \dot{w}^2(L,t) \tag{3.3}$$

The virtual work done by the tip vertical resultant force due to bluff body aerodynamics and electrical field is:

$$\delta W_{ext} = F_y \delta w(l,t) + \int_0^{L_p} h_p v_1 \delta D_3 dx + \int_0^{L_p} h_p v_2 \delta \bar{D}_3 dx \tag{3.4}$$

F_y is the resultant transverse aerodynamic force acting on the bluff body. v_1 and v_2 are the voltage drop across the non-conservative electrical element from the top and the bottom piezoelectric layers, respectively.

3.1.2 Governing Equations

The transverse displacement is assured as a product of the beam bending mode shape functions $\phi_i(x)$ and associate coefficients $y_i(t)$ [35];

$$w(x,t) = \sum_{j=1}^{N} \phi_j(x) y_j(t) = \phi_1 y_1 = \phi y \tag{3.5}$$

Where, N is the number of modes.

The potential energy can be rewritten by assuming only one beam mode

$$U = \frac{1}{2}Ky^2 + \frac{1}{2C_p}Q^2 + y\Theta Q \tag{3.6}$$

Where K is the stiffness matrix and Θ is the piezoelectric coupling matrix and C_p is capacitance.

Similarly, the kinetic energy is

$$T = \frac{1}{2}M\dot{y}^2 \tag{3.7}$$

Applying Lagrange equation, two coupled equations of motion for a GPEH are given by

$$\ddot{y} + 2\xi\omega\dot{y} + \omega^2 y + \lambda_1\Theta Q = \overline{F}_{tip} \tag{3.8}$$

$$R\dot{Q} + \frac{\lambda_2}{C_P}Q + \lambda_1\Theta y = 0 \tag{3.9}$$

Θ is the piezoelectric coupling term. Q is the total charge in piezoelectric layers, C_p is the total capacitance, and R is the electrical load. ω is the natural frequency. ξ is the viscous damping ratio (Note that the modal damping is introduced here). All parameters are defined below.

Where

$$M = \int_{V_b} \rho_b \phi^2 dV_b + \int_{V_p} \rho_p \phi^2 dV_p + \phi^2(L_b)M_{tip} \tag{3.10}$$

$$K = \int_{V_p} \frac{\varepsilon_{33}^{\ T}}{S_{11}^{E}\varepsilon_{33}^{T} - d_{31}^{2}} y^2 \left(\frac{d^2\phi}{dx^2}\right)^2 dV_p + \int_{V_b} E_b y^2 \left(\frac{d^2\phi}{dx^2}\right)^2 dV_b \tag{3.11}$$

$$\Theta = \lambda_i \int_{V_p} \frac{y\phi'' k_{31}}{d_{31}(1-k_{31}^2)A_p} dV_p \tag{3.12}$$

$$k_{31} = \frac{h_{31}^2}{C_{11}^D \beta_{33}^D} \tag{3.13}$$

$$C_p = \frac{\varepsilon_{33}^S L_p b_p}{h_p} \tag{3.14}$$

$$\omega^2 = \frac{K}{M} \tag{3.15}$$

$$\overline{F}_{tip} = \frac{F_y}{M} = \frac{\rho V^2 hl}{2M} C_{FY} \tag{3.16}$$

Series	Parallel
$\lambda_1 = 2 \quad , \quad \lambda_2 = 2$	$\lambda_1 = 1 \quad , \quad \lambda_2 = \frac{1}{2}$

(3.17)

λ_1 and λ_2 are constants for both series and parallel connections between two piezoelectric layers. Dimensionless formulation is used so that it is very convenient to conduct scaling and performance comparison of different galloping piezoelectric devices. Dimensionless is conducted on the final coupled (3.8) and (3.9) to yield two coupled equations so that the system parameters can be varied independently. The two equations are

$$Y'' + 2\xi Y' + Y + \lambda_1 \overline{Q} = \frac{\eta}{2} U^2 C_{FY} \tag{3.18}$$

$$\alpha \overline{Q}' + \lambda_2 \overline{Q} + \lambda_1 \beta Y = 0 \tag{3.19}$$

Associated non-dimensional parameters are defined as:

$$Y = \frac{y}{h} \quad \tau = \omega t \quad (\,)' = \frac{d(\,)}{d\tau} \quad U = \frac{V}{\omega h}$$
$$\overline{Q} = \frac{\Theta}{Kh} Q \quad \alpha = \omega R C_p \quad \beta = \frac{\Theta^2 C_p}{K} \quad \eta = \frac{\rho A_b l}{M}$$

A_b is the bluff body cross sectional area.

3.1.3 Solution Approach

Based on the Krylov-Bogoliubov method [95], the first approximation solutions for the dimensionless LCO amplitude is

$$\begin{aligned} Y &= Y_0(\tau)\sin(\omega t + \phi(\tau)) = Y_0(\tau)\sin(\psi(\tau)), \\ Y' &= Y_0\omega\cos(\omega t + \phi(\tau)) \approx Y_0\cos(\psi(\tau)) \end{aligned} \tag{3.20}$$

If we assume the charge output depends on the LCO amplitude as given below

$$\begin{aligned} \overline{Q} &= Q_0\sin(\omega t + \phi_1) = Q_0\sin(\psi + \phi_1), \\ \overline{Q}' &= Q_0\cos(\psi + \phi_1) \end{aligned} \tag{3.21}$$

Here ϕ, ϕ_1 represents phase angles.

Differentiating (3.21) and substituting for $\overline{Q}'$, $\overline{Q}$ and Y into (3.19), after some rearrangement yields

$$\overline{Q} = Q_0\sin(\psi - \gamma) = -\frac{\beta}{a} Y_0\sin(\psi - \gamma) \tag{3.22}$$

Where the amplitude, a, and phase angle, γ, are given by

$$a = \sqrt{\alpha^2 + {\lambda_2}^2} \qquad \gamma = \tan^{-1}\frac{\alpha}{\lambda_2} \tag{3.23}$$

Differentiating (3.20) and substituting for Y'', Y' and $\overline{Q}$ into (3.18) also, noting that Y_0 and ϕ varies slowly with τ , it is sufficient to average the behavior of the system over one cycle. Finally, the dimensionless LCO amplitude can be determined by

$$\frac{dY_0}{d\tau} = \frac{1}{2\pi}\int_0^{2\pi}\left[\eta U^2 C_{FY} - 2\xi Y_0 \cos\psi - \bar{Q}\right]\cos\psi d\psi = 0 \tag{3.24}$$

The dimensionless LCO frequency also satisfy a similar equation in the first approximation

$$\frac{d\psi}{d\tau} = \Omega = 1 + \frac{1}{2\pi Y_0}\int_0^{2\pi} -\left[\eta U^2 C_{FY} - 2\xi Y_0 \cos\psi - \bar{Q}\right]\sin\psi d\psi \tag{3.25}$$

The aerodynamic force coefficient in terms of $\frac{Y'}{U}$ is express as,

$$C_{FY} = A_0 + A_1\frac{Y'}{U} + A_2\left(\frac{Y'}{U}\right)^2 + A_3\left(\frac{Y'}{U}\right)^3 + A_4\left(\frac{Y'}{U}\right)^4 + A_5\left(\frac{Y'}{U}\right)^5 + A_6\left(\frac{Y'}{U}\right)^6 + A_7\left(\frac{Y'}{U}\right)^7 + \cdots \tag{3.26}$$

In this case, A_0 is equal to zero. A 7th order polynomial function is sufficient to represent the vertical force coefficients for both rectangular and square sections. Substituting (3.26) into (3.24), a polynomial function is obtained in terms of the LCO amplitude, which is given by

$$\frac{dY_G}{d\tau} = C_3 {Y_G}^7 + C_2 {Y_G}^5 + C_1 {Y_G}^3 + C_0 Y_G = 0 \tag{3.27}$$

Where $c_0 = \frac{A_1\eta U}{4} - \xi - \frac{\beta\sin\gamma}{2a}$ $c_1 = \frac{3\eta A_3}{16U}$ $c_2 = \frac{5\eta A_5}{32U^3}$ $c_3 = \frac{35\eta A_7}{256U^5}$

If $A_1 > 0$ the galloping criterion is reached [85,90,93], therefore the galloping wind velocity is;

$$U \; > \; U_g = \frac{4\xi + 2\beta \sin\gamma / a}{A_1 \eta} \tag{3.28}$$

Note that all even terms in the vertical force coefficients vanish after the integration. Substituting for $\overline{Q}$ from (3.22) into (3.25) and integrating, the galloping frequency is determined as,

$$\Omega = 1 - \frac{\beta \cos\gamma}{2a} \tag{3.29}$$

The LCO amplitude can be determined by substituting corresponding coefficients for different bluff body sections.

3.1.4 Bluff body with rectangular cross section

For a bluff body with a rectangular cross section (aspect ratio=1.5), the vertical aerodynamic force coefficient is given by [7]

$$\begin{aligned} C_{FY} &= A_1 \frac{Y'}{U} + A_2 \left(\frac{Y'}{U}\right)^2 + A_3 \left(\frac{Y'}{U}\right)^3 + A_4 \left(\frac{Y'}{U}\right)^4 \\ &= A_1 \left(\frac{Y_0 \cos\psi}{U}\right) + A_2 \left(\frac{Y_0 \cos\psi}{U}\right)^2 + A_3 \left(\frac{Y_0 \cos\psi}{U}\right)^3 + A_4 \left(\frac{Y_0 \cos\psi}{U}\right)^4 \end{aligned} \tag{3.30}$$

Using Novak coefficients for a bluff body on a cantilever [90], the rectangular section coefficients is

$A_1 = 1.9142 \quad A_2 = 24.8493 \quad A_3 = -94.9833 \quad A_4 = -10.0336$

The LCO amplitude can be determined by solving the following linear algebra equation since even coefficients vanish after integration.

$$c_1 Y_0^{\,2} + c_0 = 0 \tag{3.31}$$

The solution of Y_0 is

$$Y_0 = \sqrt{-\frac{c_0}{c_1}} \tag{3.32}$$

Note that $c_1 < 0$ and $c_0 > 0$ if $U > U_g$.

No inflection point is observed on the C_{FY} curve for the rectangular section which results in only one stationary oscillation with amplitude as shown in (3.32), therefore no hysteresis is noticed.

3.1.5 Bluff body with square cross section

For a bluff body with a square cross section, the vertical aerodynamic force coefficient is given by [7,89]

$$\begin{aligned} C_{FY} &= A_1 \frac{Y'}{U} + A_3 \left(\frac{Y'}{U}\right)^3 + A_5 \left(\frac{Y'}{U}\right)^5 + A_7 \left(\frac{Y'}{U}\right)^7 \\ &= A_1 \left(\frac{Y_0 \cos\psi}{U}\right) + A_3 \left(\frac{Y_0 \cos\psi}{U}\right)^3 + A_5 \left(\frac{Y_0 \cos\psi}{U}\right)^5 + A_7 \left(\frac{Y_0 \cos\psi}{U}\right)^7 \end{aligned} \tag{3.33}$$

The coefficients as given by Novak [90] for a square section on a cantilever is

$$A_1 = 2.69 \quad A_3 = -93.33 \quad A_5 = 2411.54 \quad A_7 = -17617.65$$

Substituting these vertical force coefficients into (3.26), the LCO amplitude equation takes the form

$$c_3 Y_0^{\,6} + c_2 Y_0^{\,4} + c_1 Y_0^{\,2} + c_0 = 0 \tag{3.34}$$

When $U > U_g$, self-excited vibration will initiate. The real and positive roots of (3.34) result in the LCO amplitudes, which are dependent on the incident wind velocity. The charge developed in the piezoelectric materials can then be determined using (3.22) by substituting the solution of LCO amplitude under each wind velocity. As discussed by Novak [90], two identical real roots can appear which result in the hysteresis LCO response. Parkinson and Smith [89] establish this on the basis of phase plane analysis. The physics behind the hysteresis response is due to the role of inflection points in the vertical aerodynamic force coefficient curve as discussed by Barrero-Gil *et al.* [92]. The C_{FY} curve for a square section show two inflection points and results in a jump between stationary oscillations in the hysteresis range. The wind velocities associated with the hysteresis range are given by

$$U_{1,2} = \frac{U_g}{1 + \frac{35}{64A_1} Z_1 \mp \frac{35A_7}{64A_1} Z_2} \tag{3.36}$$

Where

$$Z_1 = \frac{1024A_5^{\,3}}{9261A_7^{\,2}} - \frac{128A_3A_5}{245A_7}$$

$$Z_2 = \sqrt{-\frac{4}{27}\left(-\frac{64A_5^{\,2}}{147A_7^{\,2}} + \frac{48A_3}{35A_7}\right)^3}$$

3.1.6 Transient Analysis

The self-excited nature of the galloping phenomenon requires initial perturbations to grow when axial wind flow across the tip bluff body until steady state amplitude is reached which is determined by the initial velocity [85]. The predicted transient period can be determined by integrating (3.24), with some rearrangement gives;

$$N\tau = \int_{W_0}^{W} \frac{dW}{W^4 + c_2^* W^3 + c_1^* W^2 + c_0^* W} = \int_{W_0}^{W} \frac{dW}{W(W - W_1)(W - W_2)(W - W_3)} \tag{3.37}$$

Where $N = \dfrac{512U}{35\eta A_7}, \quad W = \left(\dfrac{Y_0}{U}\right)^2, \quad W_0 = \left(\dfrac{Y_{01}}{U}\right)^2, \quad W_i = \left(\dfrac{Y_{0i}}{U}\right)^2, \quad i = 1, 2, 3$

$$c_0^* = \left(\frac{A_1\eta}{4} - \frac{\xi}{U} + \frac{\beta \sin\gamma}{2aU}\right)\frac{256}{35\eta A_7}, \quad c_1^* = \frac{768A_3}{560A_7}, \quad c_2^* = \frac{1280A_5}{1120A_7}$$

W_1, W_2, and W_3 are three roots of the cubic equation, respectively. Y_{01} is the initial displacement amplitude. For regions outside the hysteresis range one of the roots of the cubic equation is real and the other two are complex conjugates

$$W_{1,2} = m \pm in \tag{3.38}$$

The integral takes the form

$$N\tau = \ln\left[\left(\frac{W}{W_0}\right)^{\frac{-1}{W_3(m^2+n^2)}}\left(\frac{W - W_3}{W_0 - W_3}\right)^{\frac{1}{W_3\left[(W_3-m)^2+n^2\right]}}\left(\frac{(W-m)^2 + n^2}{(W_0 - m)^2 + n^2}\right)^{\frac{W_3 - 2m}{2(m^2+n^2)\left[(m-W_3)^2+n^2\right]}}\right] + \\ + \frac{\left(m^2 - W_3 m - n^2\right)}{n\left(m^2+n^2\right)\left[(m-W_3)^2+n^2\right]}\left[\tan^{-1}\left(\frac{W-m}{n}\right) - \tan^{-1}\left(\frac{W_0 - m}{n}\right)\right] \tag{3.39}$$

Within the hysteresis range the roots of the equation are all real with the possibility of a double root. The integral will be in the form:

$$-N\tau = \ln\left[\left(\frac{W}{W_0}\right)^{\frac{-1}{W_1W_2W_3}}\left(\frac{W-W_1}{W_0-W_1}\right)^{W_{1,23}}\left(\frac{W-W_2}{W_0-W_2}\right)^{W_{2,13}}\left(\frac{W-W_3}{W_0-W_3}\right)^{W_{3,12}}\right] \tag{3.40}$$

Where $$W_{i,jk} = \frac{1}{W_i(W_i-W_j)(W_i-W_k)} \tag{3.41}$$

3.2 GPEH Model with Geometrically Nonlinear Motion and Nonlinear Piezoelectricity

3.2.1 Energy and Virtual Work

Moderately large deflections can occur which requires a model to capture nonlinearities inherent in the system. The main assumptions in the linear model apply with key assumptions for the nonlinear case stated below;

- The three-layered beam is inextensible and initially straight
- Euler-Bernoulli beam theory with geometrically nonlinear motion
- Linear elasticity for base beam material
- Nonlinear piezoelectric constitutive relationship

The internal energy is given as;

$$U = U_b + U_{p_1} + U_{p_2} = \frac{1}{2}\int_{Vb}(\sigma_b \times \varepsilon_b)dv + \frac{1}{2}\int_{Vp_1} Hdv + \frac{1}{2}\int_{Vp_2} Hdv \tag{3.42}$$

The piezoelectric sheets are assumed to be identical therefore the volume of piezoelectric layers $V_p = V_{p_1} = V_{p_2}$. Curvature κ from (2.34) is used to obtain the normal strain (2.35). We insert enthalpy H from (2.21) and the normal strains into (3.42). After integration, we obtain the following expression for the internal energy.

$$U = \frac{1}{2}\int_0^L E_b I_b \kappa^2 ds + \int_0^L \left(C_{11}^E I_{p_1} \kappa^2 + e_{31} b \bar{h} \kappa v + e_{311} I_{p_2} \kappa^3 v + C_{1111}^E I_{p_3} \kappa^4 \right) ds - \frac{1}{2} C_p v^2 \qquad (3.43)$$

Where

$$I_b = \frac{1}{12} b h_b^3 \quad \bar{h} = \frac{h_b + h_p}{2}$$

$$I_{p_1} = \int_{\frac{h_b}{2}}^{\frac{h_b}{2}+h_p} b y^2 dy = \frac{1}{4} b {h_b}^2 h_p + \frac{1}{2} b h_b {h_p}^2 + \frac{b {h_p}^3}{3}$$

$$I_{p_2} = \int_{\frac{h_b}{2}}^{\frac{h_b}{2}+h_p} \frac{2}{3h_p} b y^3 dy = \frac{b\left(-{h_b}^4 + \left(h_b + 2h_p\right)^4\right)}{96 h_p}$$

$$I_{p_3} = \int_{\frac{h_b}{2}}^{\frac{h_b}{2}+h_p} b y^4 dy = \frac{b\left(-{h_b}^4 + \left(h_b + 2h_p\right)^4\right)}{160}$$

$$C_p = \frac{\varepsilon_{33}^s b L}{2 h_p}$$

Note that the terms associated with e_{311} and C_{111}^E vanish after integration due to the symmetry of the bimorph configuration.

The kinetic energy is

$$T = \frac{1}{2}\int_0^L \left(m\dot{w}^2 + m\dot{u}^2 \right) dx \qquad (3.44)$$

Where; $m = \rho_b b h_b + 2\rho_p b h_p$ is the mass per unit length of the bimorph. Note that $\dot{()}$ denotes the derivative with respect to time.

The virtual work done by external force, electrical field, and non-conservative force is

$$\delta W_{ext} = \int_0^L F_y \delta(s-L)\delta w ds - \int_0^L C_d \dot{w}\delta w ds - Q\delta v \tag{3.45}$$

Where; F_y is the resultant aerodynamic force acting on the tip bluff body, C_d is the viscous damping force coefficient; Q is the charge developed in both piezoelectric layers.

3.2.2 Governing Equations

After applying Hamilton's principle, one can obtain governing equations in terms of transverse displacement w and voltage v with associated boundary conditions.

$$\begin{aligned} &m\ddot{w} + C_d\dot{w} + EI\left[w'''' + \left(w'(w'w'')'\right)'\right] + m\left[w'\int_L^s d\xi\int_0^s\left[\dot{w}'^2 + w'\ddot{w}'\right]d\zeta\right]' \\ &+ 12C_{1111}^E I_{p_3} w''\left[2w'''^2 + w''w''''\right] + 6e_{3111}I_{p_2} v\left[w'''^2 + w''w''''\right] \\ &+ e_{31}\bar{bh}v\left[\delta'(s) - \delta'(s-L)\right] = \bar{F}_{tip} \end{aligned} \tag{3.46}$$

$$C_p\frac{dv}{dt} + \frac{v}{R} - 3\int_0^L e_{3111}I_{p_2} w''^2\dot{w}'' ds - \int_0^L e_{31}\bar{bh}\dot{w}'' ds = 0 \tag{3.47}$$

Here $\dot{Q} = -\frac{v}{R}$. The coupling term associated with e_{31} is included in (3.43), in which the Dirac delta function $\delta(s)$ is used. R is the electrical load.

Where

$$EI = E_b I_b + 2C_{11}^E I_{p_1}$$

Associated boundary conditions at $s = 0, L$

$$w=0 \quad \text{or} \quad EI(w''' + w''' w'^2 + w''^2 w') + 4C_{1111}^D I_{p_3} \left(w''^3\right)' + 3e_{3111} I_{p_2} v \left(w''^2\right)' = 0 \tag{3.48}$$

$$w'=0 \quad \text{or} \quad -EI(w'' + w'' w'^2) - 4C_{1111}^D I_{p_3} w''^3 - 3e_{3111} I_{p_2} v w''^2 = 0 \tag{3.49}$$

It is a challenge to solve the coupled nonlinear partial differential equations (3.46 - 3.47). In order to obtain the near-resonant solutions, the Galerkin method is applied. The transverse displacement, $w(s,t)$ can be expressed as a summation of N generalized coordinates, $y_j(t)$, and assumed beam mode shape functions, $\phi_j(s)$.

$$w(s,t) = \sum_{j=1}^{N} \phi_j(s) y_j(t) \tag{3.50}$$

Typically, exact cantilevered beam mode shape functions are selected to yield a set of ordinary differential equations (ODEs) in terms of unknown generalized coordinates and harvested voltage [64] [96]. Analytical approximation solutions are expected so that physical insights can be collected to design and understand the piezoelectric energy harvesters with nonlinearities. Therefore, one single beam mode is used and it is given by

$$\phi_1(s) = \phi(s) = \frac{2s^2}{L^2} - \frac{4s^3}{3L^3} + \frac{s^4}{3L^4} \tag{3.51}$$

Note the above beam mode shape satisfies both geometric and force boundary conditions as shown in (3.48 - 3.49). Substituting (3.51) and conducting integration, one can obtain the discretized equation.

$$\ddot{y} + 2\mu\dot{y} + \omega_0^2 y + by^3 + dy^3 + c\left(\dot{y}^2 + y\ddot{y}\right) + \left(e + fy^2\right)v = \overline{F}_{tip} \tag{3.52}$$

$$C_p\dot{v} + \frac{v}{R} - \left(\theta_1 + \theta_2 y^2\right)\dot{y} = 0 \tag{3.53}$$

where

$$\omega_0^2 = \frac{K}{M} \quad b = \frac{K_1}{M} \quad c = \frac{M_1}{M} \quad d = \frac{K_2}{M} \quad e = \frac{\theta_1}{M} \quad f = \frac{K_3}{M} \quad \mu = \frac{C_d}{2m}$$

$$M = \int_0^L m\phi^2 ds = m\frac{104L}{405}$$

$$K = \int_0^L EI\phi\phi'''' ds = \frac{16}{5L^3}$$

$$M_1 = \int_0^L m\left[\phi'\left(\int_L^s d\varsigma \int_0^s \phi'^2 d\xi\right)'\right] ds = m\frac{352}{1215L}$$

$$K_1 = \int_0^L EI\phi\left(\phi''''\phi'^2 + 4\phi'\phi''\phi''' + \phi''^2\right) ds = EI\frac{128}{55L^5}$$

$$K_2 = 4C_{1111}I_{p3}\int_0^L \phi\left(6\phi''\phi'''^2 + 3\phi''^2\phi''''\right) ds = 4C_{1111}I_{p3}\frac{256}{9L^7}$$

$$K_3 = 6e_{3111}I_{p2}\int_0^L \phi\left(\phi'''^2 + \phi''\phi''''\right) ds = 6e_{3111}I_{p2}\frac{32}{7L^5}$$

$$\theta_1 = e_{31}b\overline{h}\,\phi'(L)$$

$$\theta_2 = 3e_{3111}I_{p2}\int_0^L \phi''^3 ds = 3e_{3111}I_{p2}\frac{64}{7L^5}$$

Note that for this mode shape $K_3 = \theta_2$. As shown in Table 3.1, by specifying different values of coefficients in (3.52 - 3.53), one can obtain corresponding equations with different assumptions.

Table 3.1 : Model Coefficients under different assumptions

Model	Coefficients
Linear Case	$b=c=d=f=\theta_2=0$
Geometrically Nonlinear Case Only	$d=f=\theta_2=0 \quad b\neq 0 \quad c\neq 0$
Piezoelectric Material Nonlinear Case Only	$b=c=0 \quad d\neq 0 \quad f\neq 0 \quad \theta_2\neq 0$

Under the geometrically nonlinear motion assumption, a cubic spring term (coefficient b) and a coupling term due to kinematics (coefficient c) are introduced. By assuming nonlinear piezoelectric constitutive, not only a cubic spring term (coefficient d), but also higher order electromechanical coupling term (coefficients f and θ_2) are introduced. Corresponding solutions under different assumptions can be obtained by simply substituting different values.

3.2.3 Solution Approach

The solution to the nonlinear case is presented using the Krylov-Bogoliubov first approximation method as in the linear case. The coupled equations (3.52 - 3.53) for the nonlinear case can be expressed as;

$$[1+cY]Y'' + 2\xi Y' + chY'^2 + \frac{1}{\omega^2}\left[\omega_0^2 + (b+d)h^2Y^2\right]Y + \frac{\lambda_1}{\omega^2 h}\left[\left(e + fh^2Y^2\right)\right]v = \frac{\eta}{2}U^2 C_{FY} \quad (3.54)$$

$$v' + \frac{\lambda_2 v}{\alpha} - \frac{\left(\theta_1 h + \theta_2 h^3 Y^2\right)}{C_p}Y' = 0 \quad (3.55)$$

The first approximation solutions for the LCO amplitude is

$$\begin{aligned} Y &= Y_0(\tau)\sin(\omega t + \phi_2(\tau)) = Y_0(\tau)\sin(\psi(\tau)), \\ Y' &= Y_0\omega\cos(\omega t + \phi_2(\tau)) \approx Y_0\cos(\psi(\tau)) \end{aligned} \quad (3.56)$$

We assume the voltage output depends on the LCO amplitude as given below

$$\begin{aligned} v &= v_0\sin(\omega t + \phi_3) = v_0\sin(\psi(\tau) + \phi_3), \\ v' &= v_0\cos(\psi(\tau) + \phi_3) \approx v_0\cos\left(\psi_1(\tau)\right) \end{aligned} \quad (3.57)$$

Here ϕ_2, ϕ_3 represents phase angles.

Substituting for (3.56) and (3.57) into (3.55) after some rearrangement yields

$$v_0 = \frac{\theta_1 h Y_0 + \theta_2 h^3 Y_0^{\,3}}{C_p a/\alpha} \quad (3.58)$$

The LCO amplitude as before (3.24) can be determined from

$$\frac{dY_0}{d\tau} = \frac{1}{2\pi}\int_0^{2\pi} \left[\begin{array}{l} \frac{\eta}{2} U^2 C_{FY} - 2\xi Y_0 \cos\psi \ldots \\ \ldots + \omega^2 \left(1 + cY_0 \sin\psi\right) Y_0 \sin\psi - \omega^2 chY_0^2 \cos^2\psi \ldots \\ \ldots - \frac{\omega_0^2}{\omega^2} Y_0 \sin\psi - \frac{\left(b+d\right)}{\omega^2} Y_0^3 \sin^3\psi \ldots \\ \ldots - \frac{e\theta_1}{\omega^2 C_p a/\alpha} Y_0 \sin\psi_1 - \frac{e\theta_2 h^2}{\omega^2 C_p a/\alpha} Y_0{}^3 \sin\psi_1 \ldots \\ \cdots - \frac{f\theta_1 h^2}{\omega^2 C_p a/\alpha} Y_0{}^3 \sin^2\psi \sin\psi_1 - \frac{f\theta_2 h^4}{\omega^2 C_p a/\alpha} Y_0{}^5 \sin^2\psi \sin\psi_1 \end{array} \right] \cos\psi d\psi = 0 \tag{3.59}$$

Substituting for C_{FY} (3.26) into (3.59), a polynomial function is obtained in terms of the dimensionless LCO amplitude, which is given by

$$c_3 Y_0^{\,7} + c_2 Y_0^{\,5} + c_1 Y_0^{\,3} + c_0 Y_0 = 0 \tag{3.60}$$

Where

$$c_0 = \frac{A_1 \eta U}{4} - \xi - \frac{\beta_1 \sin\gamma}{2a}$$

$$c_1 = \frac{3\eta A_3}{16U} - 5\frac{\sqrt{\beta_1 \beta_2}\sin\gamma}{8a}$$

$$c_2 = \frac{5\eta A_5}{32U^3} - \frac{\beta_2 \sin\gamma}{8a}$$

$$c_3 = \frac{35\eta A_7}{256U^5}$$

Also,

$$\beta_1 = \frac{\alpha\theta_1^2}{K_{nl} C_p}, \quad \beta_2 = \frac{\alpha\theta_2^2 h^4}{K_{nl} C_p} \tag{3.61}$$

The amplitude, a, and phase angle, γ, are given by;

$$a = \sqrt{\alpha^2 + \lambda_2^{\,2}} \qquad \gamma = \tan^{-1}\frac{\lambda_2}{\alpha} \tag{3.62}$$

Here ω_0, ω are the linear and nonlinear undamped natural frequencies respectively.

$$\omega^2 = \frac{K_{nl}}{M} = \frac{K + (K_1 + K_2)h^2 Y_0^2}{M} \tag{3.63}$$

Since ω_0 and ω are very close, using the linear model parameters as initial conditions, ω can be determined by solving (3.60) and (3.63) iteratively at the critical velocity U_g. A matlab code has been developed to implement the algorithm in order to determine both ω and Y_0.

Nonlinearity introduces additional damping terms to coefficients C_1 and C_2 decreasing the structural response as compared to the linear model. The decrease in structural response is compensated for with the additional nonlinear term in the voltage equation (3.58). Therefore, the electrical response remains the same for the reduced LCO amplitude. The velocity for initiation of galloping (U_g) and the hysteresis range ($U_{1,2}$) remain the same as in the linear case.

The dimensionless LCO frequency also satisfies a similar equation in the first approximation as before (3.25);

$$\frac{d\psi}{d\tau} = \Omega = 1 + \ldots$$

$$\ldots + \frac{1}{2\pi\omega(1+cY_0)Y_0}\int_0^{2\pi}\left[\begin{array}{l} \\ \\ \dfrac{\eta}{2}U^2 C_{FY} - 2\xi Y_0 \cos\psi \ldots \\ \ldots + \omega^2(1+cY_0\sin\psi)Y_0\sin\psi \ldots \\ \ldots - \omega^2 chY_0^2\cos^2\psi \ldots \\ \ldots - \dfrac{\omega_0^2}{\omega^2}Y_0\sin\psi - \dfrac{(b+d)}{\omega^2}Y_0^3\sin^3\psi \ldots \\ \ldots - \dfrac{e\theta_1}{\omega^2 C_p a/\alpha}Y_0\sin\psi_1 - \dfrac{e\theta_2 h^2}{\omega^2 C_p a/\alpha}Y_0{}^3\sin\psi_1 \ldots \\ \ldots - \dfrac{f\theta_1 h^2}{\omega^2 C_p a/\alpha}Y_0{}^3\sin^2\psi\sin\psi_1 \ldots \\ \ldots - \dfrac{f\theta_2 h^4}{\omega^2 C_p a/\alpha}Y_0{}^5\sin^2\psi\sin\psi_1 \end{array}\right]\sin\psi d\psi = 0 \tag{3.64}$$

Substituting for C_{FY} and integrating, the galloping frequency is expressed as

$$\Omega = 1 + \frac{1}{(1+cY_0)}\left[\begin{array}{l} \dfrac{\omega^2-\omega_0^2}{8\omega^2}\ldots \\ \ldots - \left[\dfrac{\beta_1}{2a} - \left[\dfrac{\sqrt{\beta_1\beta_2}}{2a} + \dfrac{\sqrt{\beta_1\beta_2}h^4}{8a}\right]Y_0^2 - \dfrac{\beta_2 h^4}{8a}Y_0^4\right]\cos\gamma \end{array}\right] \tag{3.65}$$

The coupling (softening effects) between galloping frequency and LCO amplitude is evident in (3.65). Ω will vary (though slightly) as LCO amplitude changes due to changes in system damping as required by system conservation.

3.3 Model Prediction Results

3.3.1 Square section tip mass on beam without piezoelectric material

In this section, performance prediction for a representative GPEH shown in Table 3.2 is presented. Figure 3.2 shows the LCO amplitude and wind velocity characteristics for a square prism elastically mounted at both ends without piezoelectric materials [89]. Clearly, the unstable limit cycles exist in the hysteresis range. The LCO amplitude will follow the path from 1 to 5. A significant jump from 2 to 3 is observed. The present prediction matches well with experimental data.

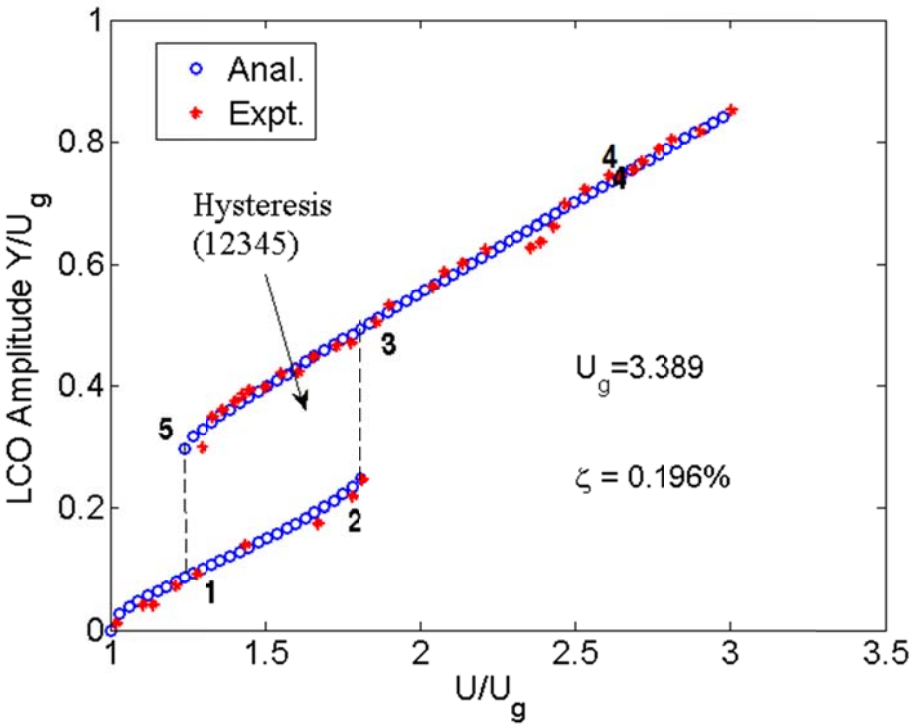

Figure 3.2: LCO amplitude and wind velocity diagram of a square prism ($\eta = 8.6 \times 10^{-4}$)

Table 3.2 : GPEH Model Properties

Bimorph piezoelectric cantilever beam constants		
Property	Piezoelectric	Base beam
Material	PZT-5A	Aluminum
Density (kg/ m^3)	7800	2700
Length (mm)	72	150
Thickness (mm)	0.267	0.889
Width (mm)	36	36
Elastic modulus $\left(1/S_{11}^{E}, E\right)$(GPa)	66	70
Piezoelectric constant (d_{31}) (pm/V)	-190	—
Piezoelectric permittivity (ε_{33}^{S}) (nF/m)	30.1	—
Tip mass properties and dimension		
Property	Square	Rectangular
Mass (kg)	0.024	0.024
Length (l)(mm)	100	100
Cross section (mm^2)	50 x 50	50 x 33.3

3.3.2 GPEH with Rectangular Tip Bluff Body

The GPEH system properties and dimensionless parameters calculated using Table 3.2 is given in Table 3.3 below. The properties of the piezoelectric material are for PSI-5A4E piezo-ceramic sheets from Piezo Systems, Inc.

Table 3.3: GPEH System Properties and Dimensionless Parameters

System Property	Parallel Connection	
Piezoelectric coupling term (Θ) (v/m)	-245.03	
Capacitance (nF)	538	
Damping Ratio (ξ) (10^{-3})	1.96	
Dimensionless Parameters		
α	R=100Ω	R=1MΩ
	0.443×10^{-3}	4.43
β	0.0234	
η	Square	Rectangle
	5.82×10^{-3}	3.88×10^{-3}

The LCO amplitude and harvested current are calculated for a GPEH with the rectangular section. Voltage is calculated using $v = IR$ and Power is calculated using $P = I^2 R$. The higher the α value, the higher the resistance load is if both piezoelectric capacitance and natural frequency are fixed. LCO amplitude and harvested energy results can be predicted as shown for various loads in Figure 3.3. The plots show the short circuit currents and the open circuit voltages are highest which is expected, while the values for power are illusionary since no power is derivable in this case. The most power is derivable at the optimum load which is around the 100kΩ. The Hysteresis behavior does not exist for the rectangular section because no inflection point is observed from the vertical aerodynamic force coefficient plot [92].

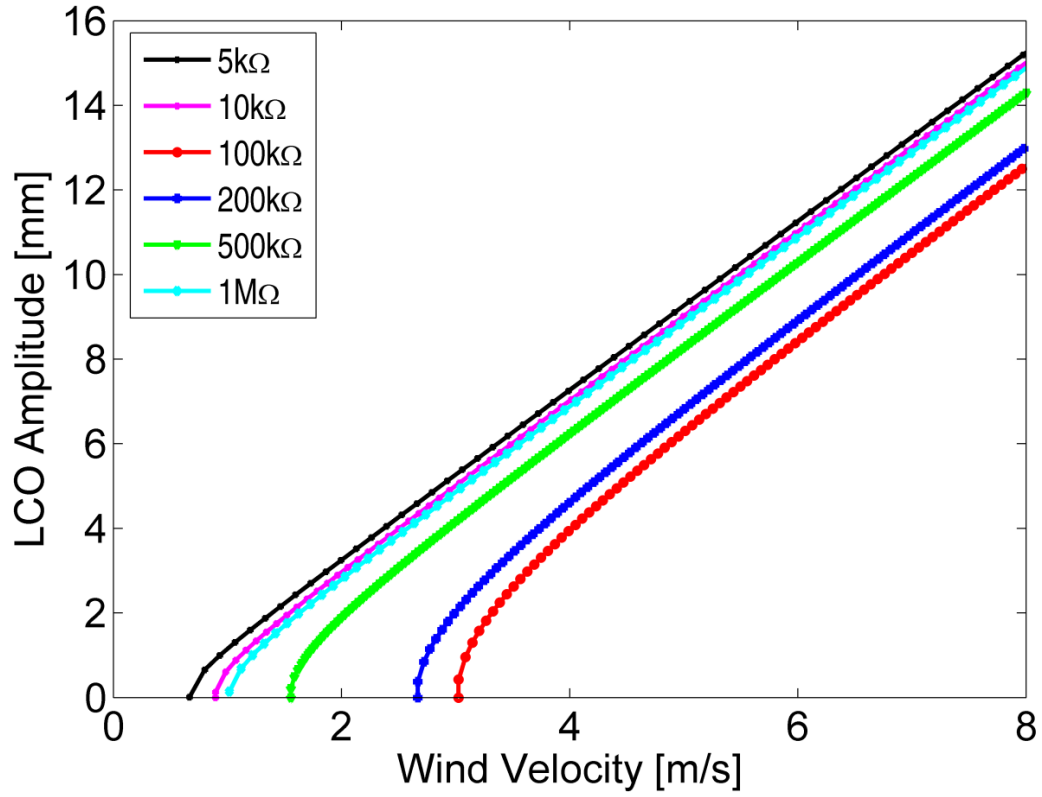
5kΩ
10kΩ
100kΩ
200kΩ
500kΩ
1MΩ
LCO Amplitude [mm]
Wind Velocity [m/s]
0
2
4
6
8
10
12
14
16

(a)

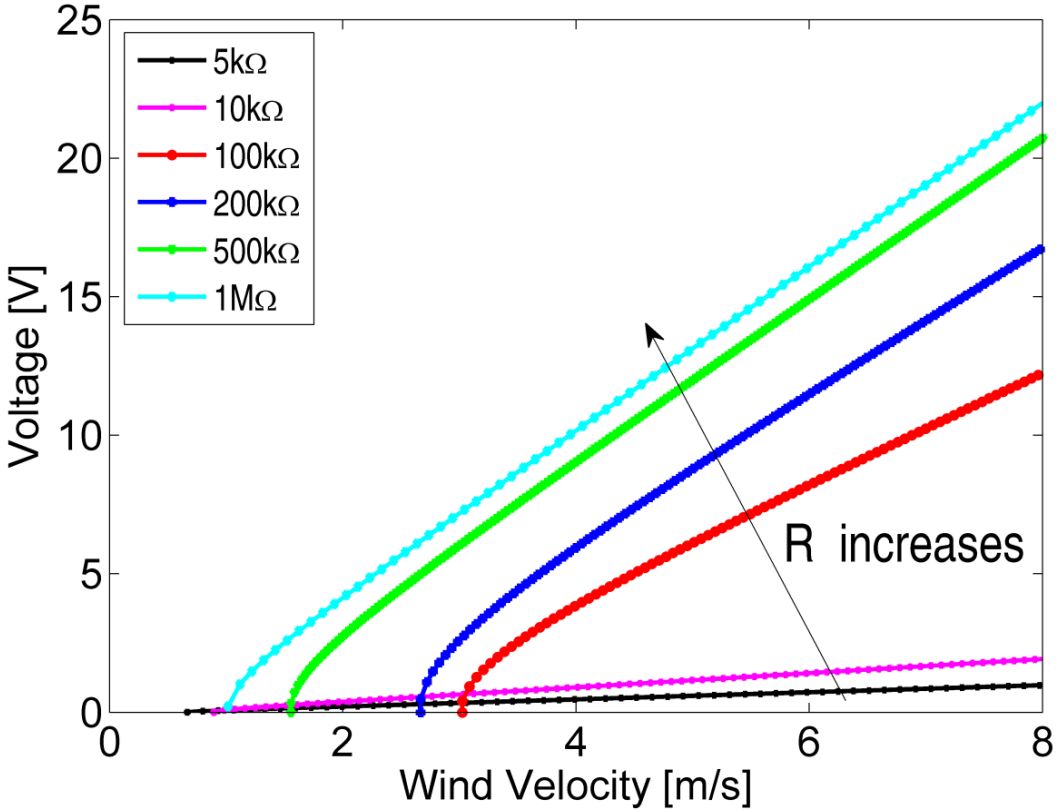
5kΩ
10kΩ
100kΩ
200kΩ
500kΩ
1MΩ
R increases
Voltage [V]
Wind Velocity [m/s]
0
5
10
15
20
25
2
4
6
8

(b)

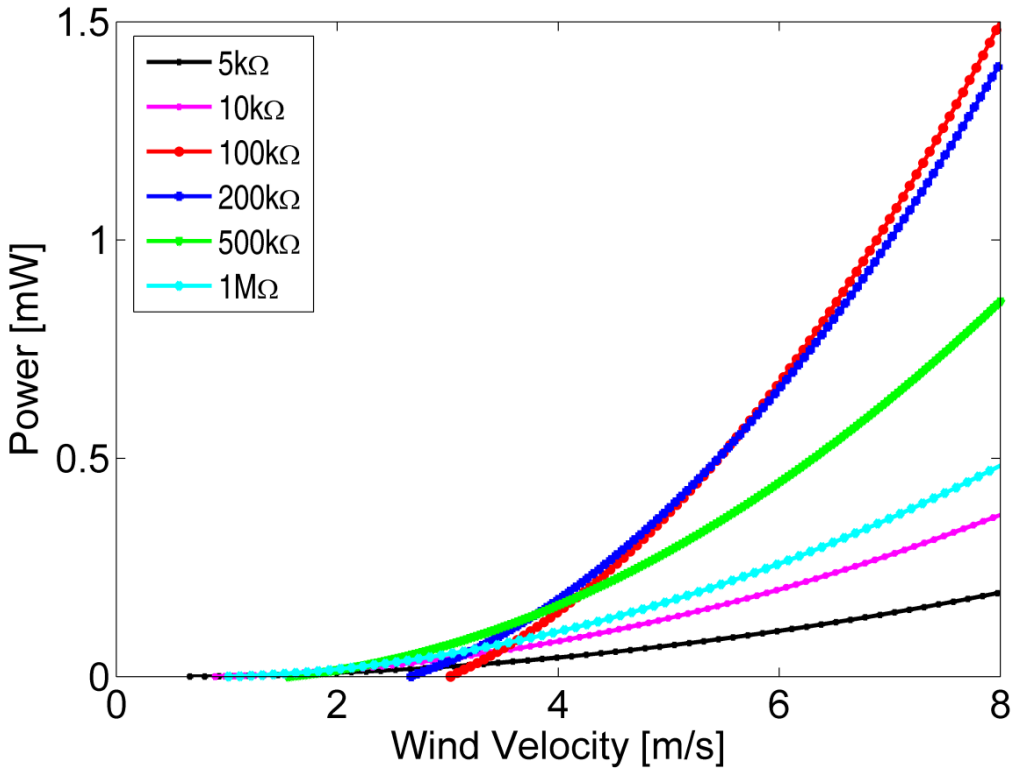

(c)

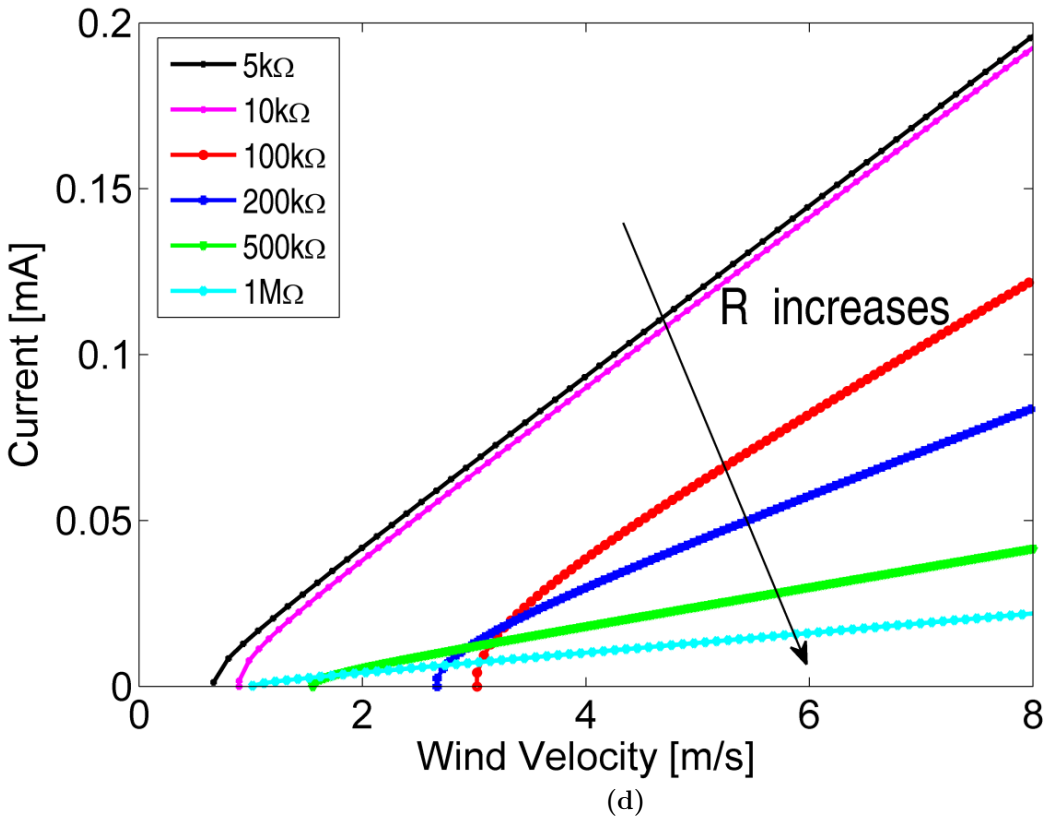

(d)

Figure 3.3: Performance prediction for rectangular section: (a) Voltage, (b) LCO amplitude (c) Power, (d) Current

3.3.3 GPEH with Square Tip Bluff Body

Applying the same parameters as used in the previous section to a GPEH with square section, similar LCO amplitude and harvested energy results can be predicted as shown in Figure 3.4 for varying loads from short circuit and open circuit. Similar hysteresis behavior is observed compared to the square prism case without piezoelectric materials in Figure 3.2. The hysteresis range is observed to occur at slightly lower values than that of the case without piezoelectric materials. The jump phenomenon can be leveraged by properly setting the corresponding wind velocity as the galloping harvester operational condition. Then a potential 100% increase of the harvested current can be achieved. Compared to the rectangular section case, the wind velocity for initiation of galloping is lower while the LCO amplitude and harvested energy are substantially higher. This implies that a GPEH with the square section is more efficient and the performance of galloping piezoelectric energy harvesters is significantly improved. Finally, in all cases, a slightly reduction of galloping frequency is obtained. The galloping frequency is computed from (3.29) to be $0.99\,\omega$. Without the piezoelectric coupling, the galloping frequency is same as the natural frequency of the single degree of freedom model as discussed by Novak [90].

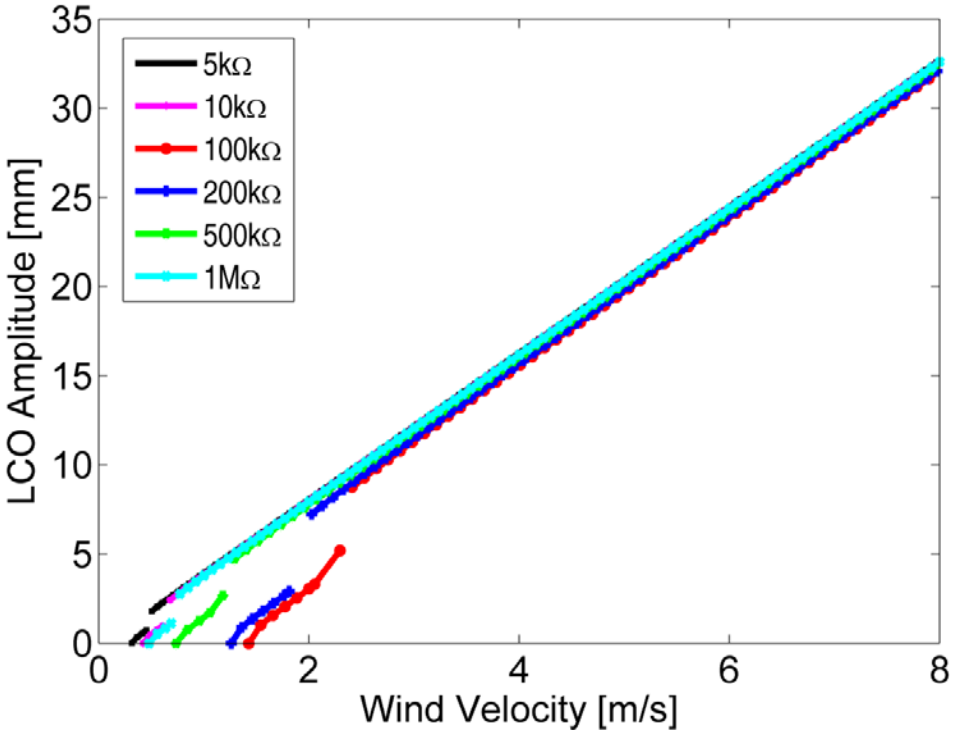
LCO Amplitude [mm]
Wind Velocity [m/s]
5kΩ
10kΩ
100kΩ
200kΩ
500kΩ
1MΩ
0
5
10
15
20
25
30
35
0
2
4
6
8

(a)

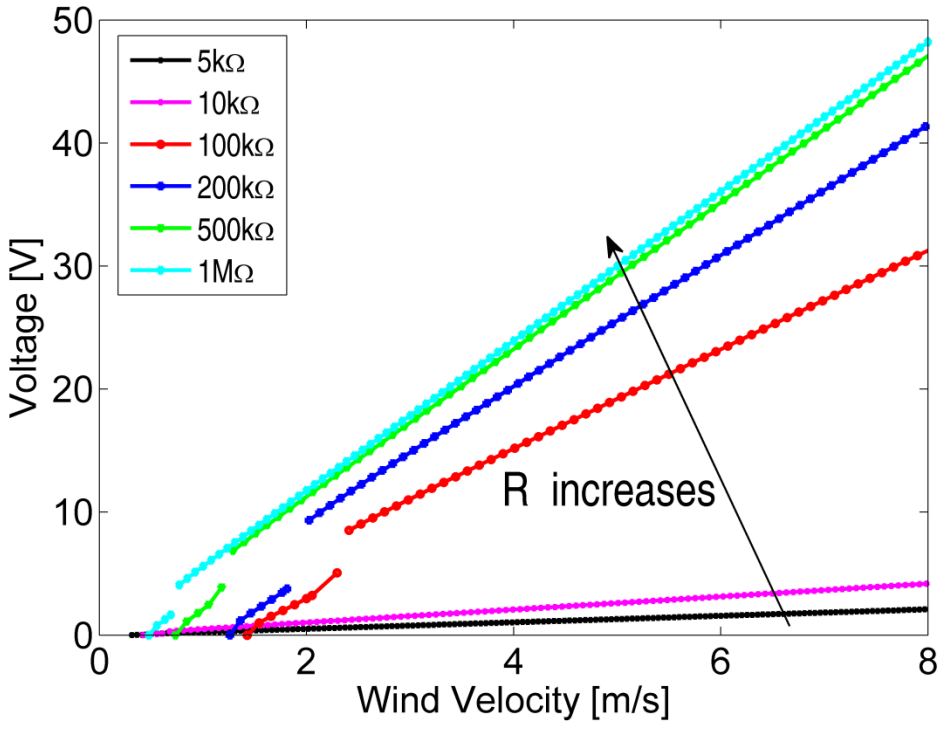
Voltage [V]
Wind Velocity [m/s]
5kΩ
10kΩ
100kΩ
200kΩ
500kΩ
1MΩ
R increases
0
10
20
30
40
50
0
2
4
6
8

(b)

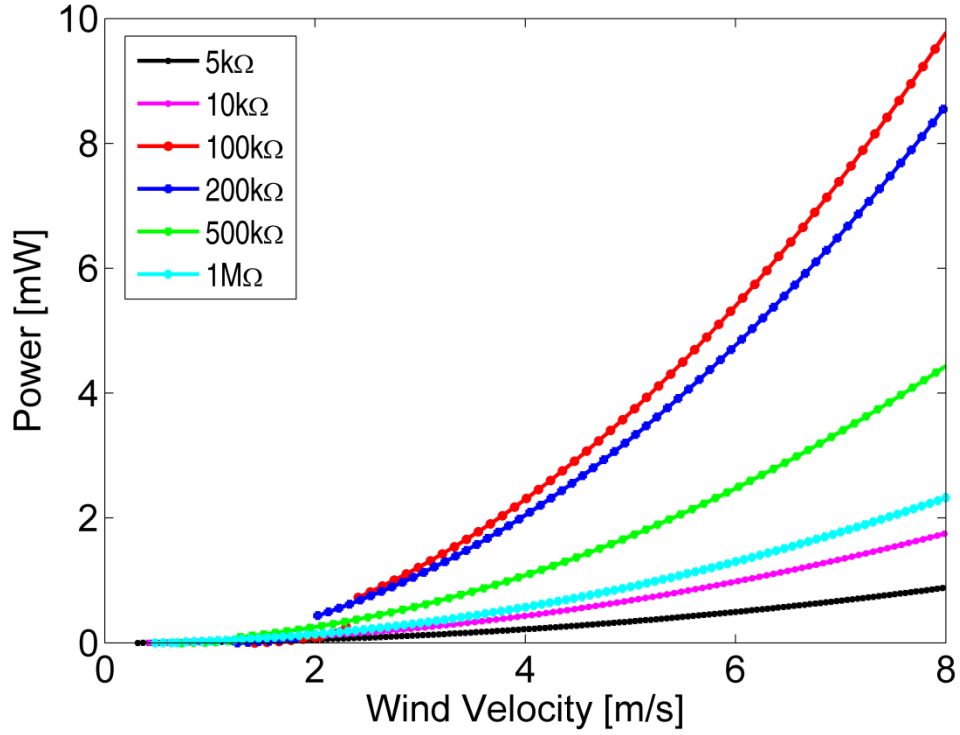

(c)

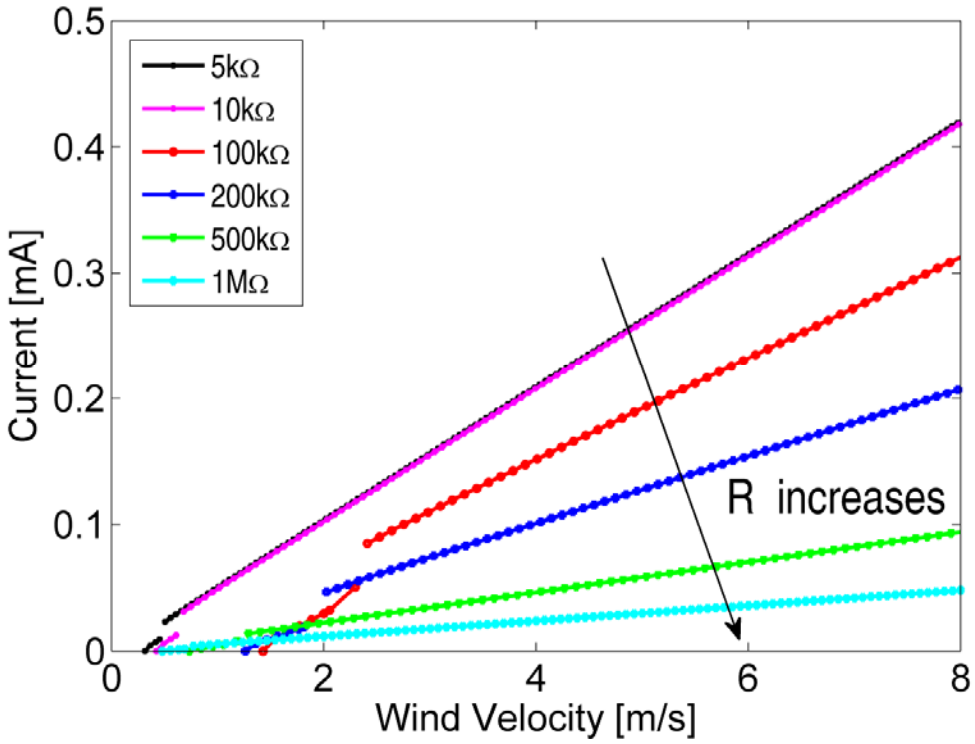

(d)

Figure 3.4: Performance prediction for square section: (a) LCO amplitude (b) Voltage (c) Power (d) Current

3.3.4 Galloping initiation velocity:

The velocity for the onset of galloping is influenced by the electrical load on the system represented by the load resistance connected across the electrodes of the piezoelectric sheets. The additional positive damping terms as seen in (3.28) cause variation in the galloping velocity as shown in Figure 3.5. The plot shows a steady increase from the short circuit load, peaks around 100kΩ (matching load and maximum power) and decreases to the open circuit loads. The troughs are the galloping velocities without piezoelectric layers. The pattern is the same for both sections with the rectangular section showing significantly higher values.

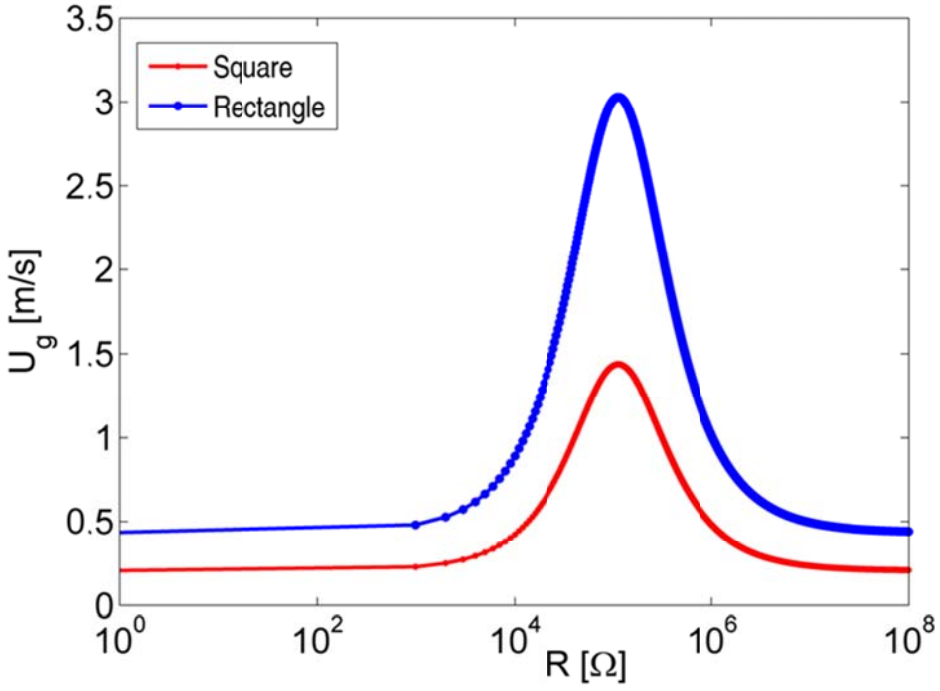

Figure 3.5: Variation of galloping velocity with electrical resistance

3.3.5 Transient response

Steady state response is desired. It is beneficial to understand the transient response in order to determine the transient period before acquiring signals.

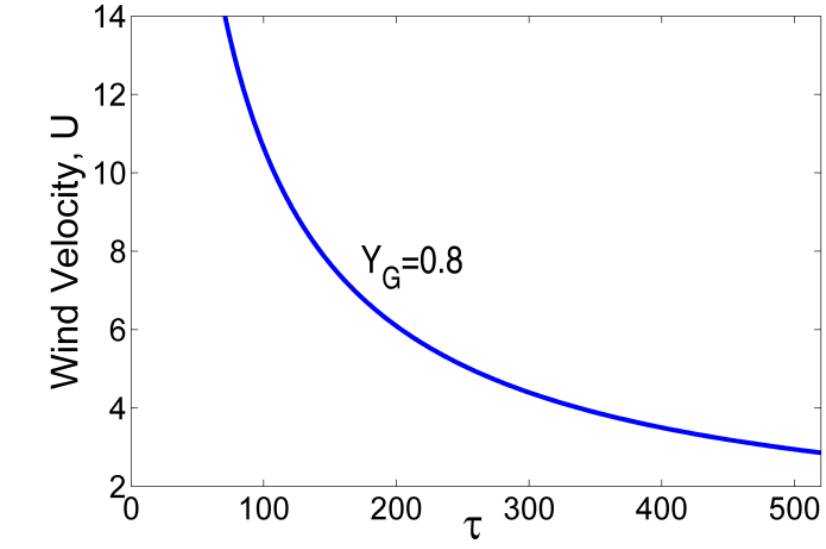

(a)

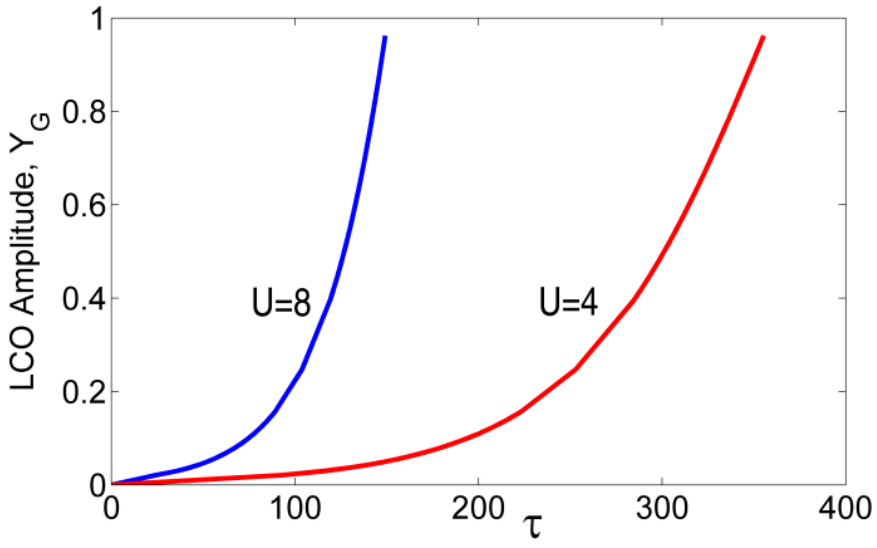

(b)

Figure 3.6: Analytical prediction of approximate time to steady oscillation, Y_0=0.002

The transient period depends on initial wind speed as shown in Figure 3.6, τ increases with decreasing initial wind speed and gradually approaches an asymptote (Figure 3.6a). The oscillation amplitude increases slowly at first and grows rapidly to steady values (Figure 3.6b). A smaller prototype with the same non-dimensional parameters will have a higher ω_n and $t=\tau/\omega_n$ reduces significantly.

3.4 Summary

Predictions from analytical approximate solutions to the coupled nonlinear aero-electro-mechanical model developed for the GPEH were presented. A representative GPEH was used for analysis, and the performance in terms of the galloping wind velocity, LCO amplitude, harvested voltage, harvested current, and harvested power was predicted for a GPEH with rectangular and square sections. Performance predictions for the different tip mass sections were demonstrated for loads varying from short circuit to open circuit. Furthermore, predictions for the transient period are given. Key conclusions are summarized below.

- Hysteresis LCO response is observed in the GPEH with square section. This is due to the unique feature of the vertical aerodynamic force of square

section bluff body. The LCO amplitude could increase substantially by leveraging the jump phenomenon.

- For the GPEH with rectangular section, there is no hysteresis response as observed in the square section case.
- The dimensionless hysteresis range velocity was also calculated for the square section and is noticed to occur at slightly lower values than the case without piezoelectric materials.
- It is observed that the velocity for initiation of galloping for the square section is significantly lower than that of the rectangular section.
- The velocity for initiation of galloping is influenced by additional positive damping from electric resistance and is observed to increase steadily from short-circuits loads with peaks at the matching impedance loads (100 kΩ) and decreases for the open-circuit loads.
- The LCO amplitude and harvested energy for the square section show a significant increase when compared to the rectangular section in all cases.
- Buildup time to stationary oscillation increases with decreasing initial wind speed.
- Initial displacement amplitude increases slowly as galloping initiates and then rapidly to steady oscillations.

Chapter 4: Experimental Evaluations

Comprehensive experimental evaluations were conducted in The University of Alabama in Huntsville (UAH) subsonic wind tunnel in order to characterize the performance of baseline and improved GPEH prototypes. First, the experimental setup was presented and detailed dimensions for the piezoelectric beam were tabulated. Then, detailed information of the bump stop was described for the improved GPEH. Both design and fabrication of the bio-inspired bluff body were given. Various tests were performed to collect both structural and electrical time domain responses under different flow conditions. Harvested voltage, LCO amplitude, and system damping were determined from these measurement data and presented for different GPEH prototypes. An optimal bump stop configuration was determined that show a significant reduction in LCO amplitude with less effects on harvested voltage. Furthermore, it is observed that the bio-inspired square bluff body can be used as passive control to tune galloping velocity. Results from this Chapter have resulted in a journal paper published by the Journal of Smart Materials and Structures.

4.1 Experimental Setup

As shown in Figure 4.1, a baseline GPEH is composed of a metal beam, two surface bonded piezoelectric layers, and a tip bluff body with square cross section. Macro-fiber composite (MFC) piezoelectric sheets (Smart Material Corporation, M8528-P2)[1] were bonded to a steel cantilever beam using the M-bond 200 adhesive kit[2]. The tip bluff body made from polyurethane foam is firmly held to the tip section of the piezoelectric beam. Table 4.1 shows the dimensions and properties of the piezoelectric beam. Figure 4.2 shows the experimental setup in a low-speed wind tunnel at the University of Alabama in Huntsville. The test section is 0.3048 m tall, 0.3048 m wide, and 0.61 m long (1 ft x1 ft x 2 ft). The piezoelectric sheets were connected in parallel to form a bimorph configuration across electrical load resistances. Wind velocity was measured using a pitot tube and an anemometer. Turbulence screens smoothen out any swirls in air and the lowest speed of the wind tunnel is 1.9m/s. Keyence laser sensor (LK H152)[3] was used to measure the displacement responses at the location of 170mm away from the clamped end. This location is selected for the best measurement without interfering with the tip bluff body motion. Beam tip displacement is resolved based on the first bending mode

[1] http://www.smart-material.com

[2] http://www.vishaypg.com/docs/11010/bond200.pdf

[3] http://www.keyence.com/products/measure/laser-1d

shape function of a cantilevered uniform beam with a tip mass [6]. A National Instruments (NI) data acquisition (DAQ) system (Model DAQ 6356)[4] was used to record the displacement and harvested voltage under different wind velocities and different resistive loads. In-house resistive voltage divider circuit was built to collect harvested voltage signals in order to meet the DAQ input voltage range of +/-10V. The NI DAQ input impedance is larger than 16MΩ (> 100GΩ in parallel with 10pF) which will not alter the effective impedance of the signal circuit.

Signal post-processing must be conducted in order to extract the frequency components from time domain signals. The NI DIAdem software was used to determine the LCO amplitudes and harvested peak voltage values under different wind velocities and resistive loads. Harvested peak power can be simply calculated based on the voltage and corresponding resistance in the circuit. To ensure a reliable electrical contact during experimentation since the contact leads are closer to the clamp end, a small gap $Lm=2mm$ is allowed between MFC and clamp.

[4] http://sine.ni.com/ds/app/doc/p/id/ds-163/lang/en

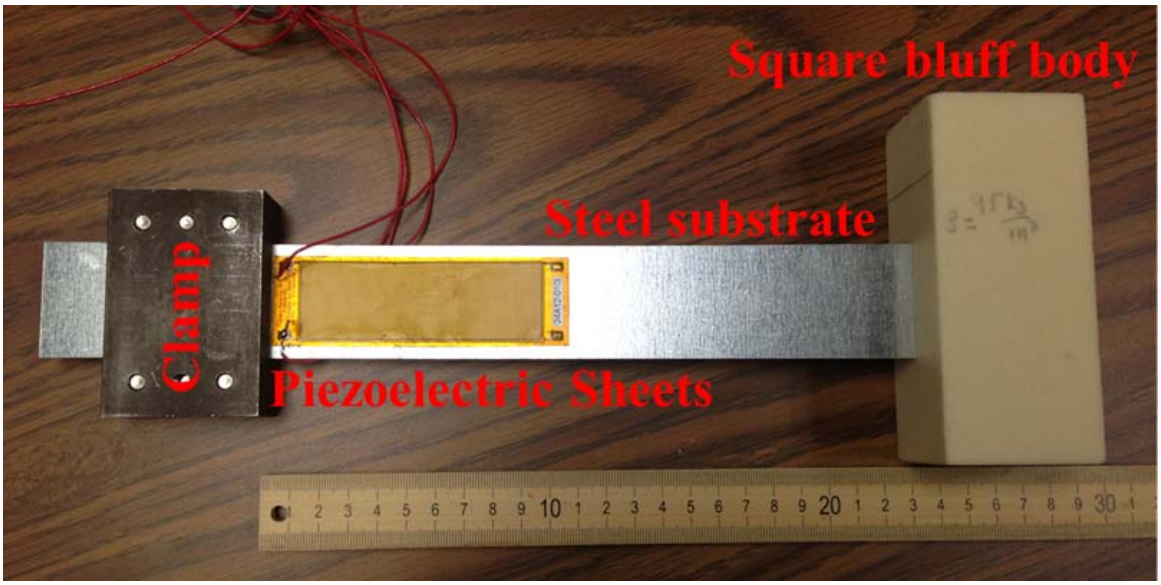

Figure 4.1: Baseline GPEH Prototype

Table 4.1: Baseline GPEH dimensions and material properties

Steel Beam	
Length from clamp (L_b) mm	228
Length MFC from clamp (L_m) mm	2
Width (b) mm	40
Thickness (h_b) mm	0.4
Young's Modulus (E) GPa	200
Density (ρ_b) kg/m^3	7850
MFC (M8528-P2)	
Active Length (L_p) mm	85
Active Width (b_p) mm	28
Thickness (h_p) mm	0.3
Overall Length (mm)	103
Overall Width (mm)	31
Piezoelectric coupling term (Θ) v/m	-2421.03
Capacitance (nF)	422
Area Density (g/cm^{-2})	0.16
Tip Bluff Body (Polyurathane Foam)	
Density (g/cm^{-3})	0.095
Length (l) (mm)	100
Width (h) (mm)	50

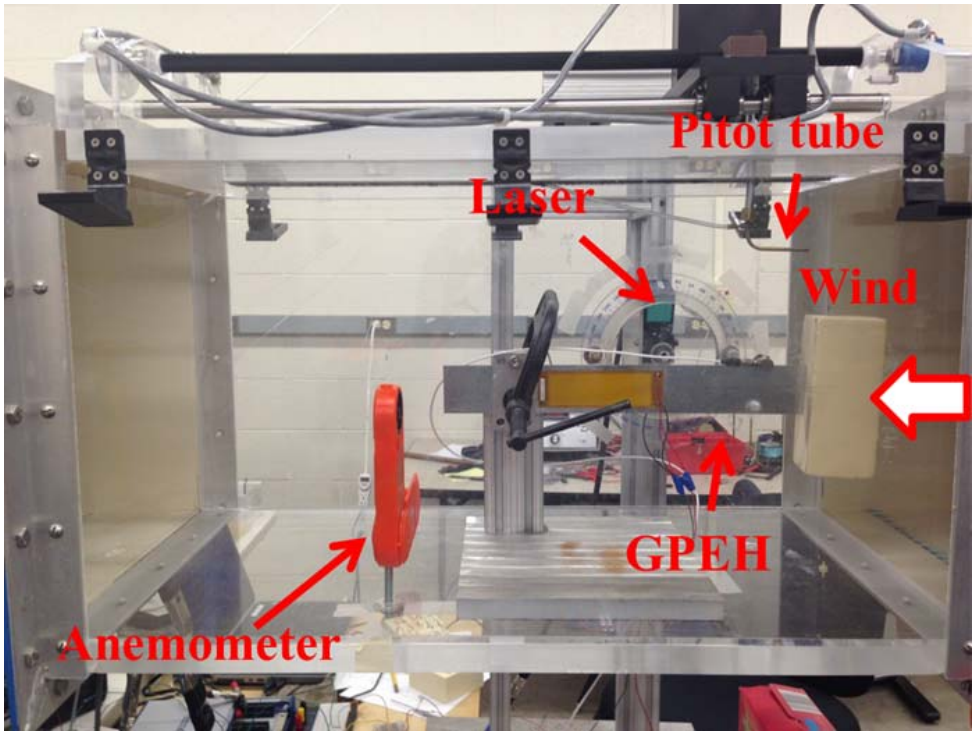

(a)

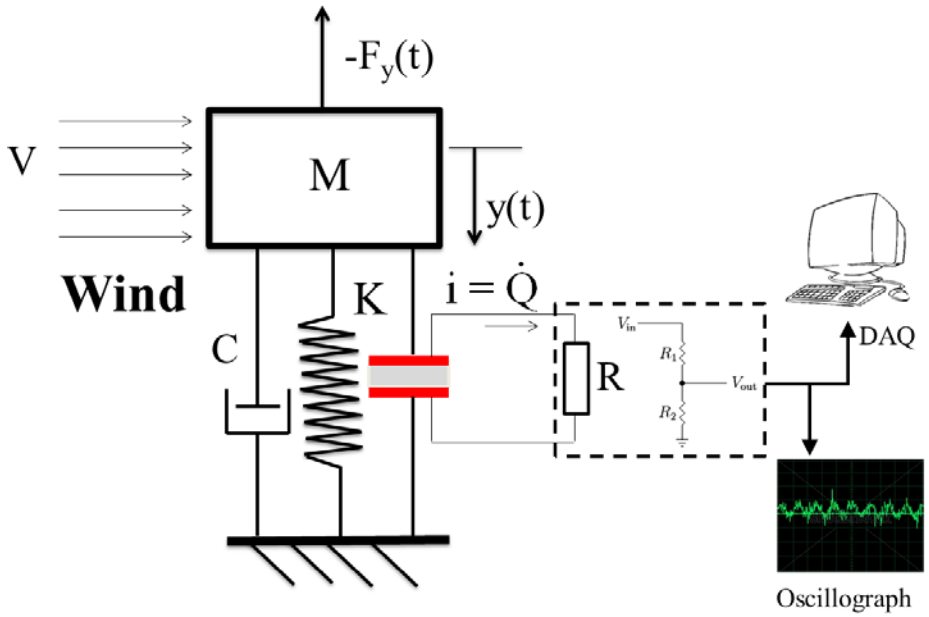

(b)

Figure 4.2: GPEH (a) Test section of wind tunnel (b) Instrumentation schematic

4.2 GPEH with bump stop

Figure 4.3 shows a baseline GPEH whose substrate cracked during experiments after about 600k cycles. Thus, a new design is needed to reduce bending stress thereby prolonging the life-span of such GPEH.

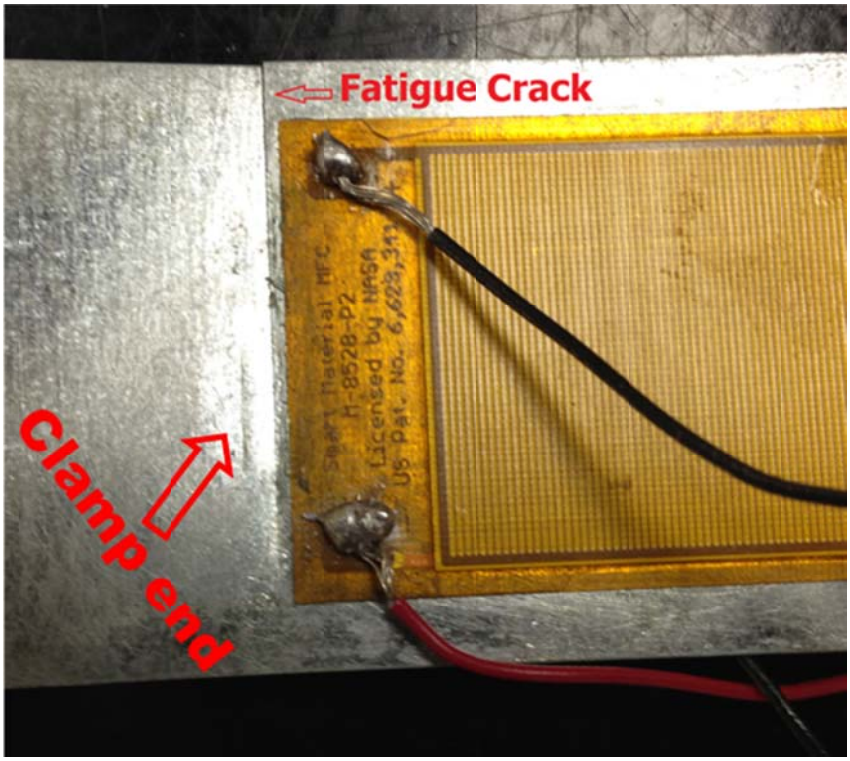

Figure 4.3: Fatigue damage on substrate of test piezoelectric beam

The concept of an impact bump stop was adopted in the improved GPEH design, as shown in Figure 4.4. The gap size (L_{Gap}), stop location (X_s), and contact area are selected as three critical parameters to define the bump stop system. Experiments were conducted to investigate the bump stop effects on the GPEH performance. The goal is to reduce the GPEH LCO amplitude while maintaining

comparable harvested power. Moreover, in order to determine the optimal bump stop design we vary the stop gap size, surface area dimensions and stop location as listed in Table 4.2.

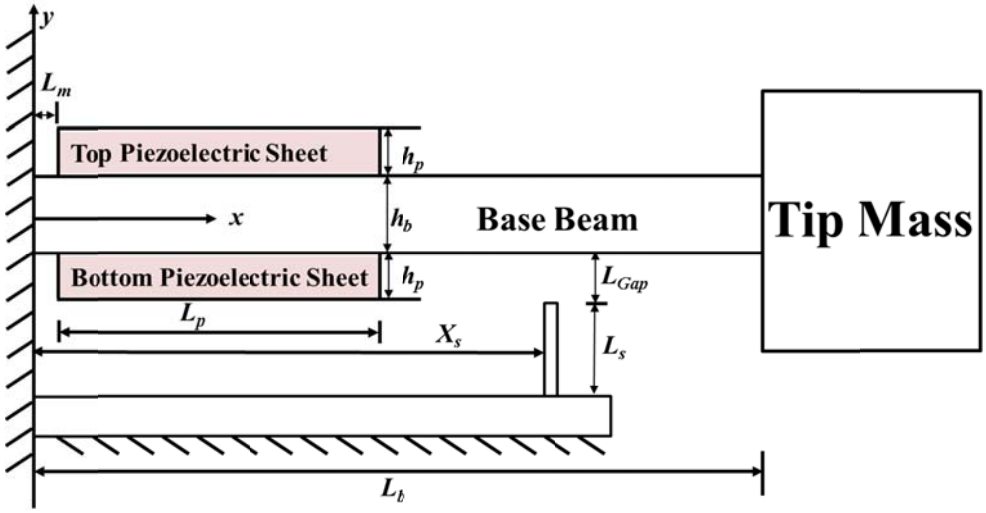

Figure 4.4: Schematic of the improved GPEH

Table: 4.2: Bump Stop Parameters

Parameter	**mm**	**%**	**mm**	**%**	**mm**	**%**
Gap Size (L_{Gap})	3	1	5	2	7	3
Stop Location (X_s)	130	57	150	66	170	75
Stop Width (b_s)	40	18	40	18	40	18
Stop Length (L_s)	3.175	1	12.7	6	25.4	11
Stop Thickness (h_s)	12.7	6	3.175	1	3.175	1

4.3 Bio-inspired Square Bluff Body

A GPEH with bio-inspired square bluff body was developed to study the effects of the spanwise waviness on exploiting wind energy from galloping aeroelastic

instability. Different bluff bodies with sinusoidal waviness on its leading edge were tested.

4.3.1 Geometry of Bio-inspired Bluff Body

Typically, the length of the square cross-section is sufficient to define the standard length scale for the straight faced bluff body. We now define two additional length scales similar to that of Darekar and Sherwin to fully describe the bluff body with spanwise wavy leading edge [44]. The free stream velocity V is aligned with the x-axis (reverse streamwise direction), oscillatory motion is aligned with the y-axis (transverse direction) while the span of the prism is aligned with the z-axis (cross-flow direction) (see Figure 4.5). The peak to peak amplitude A, wavelength λ and cross-section length L fully defines the wavy cylinder. From Figure 4.5a the waviness can be express mathematically as:

$$\varsigma(z) = \frac{A}{2} - \frac{A}{2}\cos\left(\frac{2\pi}{\lambda} z\right) \tag{4.1}$$

Differentiating (4.1) with respect to z to determine the slope of the waviness gives:

$$\frac{d\varsigma}{dz} = \pi \frac{A}{\lambda}\sin\left(\frac{2\pi}{\lambda} z\right) = S_A \sin\left(\frac{2\pi}{\lambda} z\right) \tag{4.2}$$

Where S_A is the largest magnitude of the slope and a function of $\frac{A}{\lambda}$. Therefore two independent length parameters can be defined as [43-44]:

$\frac{\lambda}{h}$ = Spanwise to vertical spacing ratio, and

$\frac{A}{\lambda}$ = Wave steepness

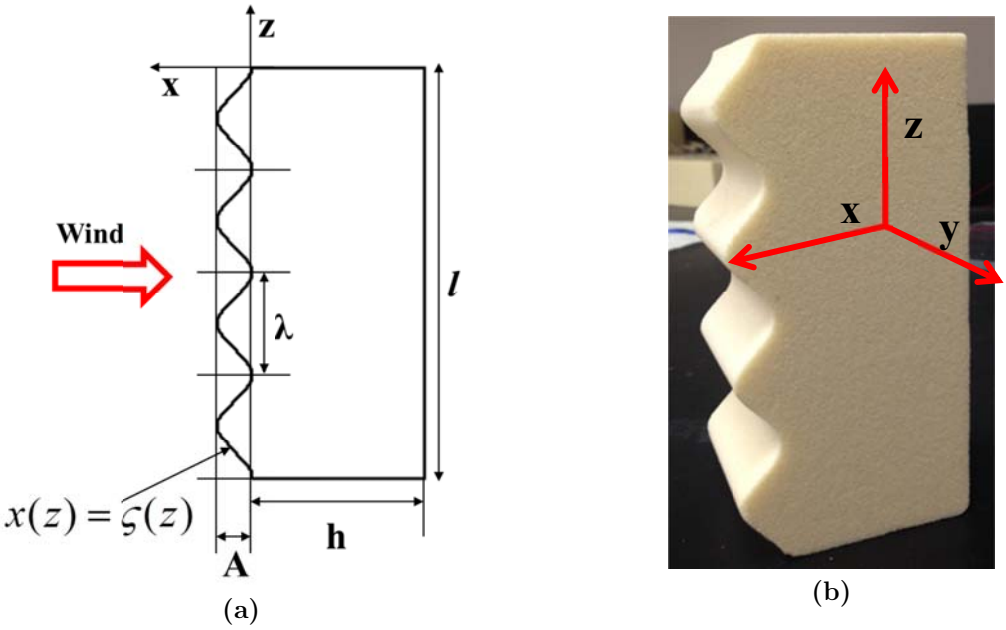

(a) (b)

Figure 4.5: Specification of waviness on bluff body with 4 full waves; (a) Schematic (b) Test specimen

Table 4.3: Baseline Bio-inspired Bluff Body Properties

Length Parameters	Sine I	Sine II	Sine III	Sine IV
λ/h	2.4	1.2	0.8	0.6
A/ λ	0.0833	0.167	0.2500	0.3333

[M=29.7g, Sine # = number of full waves]

4.3.2 Fabrication and Tests

A table for the leading edge wavy trajectory is made is MS Excel using (4.1). The curve by table feature in Solid Edge is used to make a CAD model. Materials are removed symmetrically through the back face to ensure the bluff bodies have

the same weight. This 3D CAD model is now fed into a CNC machine used to cut the wavy profile on the leading edge of the square cross-section bluff body.

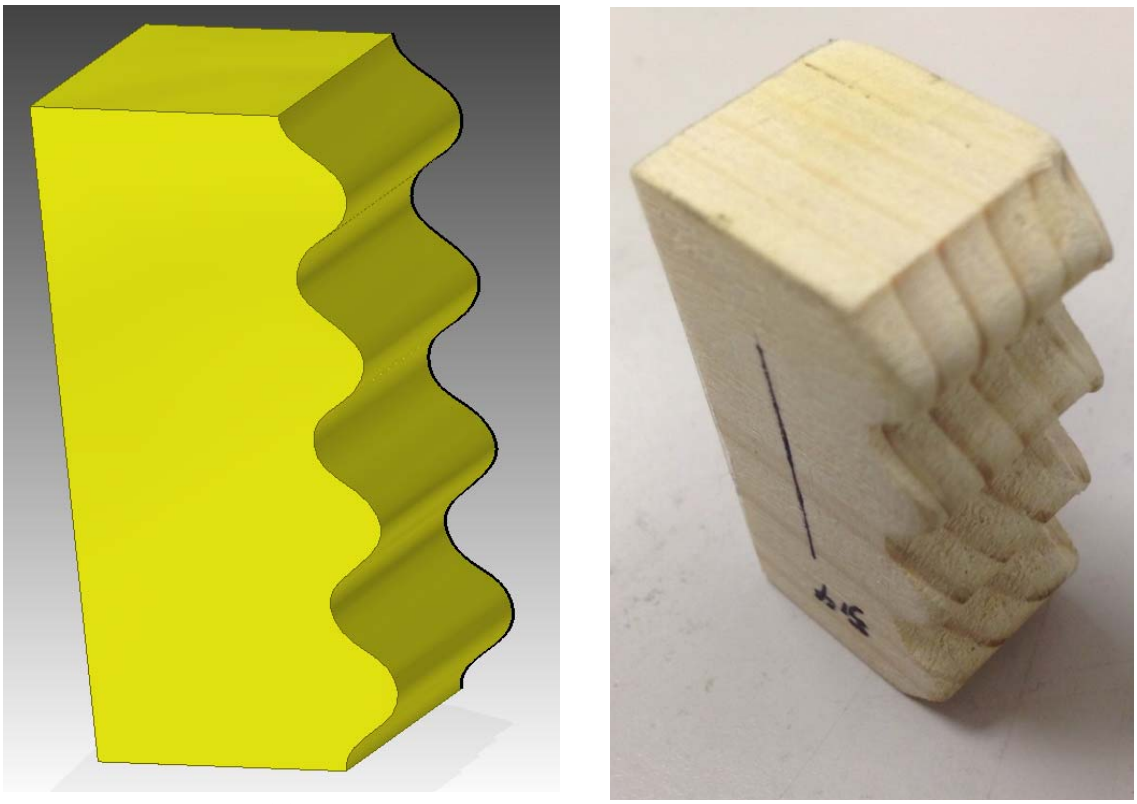

(a) **(b)**

Figure 4.6: Bio-inspired bluff body; (a) CAD Model (b) CNC machined prototype

Two separate tests were conducted; first for four bluff bodies of the same mass and material as the baseline square cross-section bluff body with length parameters as shown in Table 4.3. Fixed 100kΩ load is connected across the piezoelectric sheets while wind velocity is varied from 2m/s – 4m/s. Details of the second test conducted on scaled prototypes are presented in 6.2.

4.4 Baseline GPEH Measured Data

4.4.1 Time history of measured data

The baseline GPEH is tested under different electrical load ranging from 10kΩ to 1MΩ and different wind velocity ranging from 2m/s to 8m/s. Time history voltage and displacement responses are shown in Figure 4.7. The self-excited nature of the galloping phenomenon requires initial perturbations to grow until a steady state response is reached [35,89].

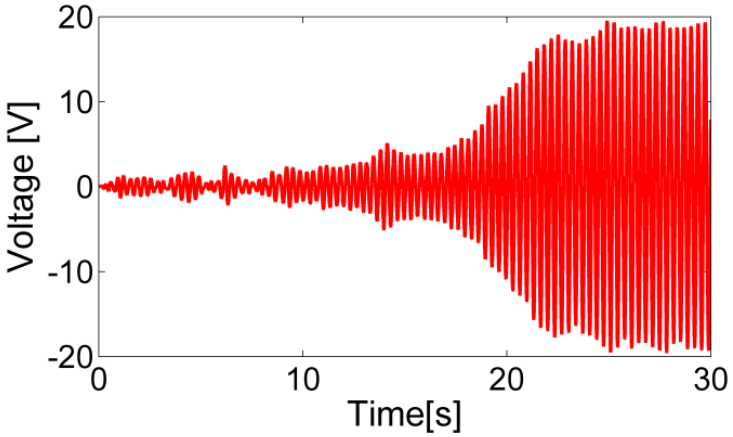

(a)

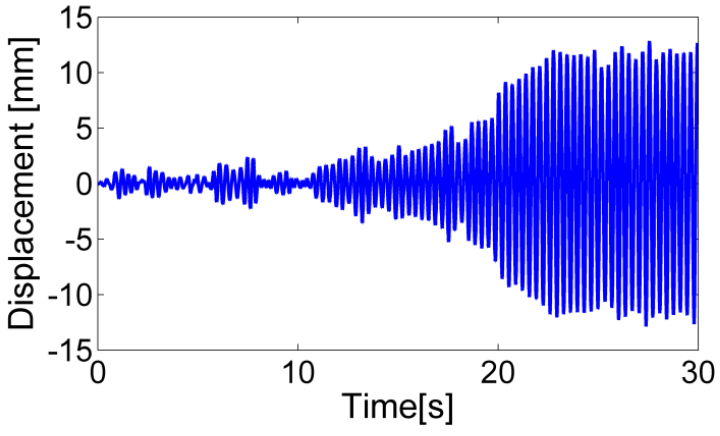

(b)

Figure 4.7: Measured time history responses of the baseline GPEH; V = 4m/s and R = 220kΩ: (a) Voltage (b) Displacement

Measured time domain data of electrical response and displacement from rest until steady oscillations (Figure 4.8) provide physical insights. Moreover, the effect of inertial of the wind tunnel accoutrements was evaluated in these initial checks.

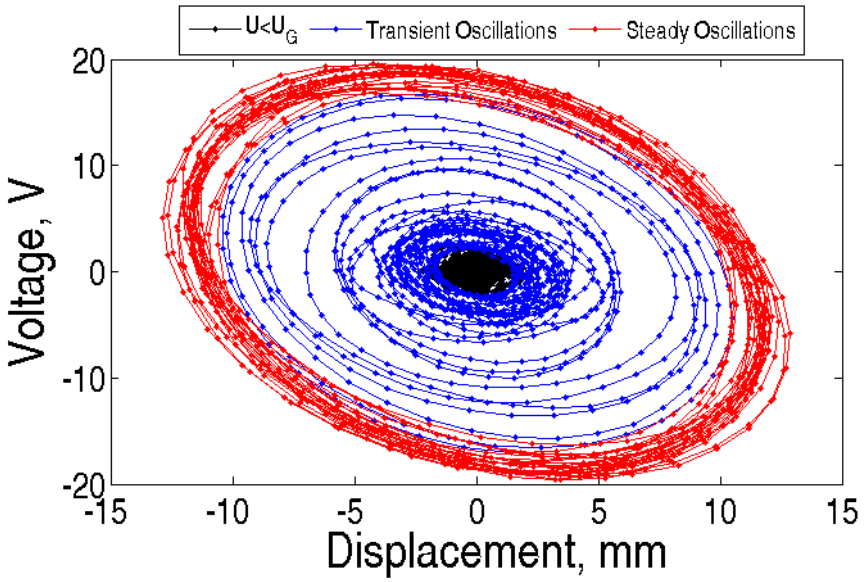

Figure 4.8: State space representation of measured system response for baseline GPEH: V= 4m/s and R=220kΩ

The first zone shows the minimal effect of inertia from wind tunnel motor, while readings were taken for a delay period of 5s before wind is turned on. When wind is turned on (still first zone), notice initial perturbations as fluid forces tries to overcome system damping. The displacement amplitude slowly increases (second zone) as galloping initiates. The perturbations grow until steady oscillation is reached in the third zone at about 22s from start. Knowing the buildup time to steady oscillations to be about 17s, we delay a minimum of 30s before readings are taken for this wind speed. In theory, the steady oscillations should collapse into a

single orbit but the fluctuations noticed are due to the varying system damping and angle of attack. The spirals do not intersect; so a complete plot would be three dimensional where the third axis is wind velocity showing the three coupled states: aero-electro-mechanical system.

4.4.2 Harvested Voltage and LCO Amplitude

Measured voltages and calculated power under different wind velocities and electrical loads are shown in Figure 4.9. The voltage increases with increasing wind velocity if electrical load is fixed. The maximum peak voltage is 50v with the 470kΩ electrical load and the maximum peak power is 13mW with the 100kΩ electrical load. The calculated optimal resistance load for the maximum power output is 125.7kΩ, which is very close to the actual value. It is determined from the time constant in a RC circuit.

$$R = \frac{1}{\omega C_P} = 125.7k\Omega \tag{5.1}$$

Here, ω is the measured galloping frequency, i.e., $\omega = 3\text{Hz}$. C_p is the capacitance of the piezoelectric materials. In this calculation, we neglected the finite leakage resistance in the piezoelectric materials [97].

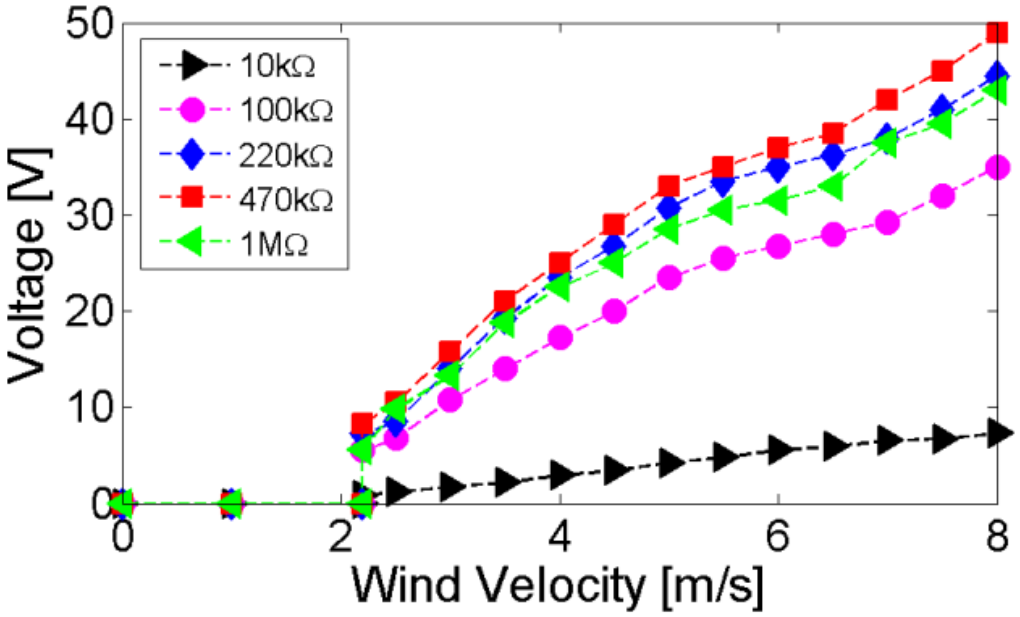
Voltage [V]
Wind Velocity [m/s]
10kΩ
100kΩ
220kΩ
470kΩ
1MΩ
0
10
20
30
40
50
0
2
4
6
8

(a)

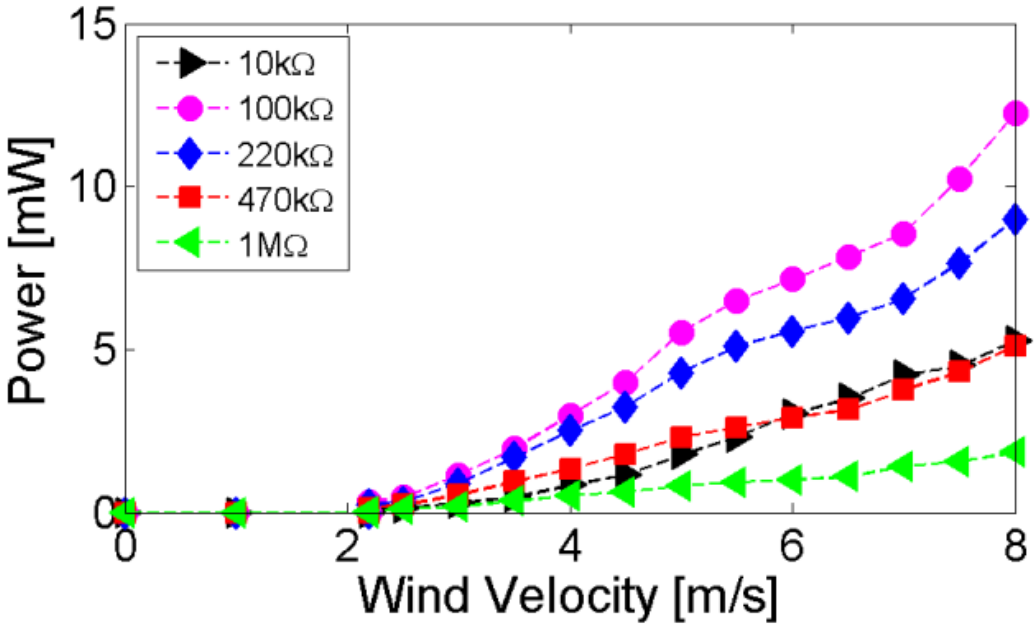
Power [mW]
Wind Velocity [m/s]
10kΩ
100kΩ
220kΩ
470kΩ
1MΩ
0
5
10
15
0
2
4
6
8

(b)

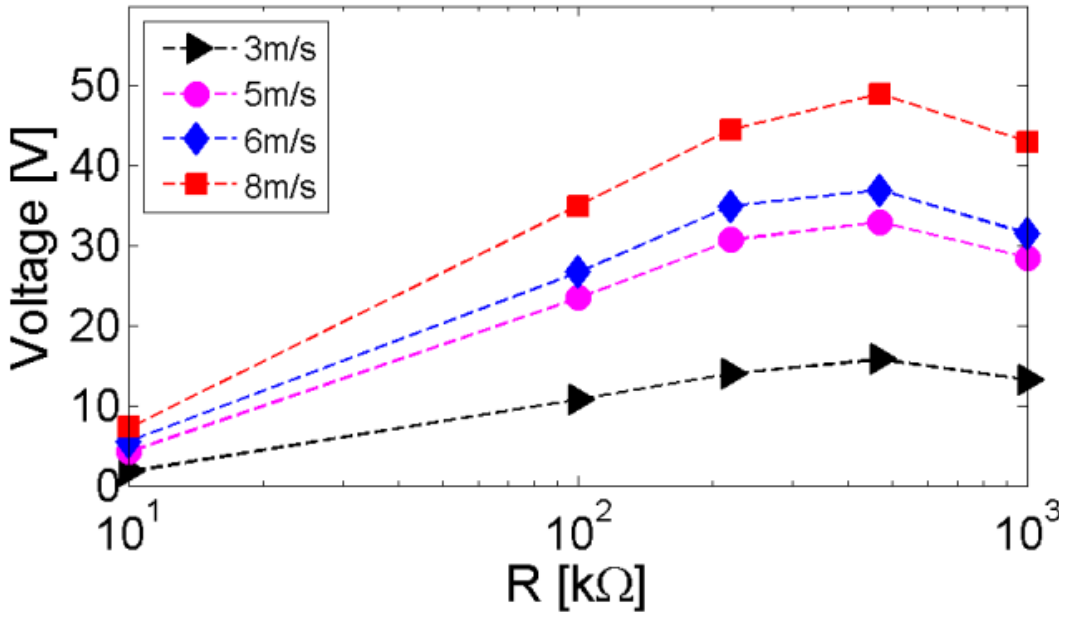

(c)

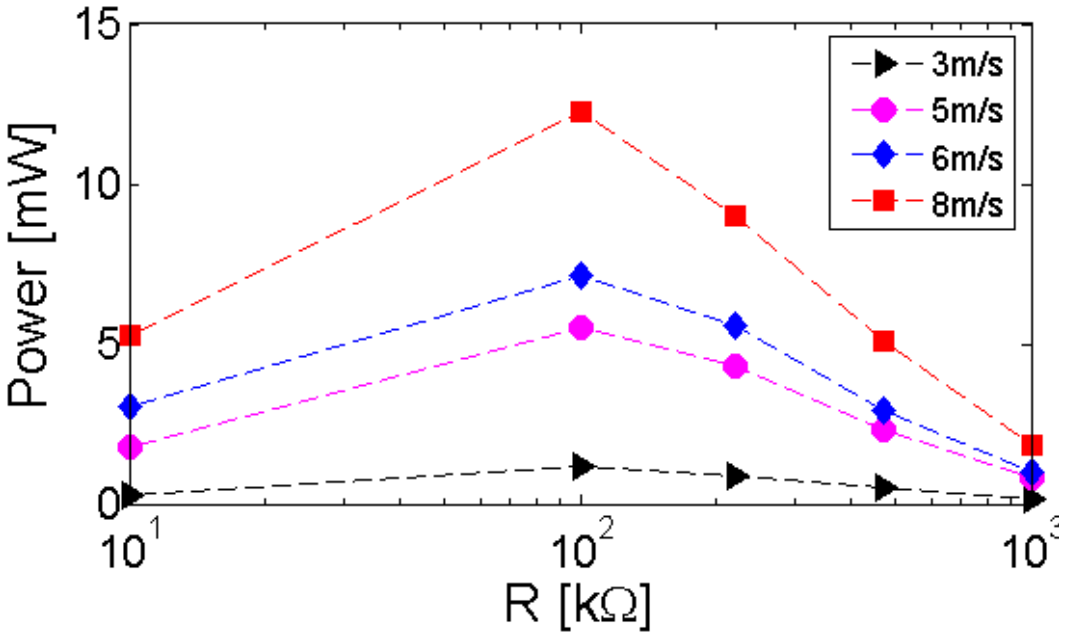

(d)

Figure 4.9: Measured baseline GPEH data: (a) Peak voltage vs. wind velocity (b) Calculated power vs.wind velocity (c) Peak voltage vs. resistance (d) Calculated power vs. resistance

Figure 4.10 shows the variation of LCO amplitude with electrical loads under different wind velocities. When the electrical load is fixed, LCO amplitude

increases monotonically with wind velocity. When the wind velocity is fixed, LCO amplitude shows a nonlinear curve. It starts to decrease as the electrical load increases. Then it reaches to a minimum value in which the electrical load generates the maximum voltage in piezoelectric materials. Finally, it slowly increases toward to the open circuit electrical load.

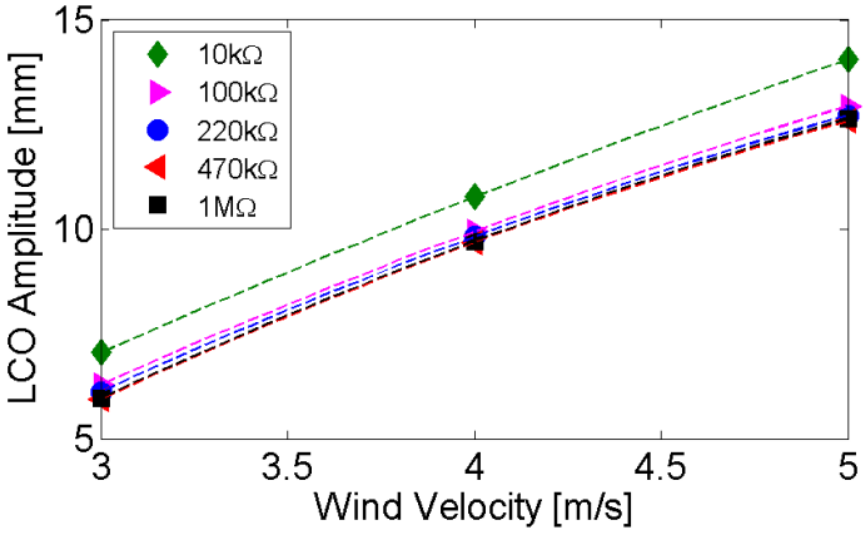

(a)

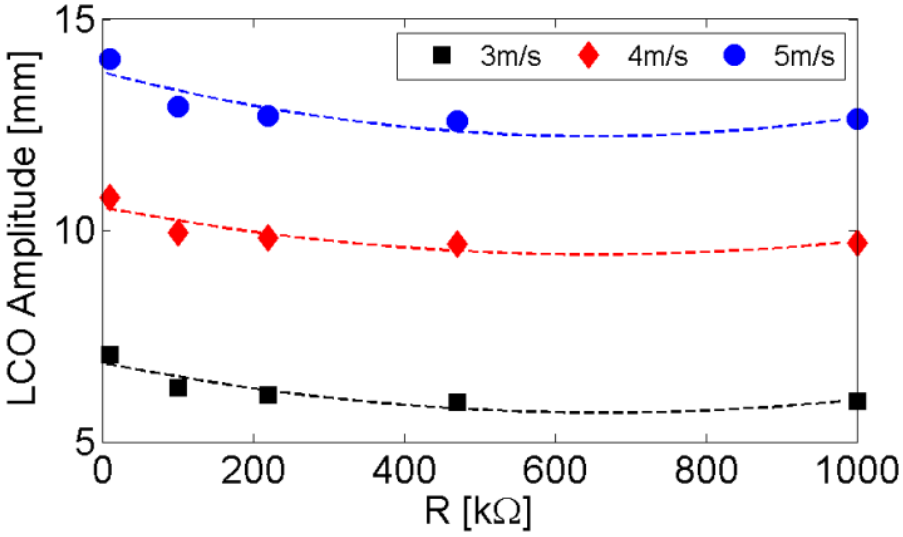

(b)

Figure 4.10:Variation of LCO amplitude with: (a) wind velocity (b) electrical load

4.4.3 Damping

When the GPEH undergoes limit cycle oscillation, if the wind tunnel airflow is shut down transient response can be collected. Figure 4.11 shows the decayed response for both harvested voltage and beam displacement of a GPEH connected with the electrical load of 100kΩ and tested at 4m/s wind velocity. The logarithmic decrement technique was used to determine the damping coefficient under different wind velocity ranging from 3m/s to 5m/s and different electrical loads varying from 10kΩ to 1MΩ.

Characteristically, the galloping frequency is very close to the fundamental frequency of the piezoelectric beam system [85,87]. Corresponding system damping ratio can then be calculated as shown in Figure 4.12. Clearly, it heavily depends on both electrical load and wind velocity. The higher the wind velocity, the higher system damping will be when the electrical load is fixed. When wind velocity is fixed, the system damping shows a reverse trend compared to the LCO amplitude results. It starts from a low value at short circuit and reaches the peak value when the electrical load yields the maximum voltage output.

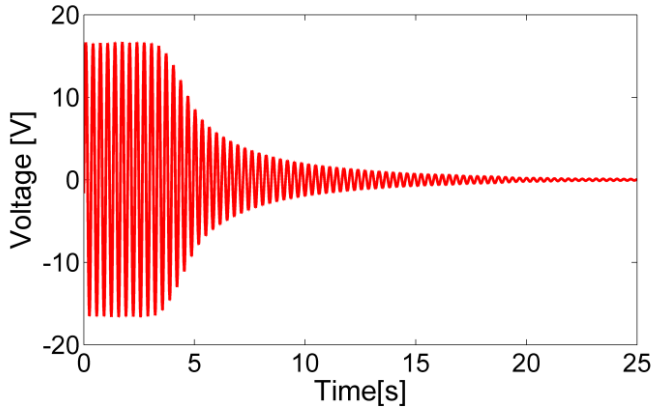

(a)

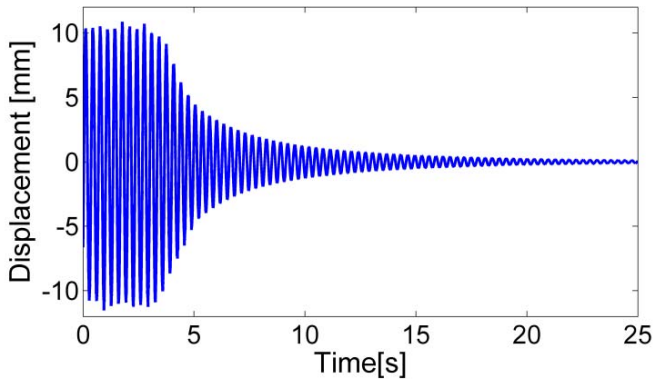

(b)

Figure 4.11: Transient response of baseline GPEH; V = 4m/s and R = 100kΩ: (a) Voltage (b) Displacement

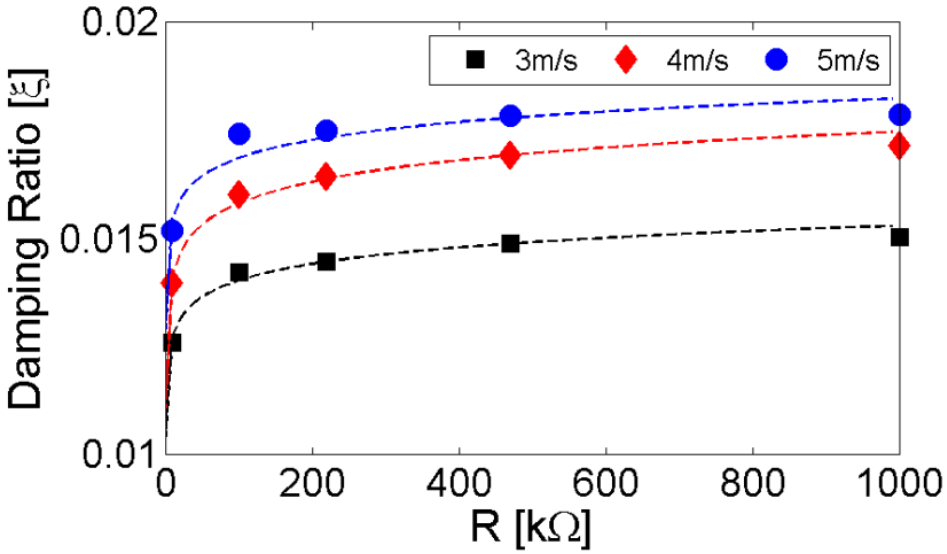

Figure 4.12: Variation of damping ratio with electrical load at different wind velocities

4.4.4 Summary (Measured Data Baseline GPEH)

Baseline GPEH with a square cross-section bluff body was comprehensively evaluated in the wind tunnel. The maximum peak harvested power is 13mW under 8 ms^{-1} wind velocity. Voltage and displacement signals are acquired in the time domain; system damping was evaluated using logarithmic decrement and the measured data was used to validate model predictions. Key conclusions are summarized below.

- Harvested voltage increases with increasing wind velocity and load resistance, while maximum peak power is 13mW with an optimal electrical load of 100 kΩ.

- System damping increases monotonically with wind velocity but is lower at open and short circuit loads and reaches the highest value when the corresponding electrical load yields maximum energy extraction.

- LCO amplitude also increases with wind velocity. It has a reverse trend as demonstrated in the damping data when varying the electrical load.

4.5 Experimental Evaluations on GPEH with bump stop

4.5.1 Time history of measured data

At rest the substrate is not in contact with the stop, but as incident wind in the axial direction initiates galloping, the beam deflection is confined due to the bump stop. Comprehensive experimental evaluations were conducted under a fixed electrical load of 100kΩ (i.e., the optimal load for the maximum power in the baseline GPEH) and different wind velocity ranging from 3.5m/s to 5.5m/s. Note that the overhung beam length is used as the reference length. Both electrical response and structural responses were acquired accordingly using the same DAQ system. Slightly higher oscillation frequency is noticed for the bump case (Figure 4.13) and since galloping takes place at the fundamental mode of the harvester, analyzing higher modes did not suffice.

a. Time History Data When Varying Bump Stop Location

Typical steady state response data of harvested voltage and displacement are shown in Figure 4.14. Note that tip displacement data were plotted and the impact occurred at 5mm offset the beam rest position, as indicated by a horizontal line in Figure 4.14b. Additional dynamics introduced by the bump stop affects both electrical and structural responses. Roughness in the voltage signals is obvious while the displacement shows quite smooth response but has an asymmetric

waveform. High frequency contents (see Figure 4.13) and transient effects due to the impact significantly affect electrical responses but have less effect on the structural response. Comparable electrical responses are obtained with substantial reduction in structural responses. This suggests that although the stop confines the beam motion there is induced strain on the beam due to unsteady aerodynamic force acting on the tip mass during the impact.

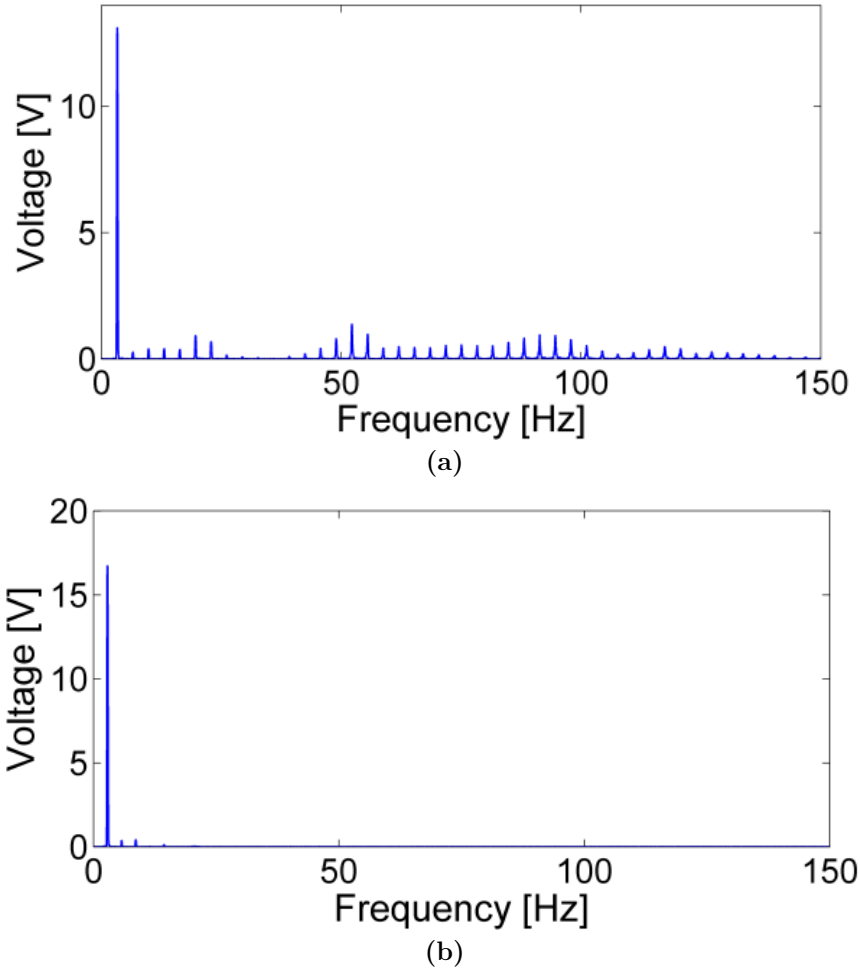

Figure 4.13: Frequency spectrum of voltage signal at V=4m/s and R=100kΩ: (a) Bump case (LGap=5mm, Xs=130mm) (b) Baseline

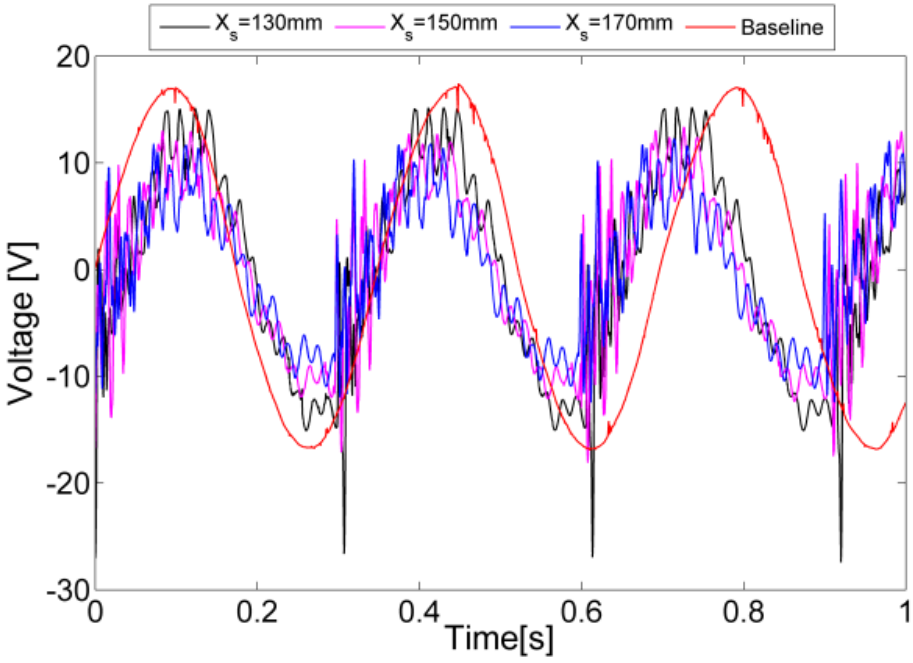

(a)

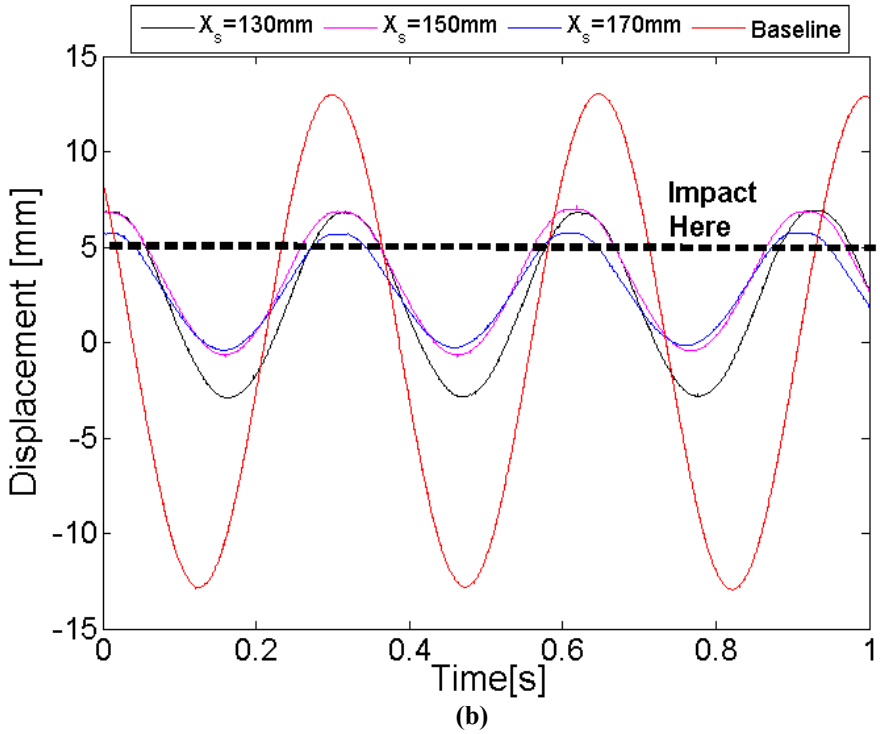

(b)

Figure 4.14: Measured system responses of improved GPEH when varying stop location: L_{Gap}=5mm, V=4m/s, R=100kΩ: (a) Voltage (b) Tip displacement

Three bump stop locations were tested. Higher spikes in the voltage responses were observed when the bump stop is located close to the clamped end, i.e., X_s=130mm. Equivalently, the bump stop introduces an additional boundary condition (clamped-pin-free instead of clamped-free) and increases the strain responses in the piezoelectric materials. Note that the piezoelectric layers are bonded close to the root.

b. Time History Data When Varying Bump Stop Gap Size

Steady state electrical and structural response data are shown in Figure 4.15 when varying the bump stop gap size. Similar voltage and displacement responses are obtained compared to the previous case. Bump gap size is directly proportional to the displacement response. Typically, the bump stop gap size would be equal to the displacement DC offset value. However, as aforementioned, the tip displacement data were plotted here and the bump stop was located at150mm away from the clamped end.

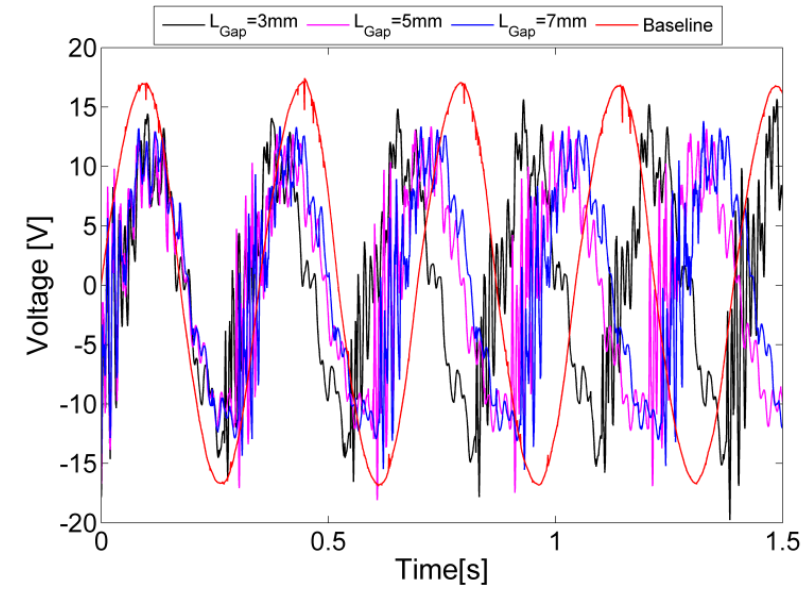

(a)

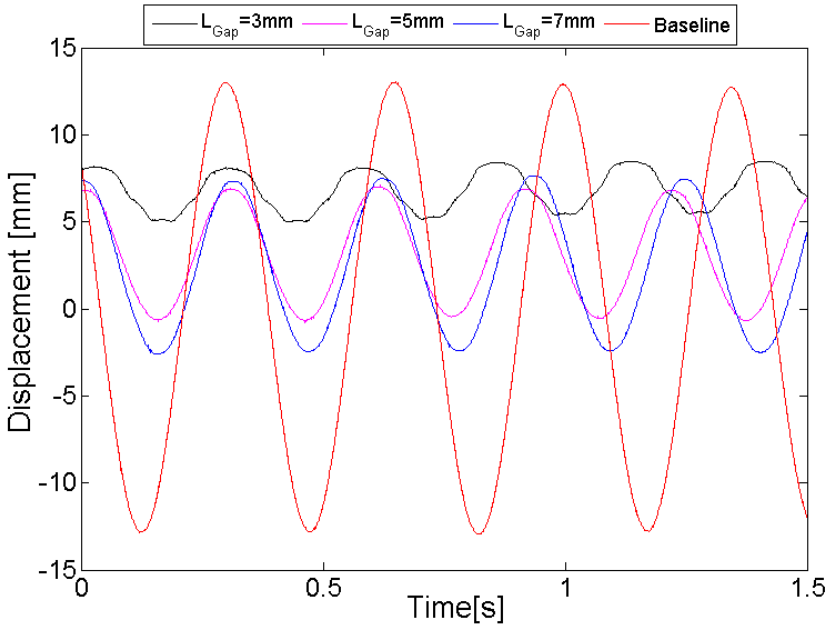

(b)

Figure 4.15: Measured system responses of improved GPEH when varying gap size; Xs=150mm, V=4m/s, R=100kΩ: (a) Voltage (b) Tip displacement

c. Time History Data When Varying Bump Stop Contact Surface Area

Figure 4.16 shows steady state electrical and structural responses when varying contact surface area. It is clear that smaller contact surface area results in large reduction in the displacement amplitude.

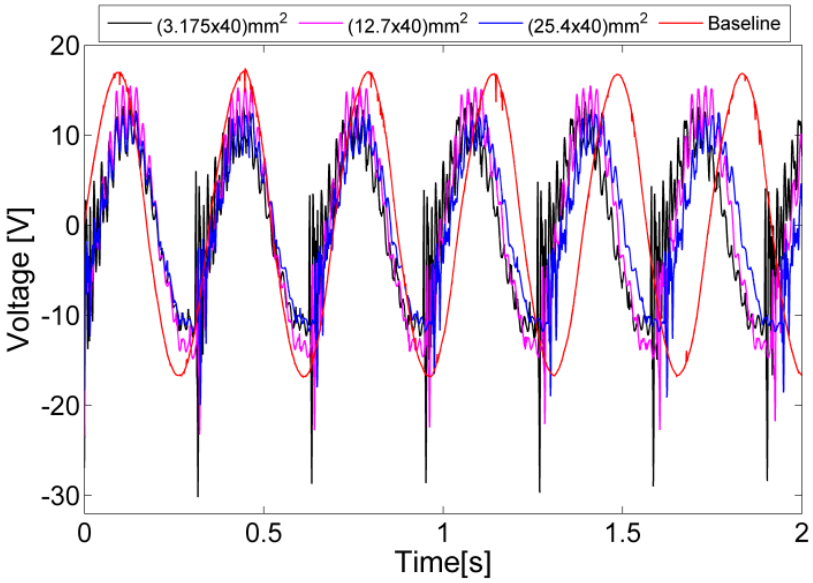

Figure 4.16: Measured system responses of improved GPEH when varying contact area; L_{Gap}=5mm Xs=130mm, V=4m/s, R=100kΩ: (a) Voltage (b) Tip displacement

d. Time History Data When Varying Wind Velocity

Figure 4.17 shows steady state electrical and structural responses when varying wind velocity. Note that there is about 4mm DC shift in the displacement response when increasing the wind velocity from 3.5m/s to 5.5m/s. This is due to inertia; the imbalance caused in momentum (retrieving force) of the beam as it impacts on the stop. Without the bump stop, as long as the aerodynamic force is acting on the tip mass; inertial force ensures continuation of the beam's motion which is disrupted in the event the beam impacts a stop. As wind velocity increases, an increase in the aerodynamic force induces higher impact force and the beam returns much less. This is why the stop is placed only on one side and this phenomenon is similar to that observed in Figures 4.14, 4.15 and 4.16 when we vary the bump stop design parameters.

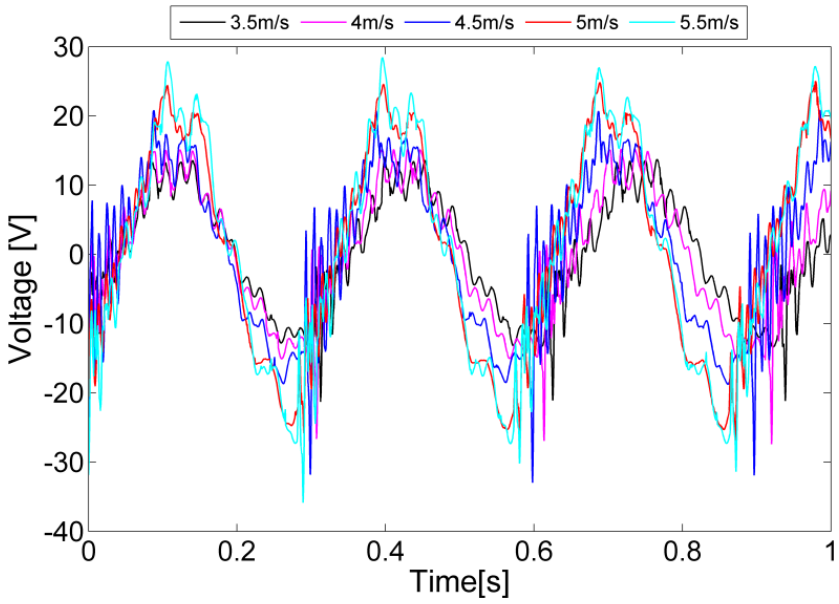

(a)

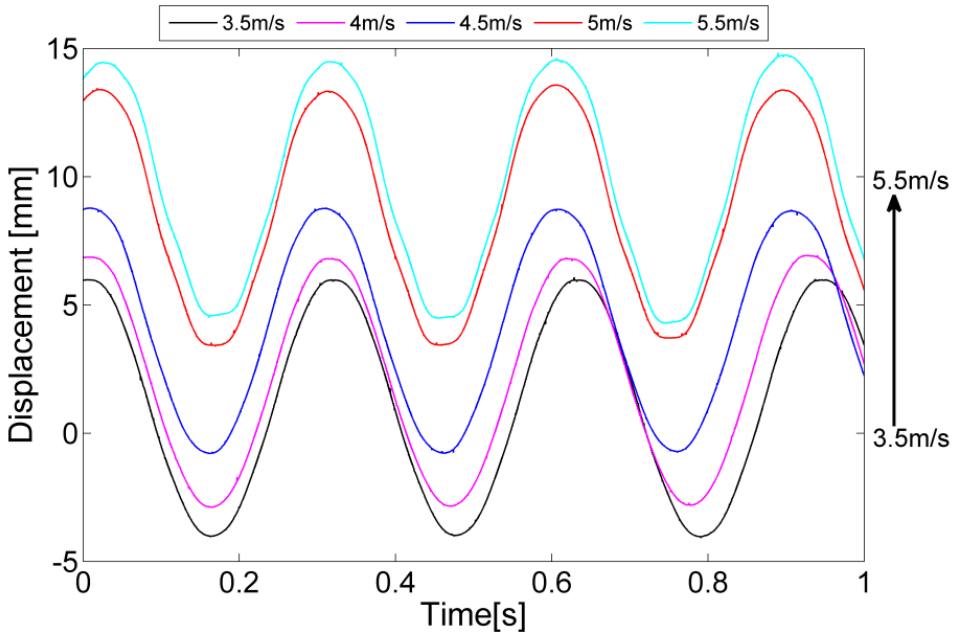

(b)

Figure 4.17: Measured system responses of improved GPEH when varying wind velocity, L_{Gap} = 5mm, Xs=130mm, R=100kΩ: (a) Voltage (b) Tip displacement

4.5.2 Optimal Bump Stop Design

As shown in Table 4.2, we tested all combinations when varying three bump stop design parameters. In this section, we expect to determine the effect of each parameter on the harvested voltage and LCO amplitude as a function of wind velocity. Finally, an optimal bump stop design can be realized.

a. Bump Stop Gap size

As shown in Figure 4.18, LCO amplitude increases monotonically with increasing gap size when stop location and contact area are fixed. Electrical output increases with wind velocity in all cases. Higher harvested voltage is observed when the gap size is 2%, i.e., L_{Gap} =5mm.

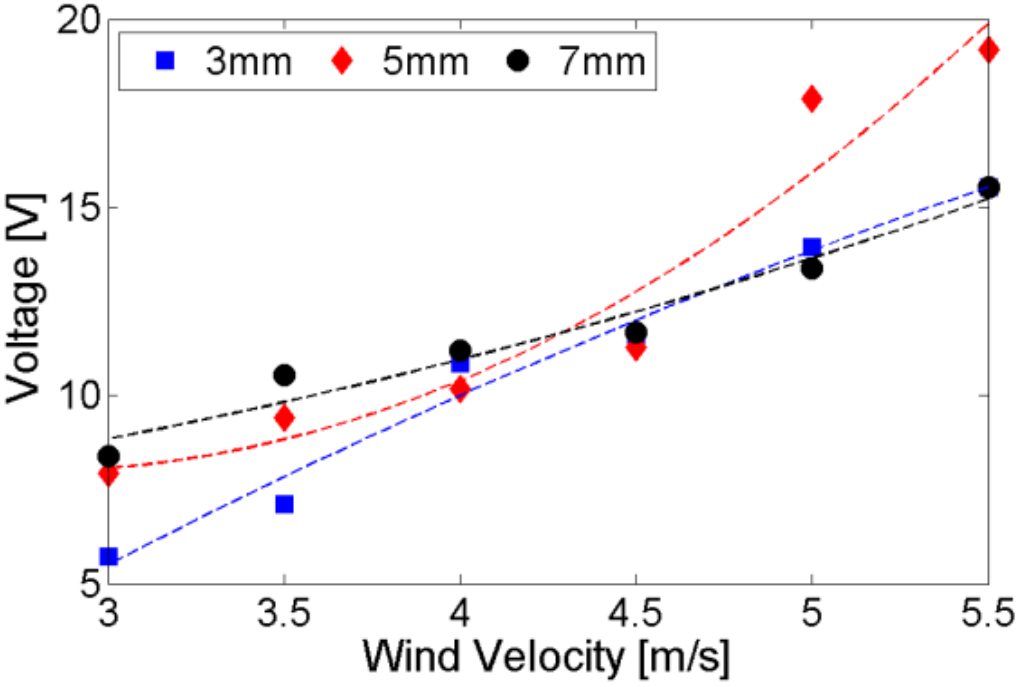

(a)

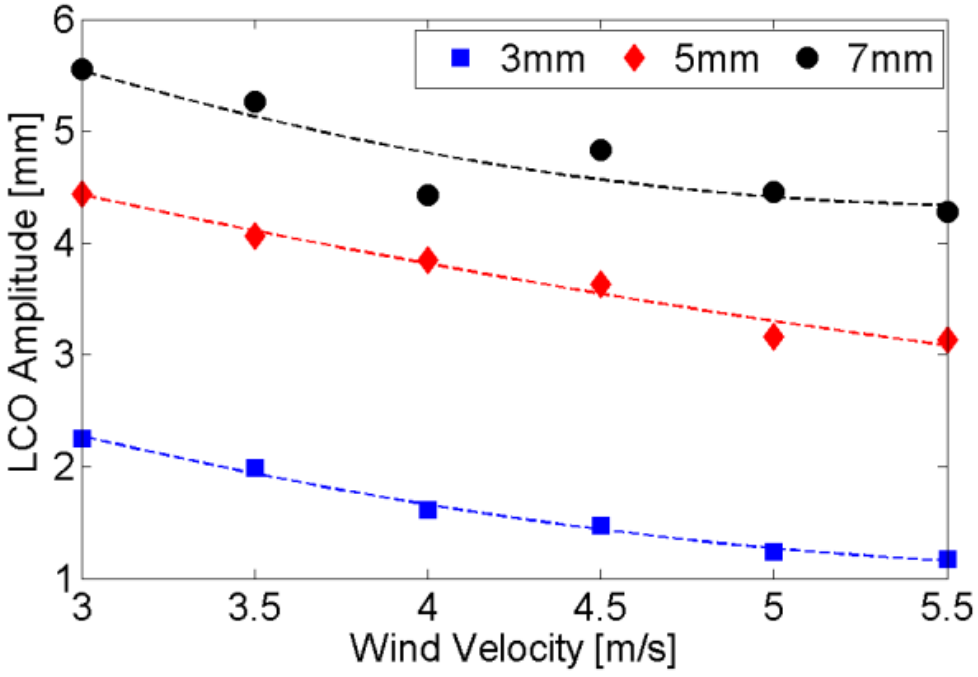

(b)

Figure 4.18: Effect of gap size on improved GPEH; Xs= 150mm, Contact area= (3.175x40)mm², R=100kΩ: (a) Voltage (b) LCO Amplitude

b. Bump Stop Location

LCO amplitude and harvested voltage reduces with increasing stop location when the gap size and contact area are fixed as shown in Figure 4.19. The optimal stop placement is at 57% from the clamped end, i.e. Xs=130mm. Observe the LCO amplitude plot for L_{Gap}=3mm Xs=130mm seems to be a straight line (Figure 4.19b). It is the closest test point of the stop to the beam (i.e. 1% and 57%). This is because at the lowest test wind velocity (3m/s) the beam's center of oscillation has shifted almost the gap size of 3mm so that the displacement amplitude is constrained by the stop, although aerodynamic forces on tip mass continues to induce electrical output.

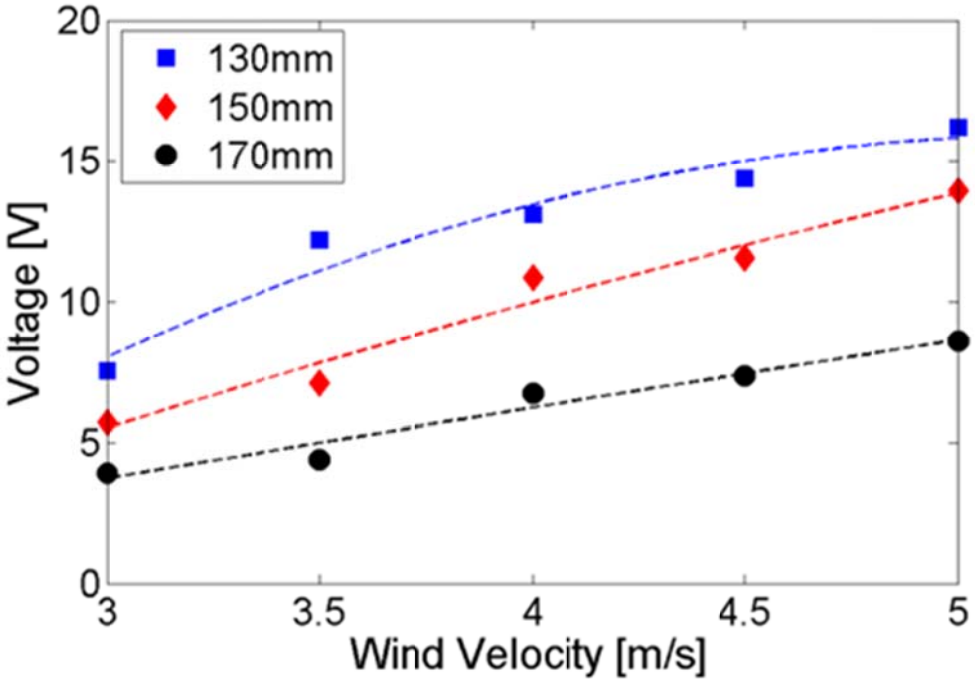

(a)

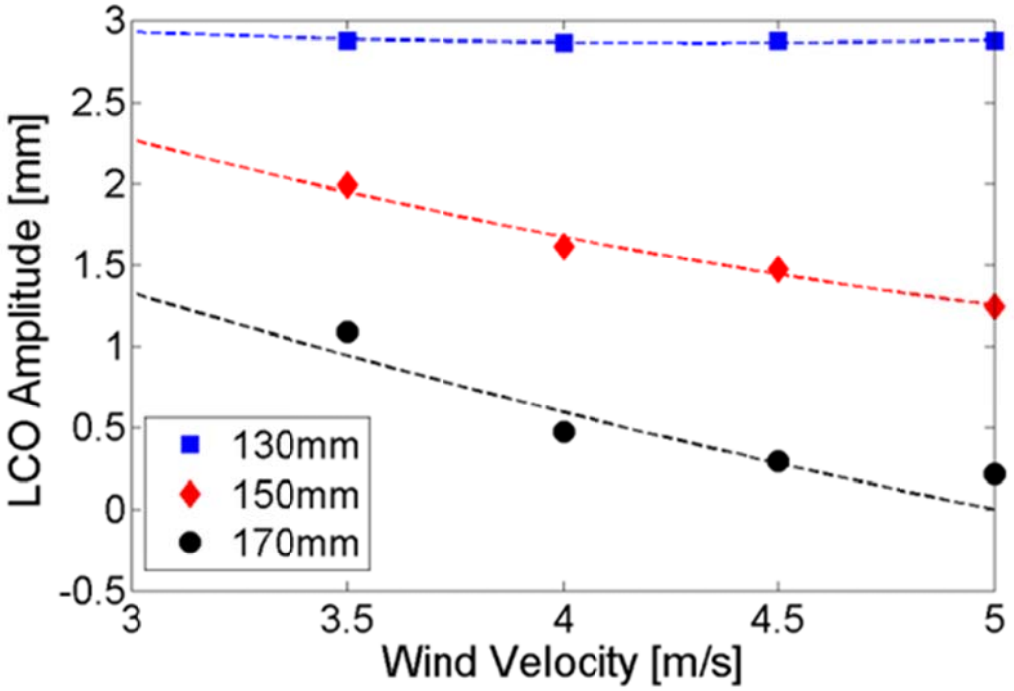

(b)

Figure 4.19: Effect of stop location on improved GPEH; L_{Gap}=3mm, Contact area=(3.175x40)mm2, R=100kΩ: (a) Voltage (b) LCO Amplitude

c. Contact Surface Area

When the gap size and stop location are fixed, LCO amplitude increases with increasing contact area under each wind velocity. The 12.7mm (~6%) case yielded highest harvested voltage response as shown in Figure 4.20.

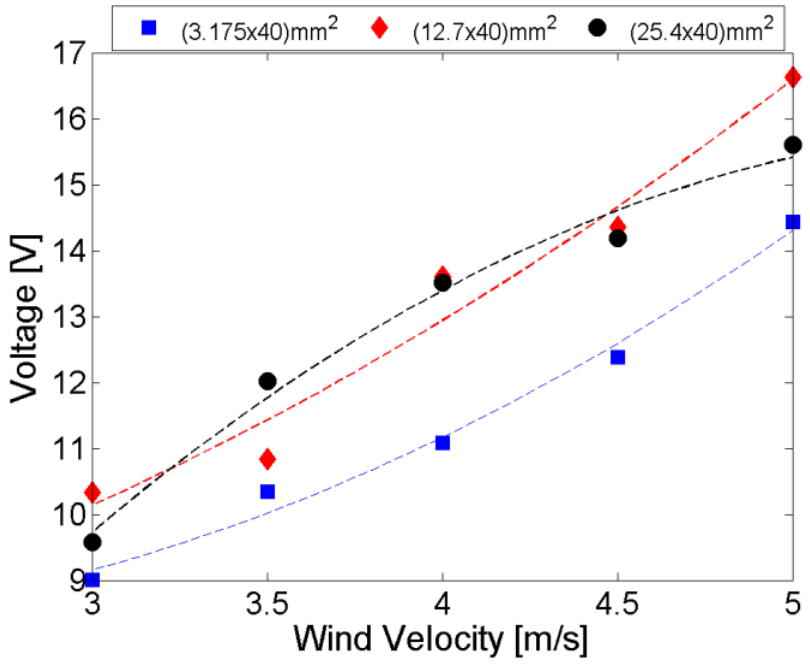

(a)

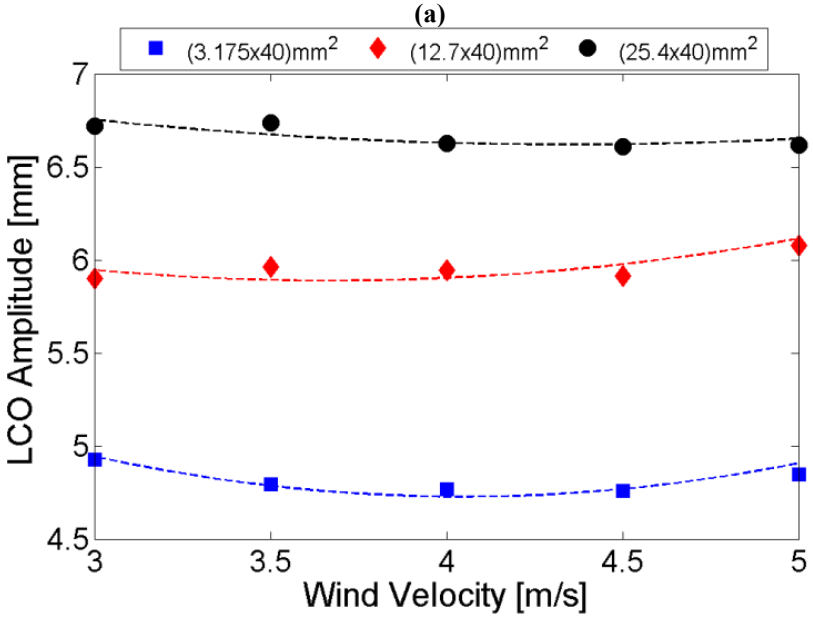

(b)

Figure 4.20: Effect of varying contact area on improved GPEH; L_{Gap}=5mm, Xs= 130mm, R=100kΩ: (a) Voltage (b) LCO Amplitude

d. Harvested Voltage and LCO Amplitude under Optimal Bump Stop Design

The general trend of voltage and LCO amplitude for the improved GPEH compared to that of the baseline GPEH is given in Figure 4.22 with the optimal bump stop design as identified in the previous section. Normalized harvested voltage and LCO amplitude values are shown in Figure 4.21 with respect to the baseline GPEH results. Clearly, the maximum reduction in harvested voltage is 20% while substantial reduction in the LCO amplitude is achieved, which is 70% compared to the baseline GPEH.

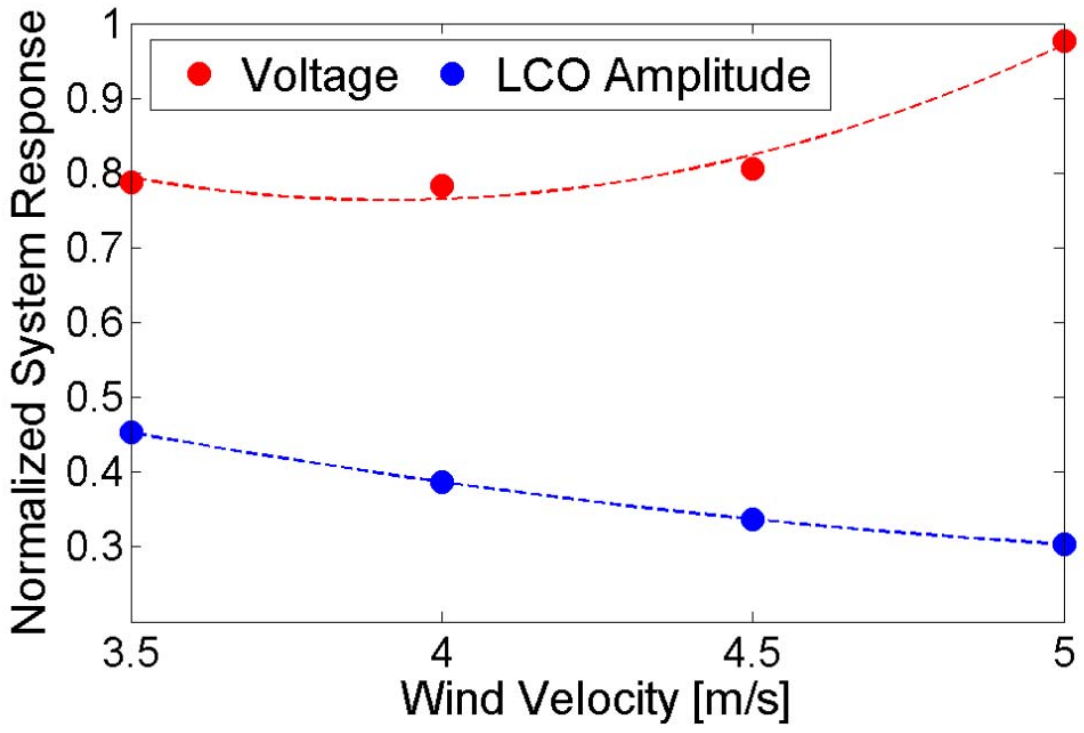

Figure 4.21: Normalized harvested voltage and LCO amplitude for the improved GPEH

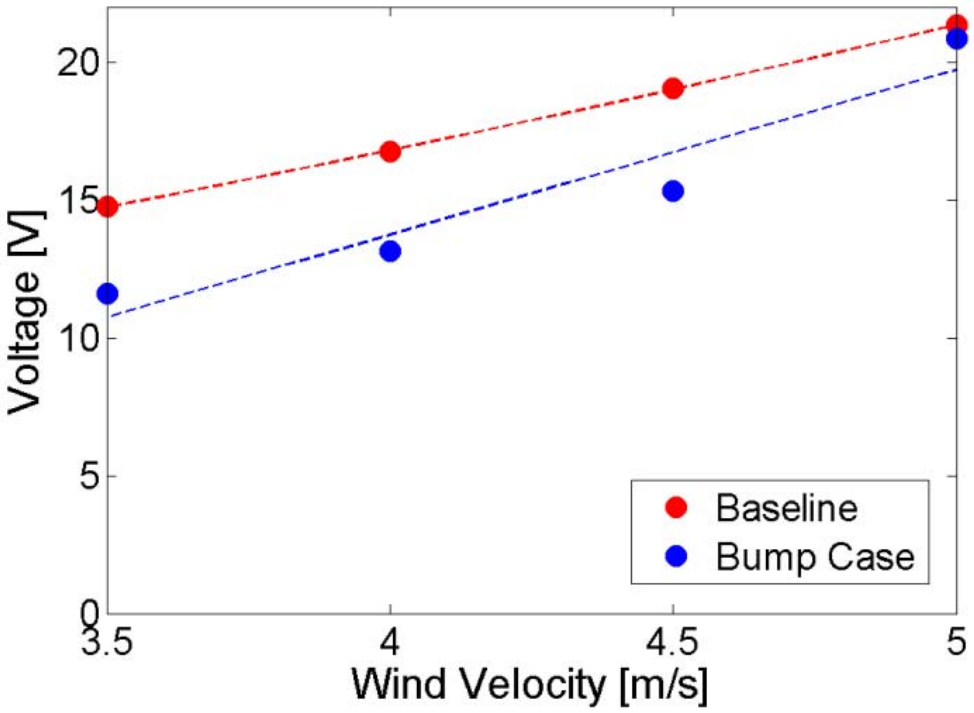

(a)

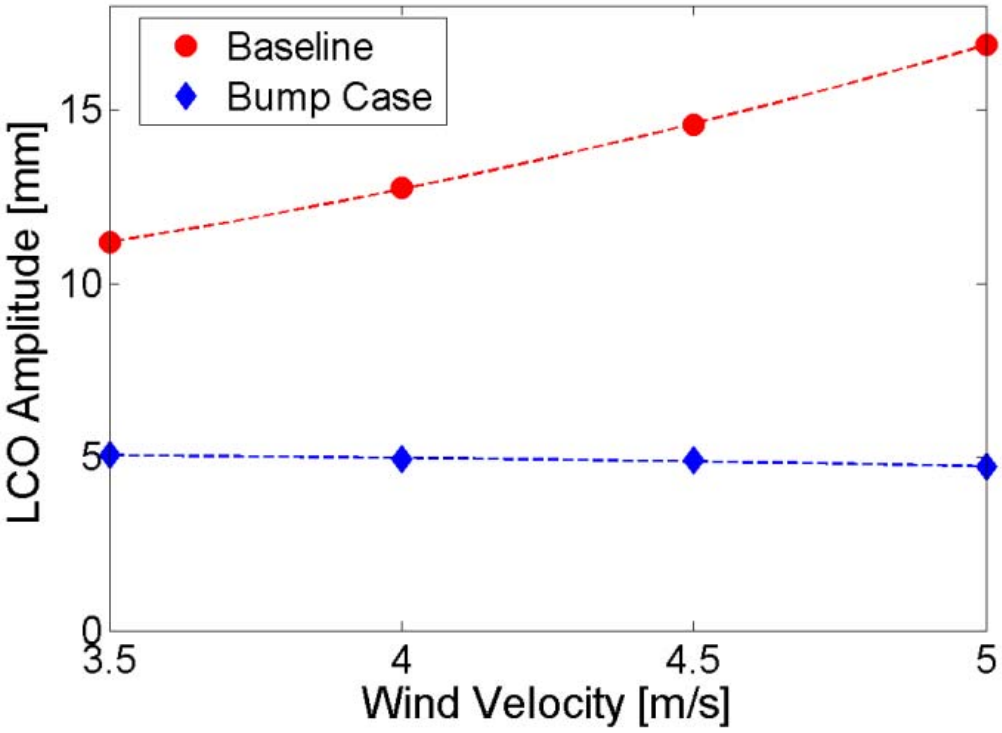

(b)

Figure 4.22: Performance comparison of baseline and improved GPEH; (L_{Gap}=5mm X_s=130mm, Contact area=(12.7x40)mm^2), R=100kΩ: (a) Voltage (b) LCO amplitude

4.5.1 Summary (Baseline GPEH with Bump Stop)

Comprehensive tests were conducted on the improved GPEH by varying three key parameters in the bump stop design. The optimal bump stop configuration was identified with substantial reduction in LCO amplitude and small tradeoff in harvested voltage. Key conclusions are summarized below.

- Fatigue damage in the baseline GPEH was observed and an improved GPEH was developed by introducing a bump stop

- Performance of the improved GPEH heavily depends on the three key bump stop design parameters, i.e., gap size, stop location, and contact surface area.

- Tests were conducted to investigate the effect of each design parameter on the harvested voltage and LCO amplitude.

- An optimal bump stop design was determined, i.e., L_{Gap} = 5 mm, Xs = 130 mm, contact surface area = (12.7 × 40) mm2

- Maximum 20% voltage reduction with substantial 70% reduction in LCO amplitude was observed for an optimal

- The baseline GPEH service life can be significantly improved by incorporating an impact bump stop. The improved GPEH design provides a practical solution to harvest electricity from wind-induced vibration.

4.6 Baseline GPEH with bio-inspired square bluff body

Figure 4.23 shows results for the variation of measured voltage and LCO amplitude with wind velocity for the different bluff bodies. Voltage and LCO amplitude increases with increasing wavelength λ/h. This implies drag and lift is reduced with decreasing wavelength. Notice an increase in the velocity for initiation of galloping with decreasing wavelength for $\lambda/h < 1$. The system begins to gallop around 3m/s which show the sinusoidal waviness alone can act as a form of passive control. The detachment of the start of galloping from system damping implies the system can be tuned to gallop by adjusting the waviness on the leading edge of the square cross-section bluff body.

There is progressive decrease in lift and drag as wave steepness increases as seen from Figure 4.24. The drag and lift reduction is due to redistribution of vorticity that leads to the breakdown of the unsteady and staggered Kármán vortex wake into a steady and symmetric near-wake structure [44]. Furthermore, at A/λ=0.25 the waviness is sufficient for the mean drag/lift levels to drop significantly and tend to zero for wind velocity of 2m/s – 3m/s.

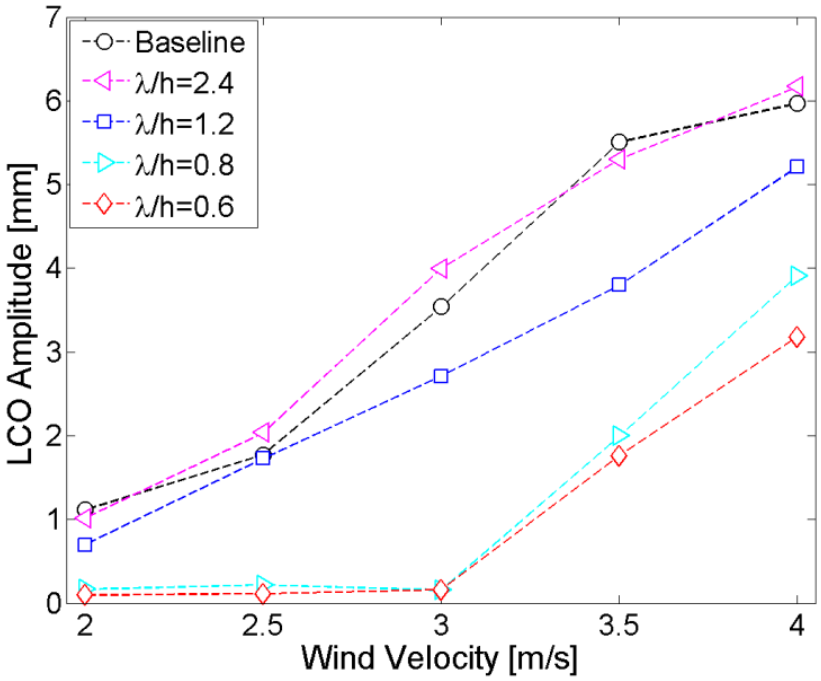

(a)

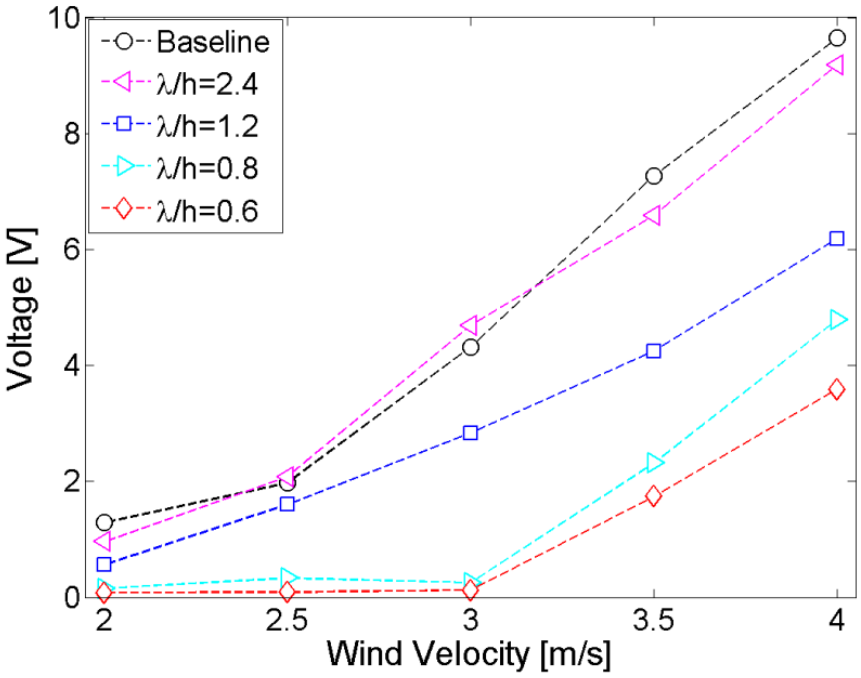

(b)

Figure 4.23: Measured data for bluff bodies variation with wind velocity (a) LCO amplitude (b) Peak voltage

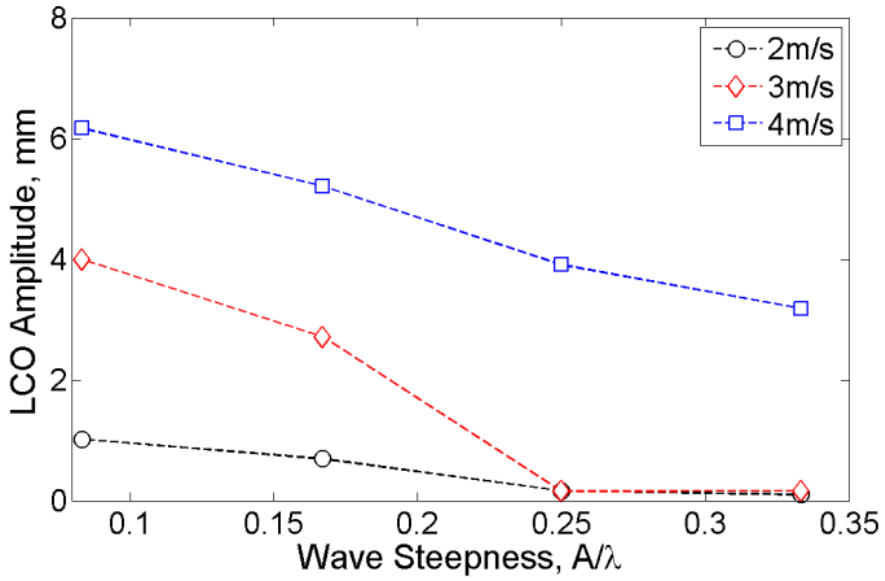

(a)

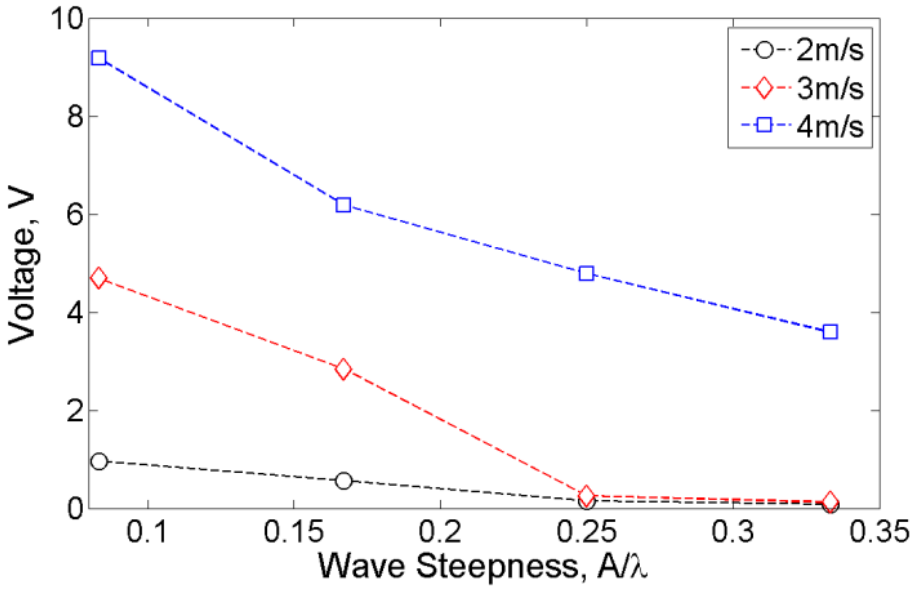

(b)

Figure 4.24: Measured data for bluff bodies variation with wave steepness (a) LCO amplitude (b) Peak voltage

Chapter 5: Numerical Model and Validation

Numerical studies were conducted using the COMSOL Multiphysics software in order to enhance the model prediction capability. Simulation were conducted to determine the vertical aerodynamic force coefficient for a square bluff body, impact stresses on a piezoelectric beam impacting a stop and voltage for the scaled (intermediate) GPEH. The COMSOL Multiphysics model captured the linear slope of the C_{FY} curve with reduced peak amplitude at 13°. Simulation results showed that (von Mises) stresses are lower for a piezoelectric beam impacting a bump stop compared to the baseline case without a stop. Furthermore, experimental data were used to validate the model predictions in terms of harvested voltage/power and LCO amplitude. The GPEH model with linear assumptions is able to capture the voltage response but fail to predict LCO amplitude. The improved GPEH model with nonlinear assumptions is able to capture both voltage and LCO amplitude responses and correlate well with experimental data.

5.1 COMSOL Multiphysics Numerical model

Numerical analysis is conducted using the finite element based simulation software; COMSOL Multiphysics. A verification analysis in 2D using the solid mechanics, MEMS and CFD module is carried out. First we determine the vertical

aerodynamic force coefficient using the CFD (Turbulent flow) module by sweeping from 0-20 degrees for a wind speed of 7m/s to agree with the Reynolds number (22700) of experiments conducted in [89,98]. Model details used to solve the Navier-Stokes equations are shown in Table 5.1 below;

Table 5.1: COMSOL Multiphysics Model Fluid Properties

Study Type	Stationary
Turbulence Model	Low Reynolds ($\kappa - \varepsilon$)
Turbulence Model Type	Reynolds Average Navier Stokes (RANS)
Turbulence Intensity	0.0005 (Low)
Turbulence Length Scale	0.005[m]
Length of Square Bluff Body	0.05[m]

To simulate baseline GPEH, the piezoelectric coupling with structure is achieved using the MEMS module (piezoelectric devices). A frequency domain study with the aerodynamic force modeled as a harmonic boundary load is conducted. The AC/DC (electric circuits) module allows for resistors to be connected to the circuit and voltage is acquired from a terminal and ground node.

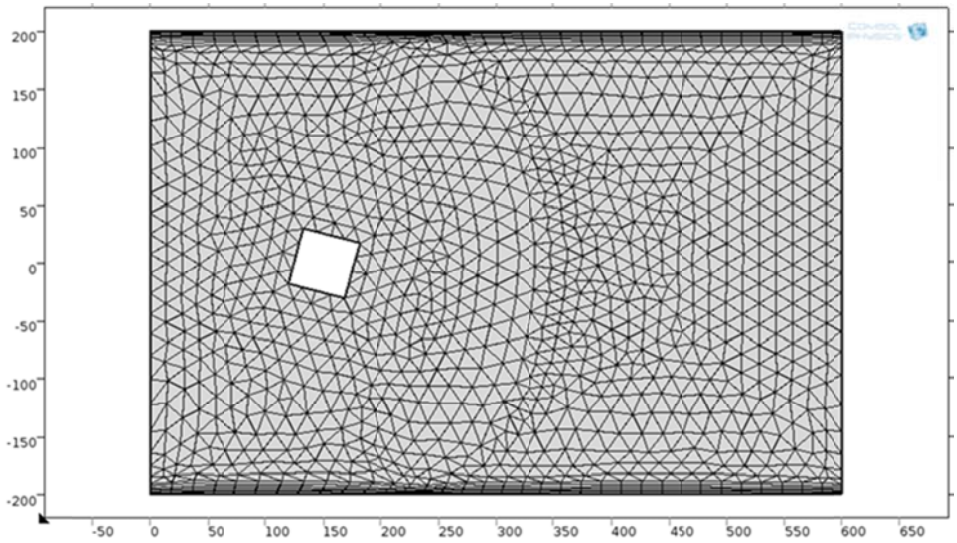

Figure 5.1: Mesh Model Snapshot

COMSOL Multiphysics expresses the piezoelectric constitutive equations in the stress-charge (2.10) or the strain-charge (2.11) only. The Properties of PZT-5A in the stress-charge form used for the simulations is given below;

Stiffness matrix

$$c_E = \begin{bmatrix} 12.03 & 7.52 & 7.51 & 0 & 0 & 0 \\ 7.52 & 12.03 & 7.51 & 0 & 0 & 0 \\ 7.51 & 7.51 & 11.08 & 0 & 0 & 0 \\ 0 & 0 & 0 & 2.11 & 0 & 0 \\ 0 & 0 & 0 & 0 & 2.11 & 0 \\ 0 & 0 & 0 & 0 & 0 & 2.26 \end{bmatrix} \times 10^{10} \frac{N}{m^2}$$

Piezoelectric constants

$$e = \begin{bmatrix} 0 & 0 & 0 & 0 & -5.35 & 0 \\ 0 & 0 & 0 & -5.35 & 0 & 0 \\ 12.30 & 12.30 & 15.78 & 0 & 0 & 0 \end{bmatrix} \frac{C}{m^2}$$

Relative permittivity

$$\varepsilon^S = \begin{bmatrix} 919.1 & 0 & 0 \\ 0 & 919.1 & 0 \\ 0 & 0 & 826.6 \end{bmatrix}$$

Parameters were for a scaled model (intermediate GPEH) shown in Figure 5.2.

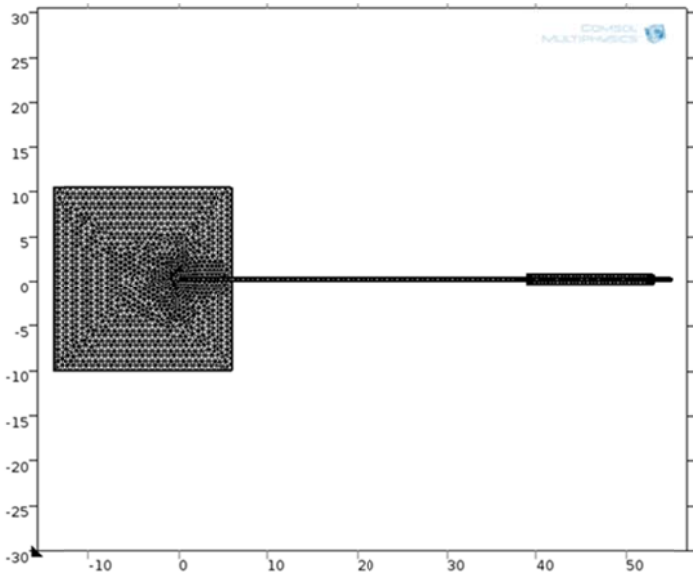

Figure 5.2: Meshed model of GPEH

Finally, a stationary study using the structural mechanics (solid mechanics) module is done on a GPEH with a bump stop to determine stresses on the baseline beam and GPEH with a bump stop.

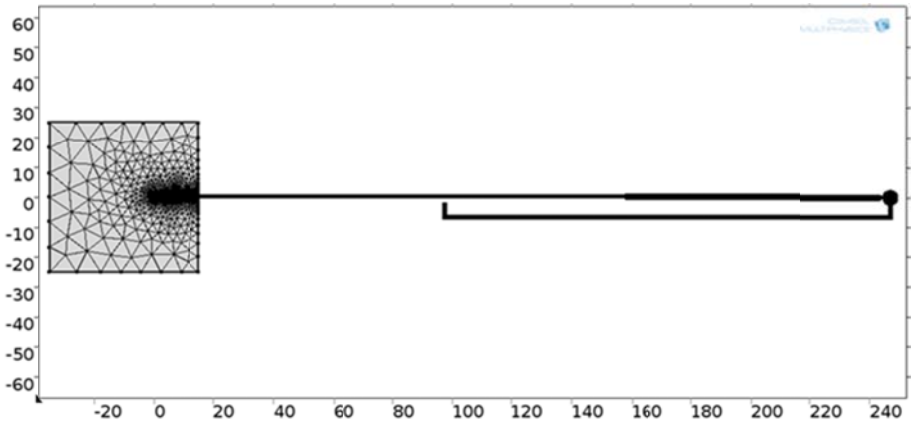

Figure 5.3: Baseline GPEH with bump stop model

A harmonic boundary load is applied to the tip mass and the gap size (L_{Gap}) is varied from 1mm to 2mm in steps of 0.2mm.

5.1.1 Quantifying aerodynamic force

The quasi-static model requires C_L and C_D at several angles of attack to determine the vertical coefficient C_{FY}. Surface plots of velocity for simulations conducted are presented in Figure 5.4 below for the case with turbulence intensity I_T=0.05%. Shear layer separation distance reduces with increasing angle of attack with attachment to the base noticed at about 16 degrees. Maximum velocity (outermost portion of shear layer) increases until 13 degrees and then reduces to 20 degrees.

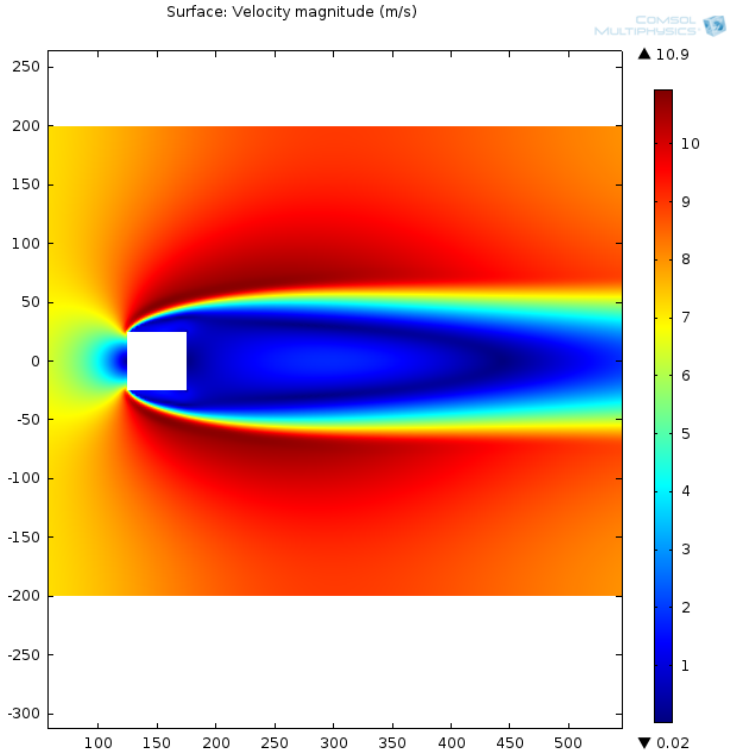
Surface: Velocity magnitude (m/s)
▲ 10.9
▼ 0.02
250
200
150
100
50
0
-50
-100
-150
-200
-250
-300
100 150 200 250 300 350 400 450 500
10
9
8
7
6
5
4
3
2
1

(a)

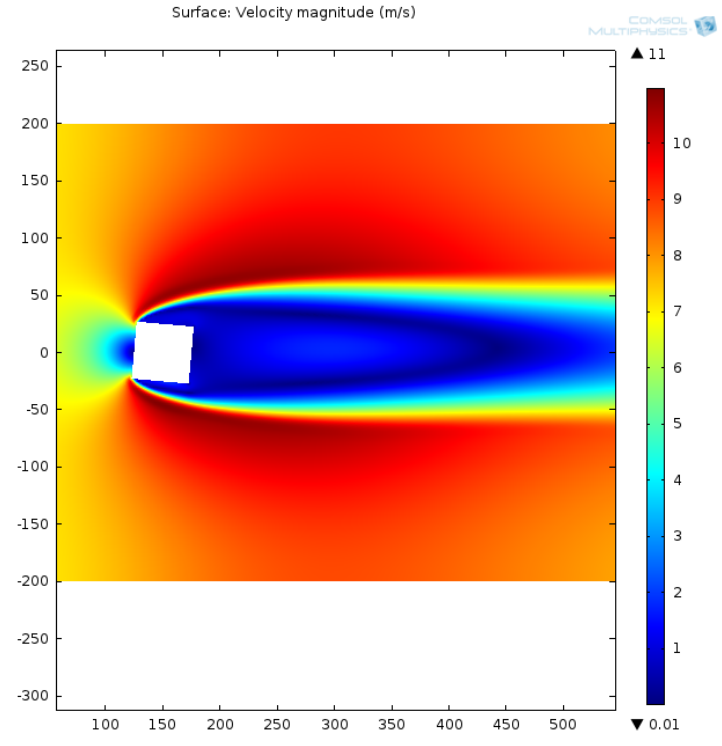
Surface: Velocity magnitude (m/s)
▲ 11
▼ 0.01
250
200
150
100
50
0
-50
-100
-150
-200
-250
-300
100 150 200 250 300 350 400 450 500
10
9
8
7
6
5
4
3
2
1

(b)

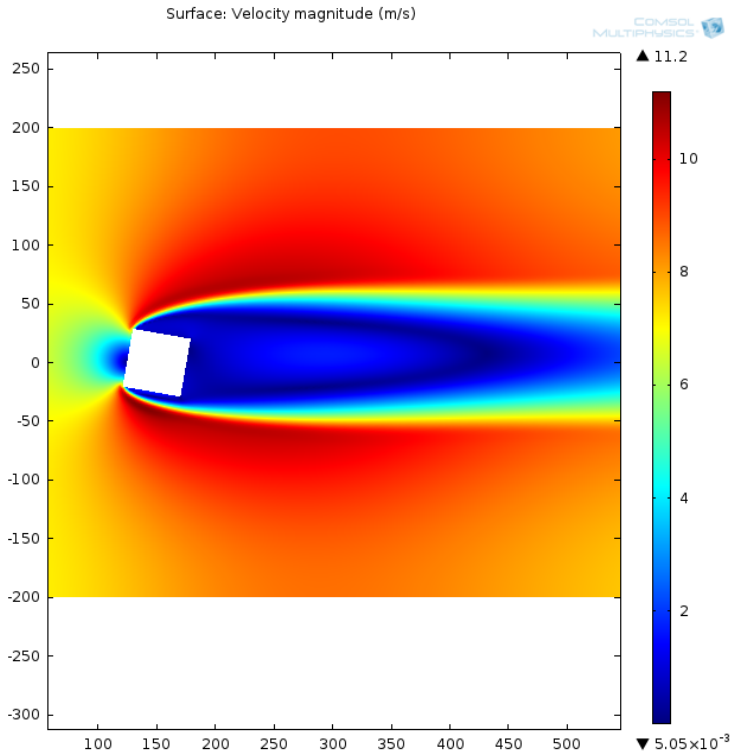
Surface: Velocity magnitude (m/s)
COMSOL MULTIPHYSICS
▲ 11.2
10
8
6
4
2
▼ 5.05×10^-3
250
200
150
100
50
0
-50
-100
-150
-200
-250
-300
100
150
200
250
300
350
400
450
500

(c)

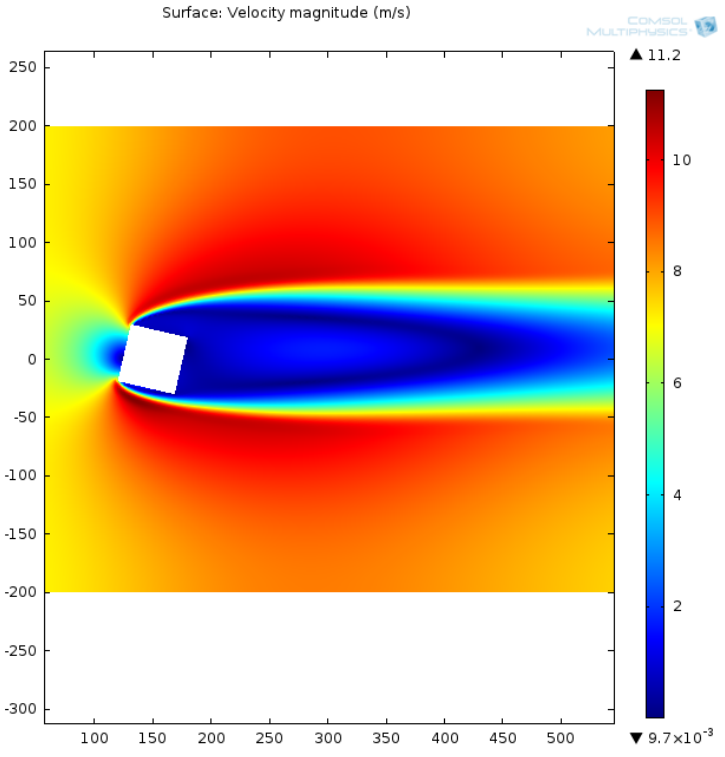
Surface: Velocity magnitude (m/s)
COMSOL MULTIPHYSICS
▲ 11.2
10
8
6
4
2
▼ 9.7×10^-3
250
200
150
100
50
0
-50
-100
-150
-200
-250
-300
100
150
200
250
300
350
400
450
500

(d)

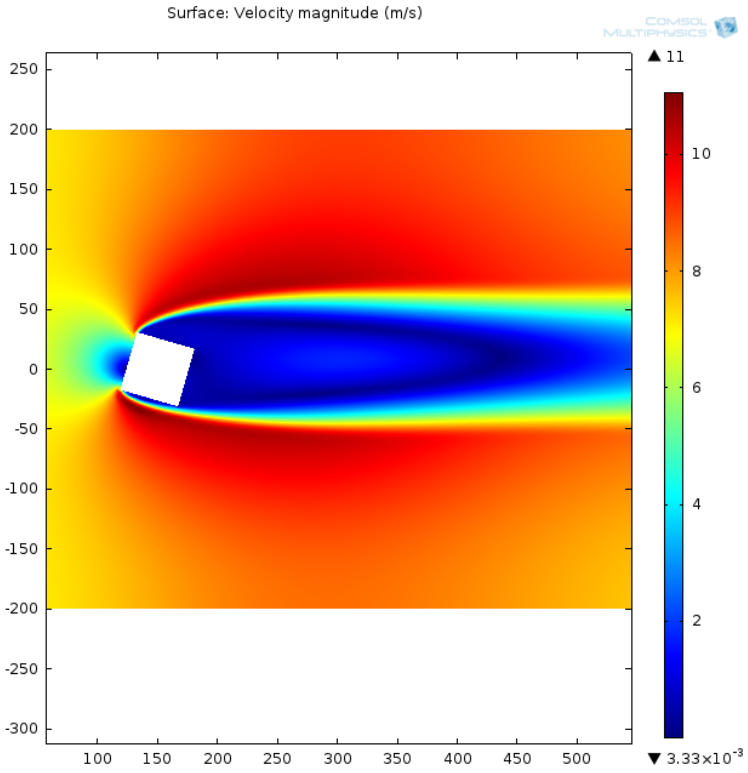

(e)

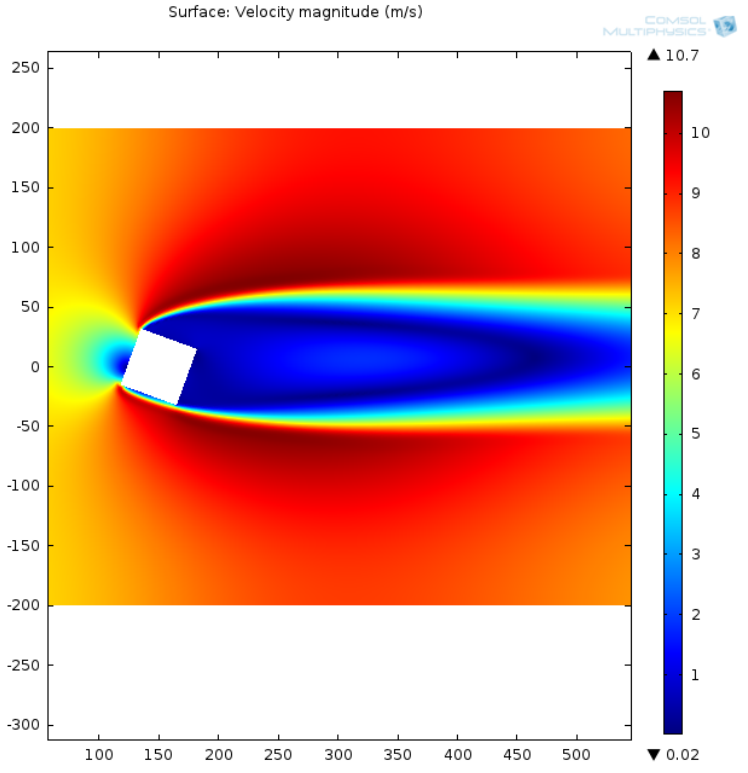

(f)

Figure 5.4: Surface plot-velocity (COMSOL Multiphysics), $I_T = 0.005$; a=0 deg. b=5 deg. c=10 deg. d=13 deg. e=16 deg. f=20 deg.

Plots for lift and drag are shown in Figure 5.5 which is consistent with experiments performed by Wawzonek [98]. The hysteresis behavior expected with low turbulence for a square cross-section bluff body is not well captured by the model as seen in the comparison curve for C_{FY} in Figure 5.6. The COMSOL Multiphysics model captures only the initial inflexion point and linear slope A_1 i.e. between 0-5 degrees but has reduced amplitude at the peak (13 deg.). This discrepancy could be due to the 2D instead of 3D model. Table 5.2 compares the coefficients of the polynomial fit for the COMSOL Multiphysics model and experiments performed by Parkinson and Smith [7,89]. The effect of turbulence intensity on C_{FY} curve is shown in Figure 5.7 which is consistent with experiments performed by Laneville [99]. The peak of the C_{FY} curve shifts to the left and reduces in amplitude with increasing I_T. Furthermore C_{FY} loses one of its inflexion points with no significant change in the initial slope A_1. This implies that the square section will become unstable at the same initiation velocity in more turbulent flow but will gallop with reduced amplitude.

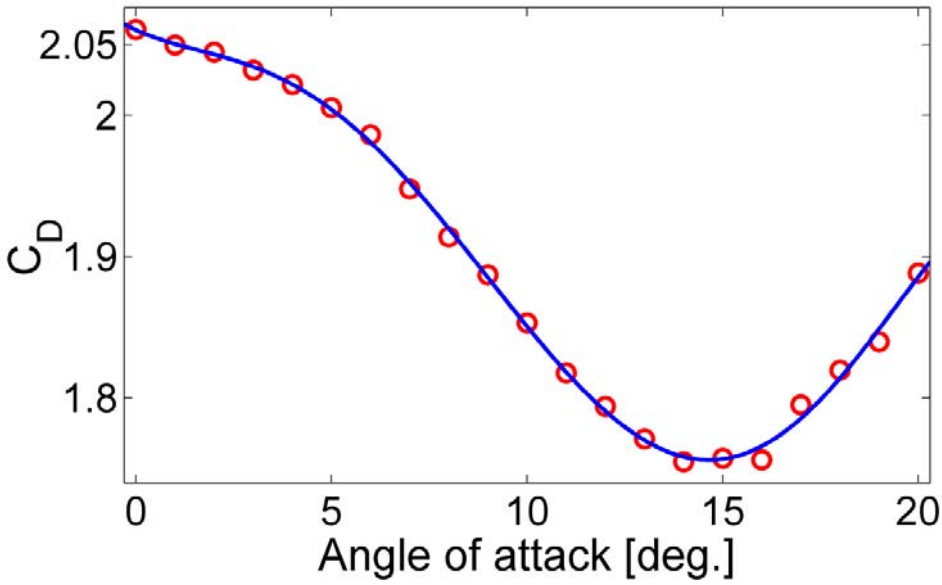

(a)

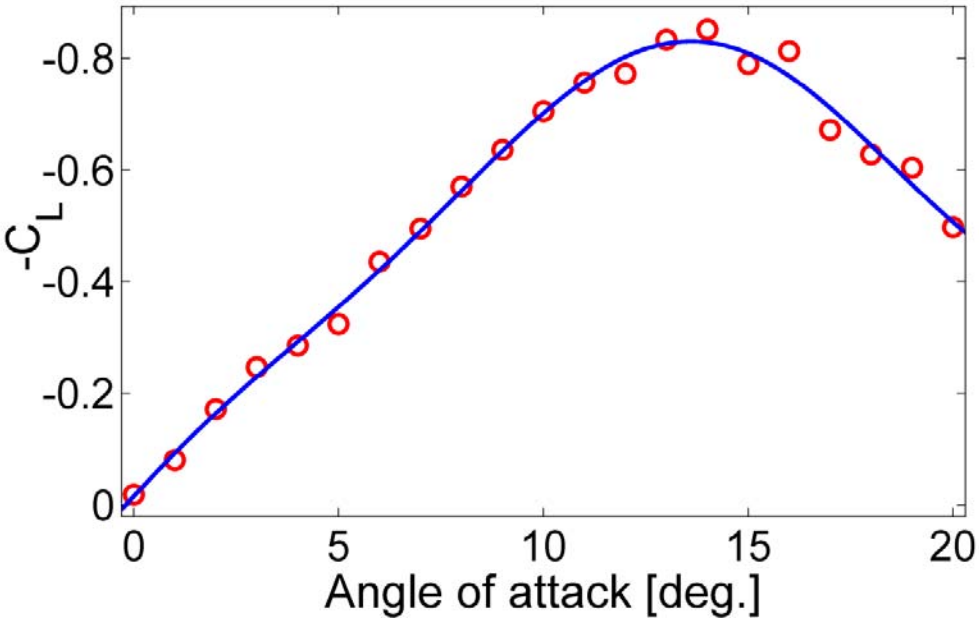

(b)

Figure 5.5: COMSOL Multiphysics Model results and 7th order polyfit for low I_T Re=22700 (a) Drag (b) Lift

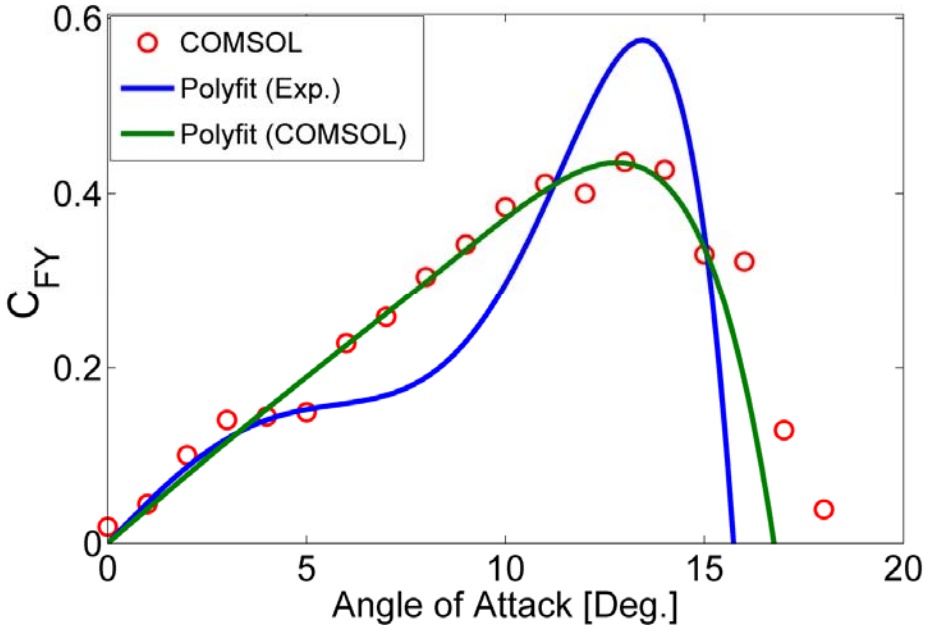

Figure 5.6: Vertical aerodynamic force (C_{FY}) COMSOL Multiphysics Model results for low I_T (0.05%) Re=22700

Table 5.2: Coefficients of C_{FY} Polynomial

7th order Polyfit	A_1	A_3	A_5	A_7
Experiment	2.69	-168	6270	-59900
COMSOL Multiphysics (2D Model)	2.244	-13.37	569.9	-8436

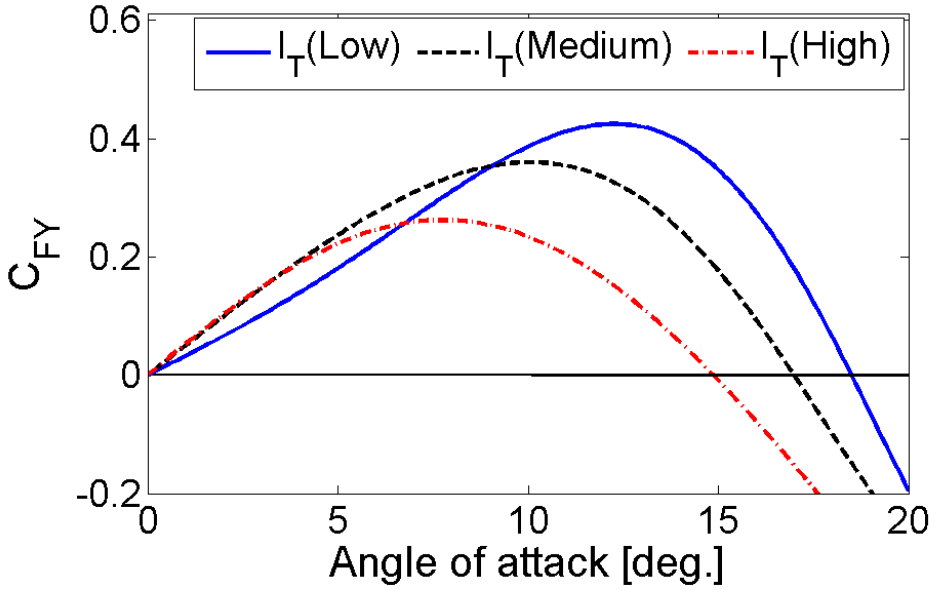

Figure 5.7: Effect of turbulence intensity (0.05%, 0.7%, 1.4%)

5.1.2 Impact stress analysis (under harmonic tip excitation)

Simulation done for the GPEH with bump stop was to show the trend of von Mises stress in the substrate and tip displacement (Figure 5.9) to illustrate the effect of the stresses generated when the beam impacts a bump stop.

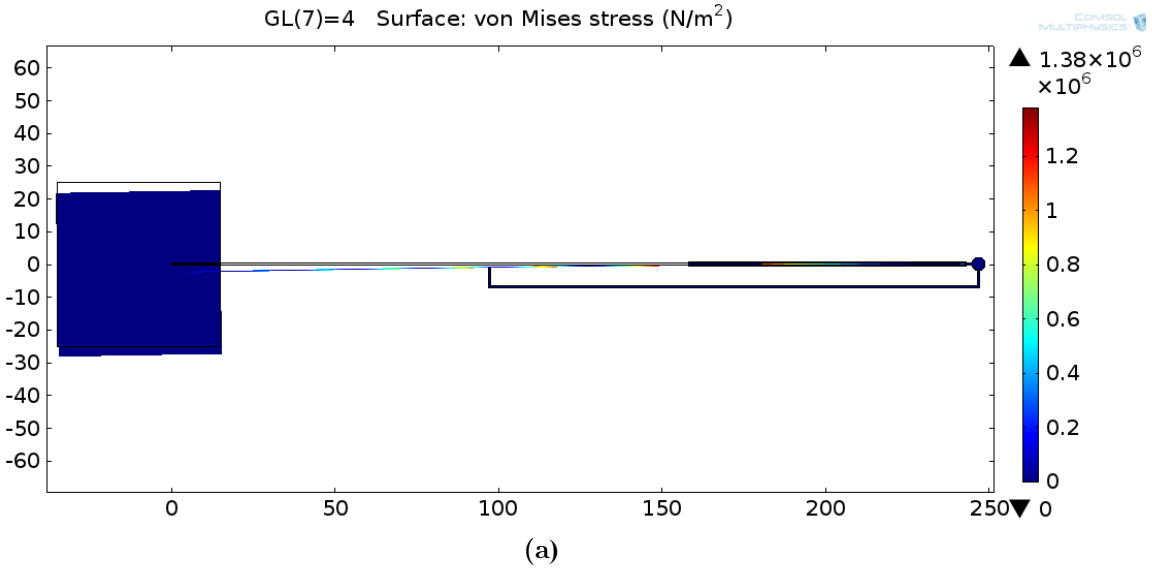

(a)

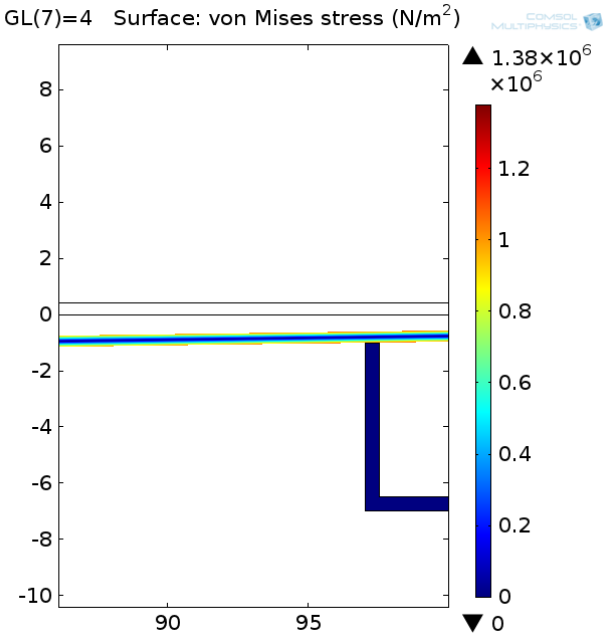

(b)

Figure 5.8: Surface plot – von Mises stress; L_{Gap}=1mm: (a) GPEH (b) Zoomed stop area

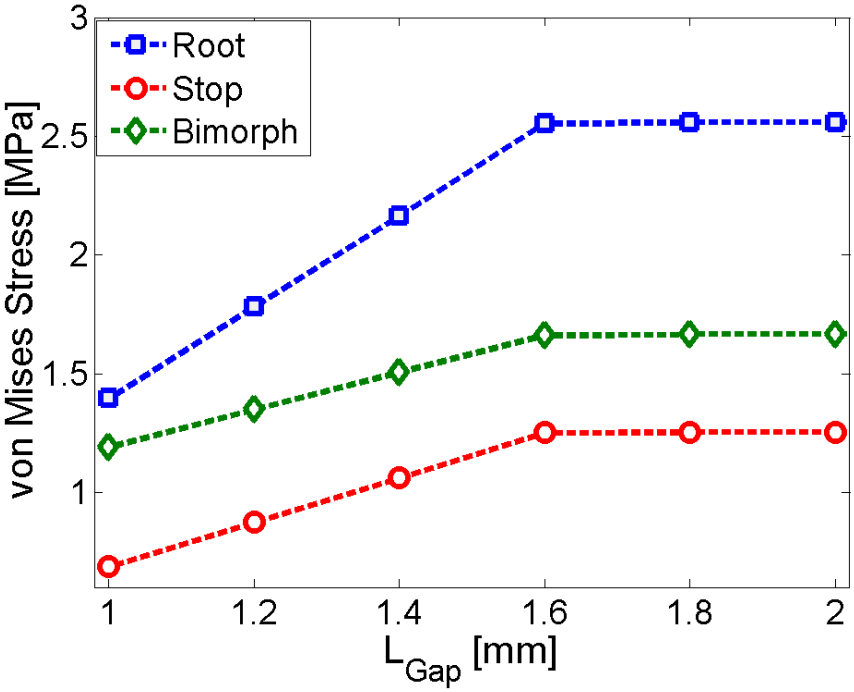

(a)

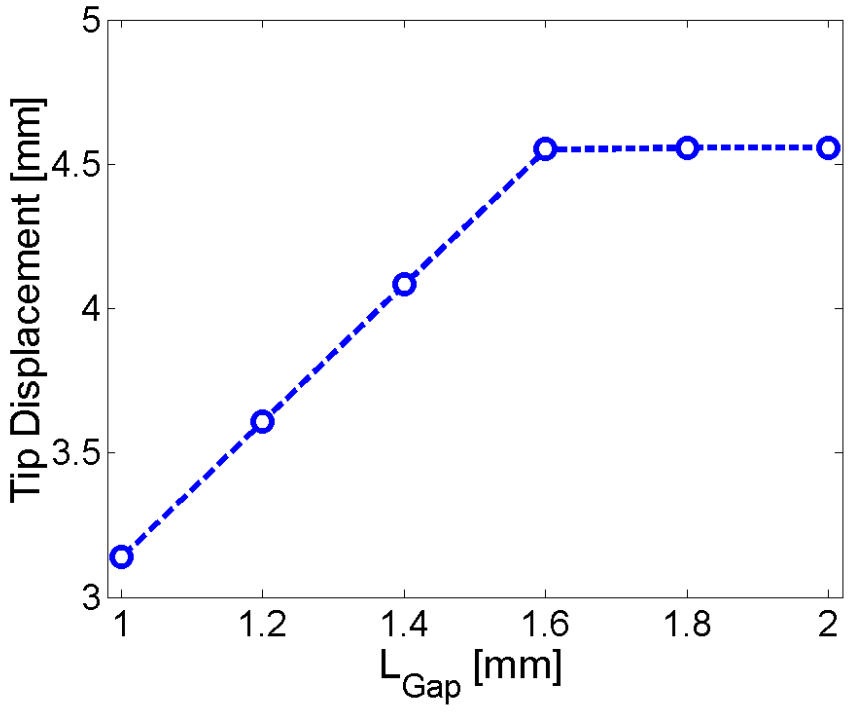

(b)

Figure 5.9: Impact Analysis: (a) von Mises (b) Tip displacement

Tip harmonic force is applied at the first mode to the tip mass. Figure 5.8 shows surface plot of von Mises stresses zoomed in to show the stop impeding beam's movement. Tip displacement and von Mises stresses increases monotonically with increasing gap size until baseline case i.e. when gap length exceeds the beam's path for the tip load considered. As expected the stresses are highest at the root, followed by the bimorph piezoelectric area and lowest at the stop area. Predictably stresses on the GPEH with a bump stop are lower than that without the stop.

5.2 Validation

5.2.1 Performance Validation (Baseline)

Model predictions are validated by experimental data, in which the electrical load is 100kΩ and wind velocity is 4m/s. Voltage and power predictions match well with experimental data as shown in Figure 5.10. However, the hysteresis jump was not noticed which is expected for a square tip bluff body [89,92]. Figure 5.11 shows the LCO amplitude predictions. Clearly, the linear model (Figure 5.11a) captures the trend but over-predicts the LCO amplitude. Recall the length of the GPEH is 228mm. The beam motion is within the linear elastic range. Piezoelectric material nonlinearity, i.e., softening effect, should also play a role in the displacement predictions as discussed by Stanton *et al.* [96]. Therefore, we must include

piezoelectric material nonlinearity and nonlinear damping model in order to improve our structural prediction which is encompassed in the nonlinear model. The nonlinear model (Figure 5.11b) is in good agreement with measured values; it captures the trend and matches the amplitude.

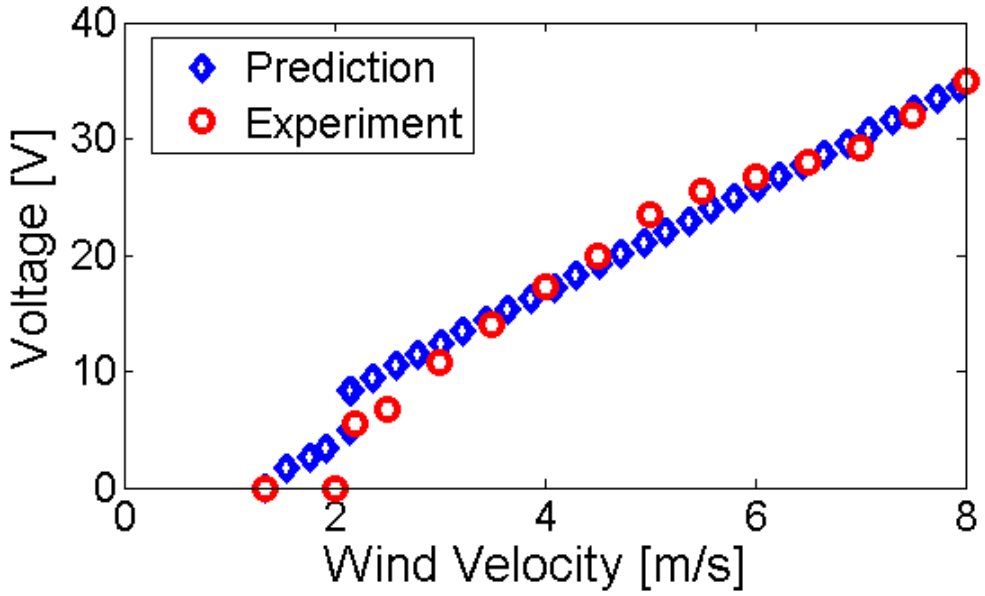

(a)

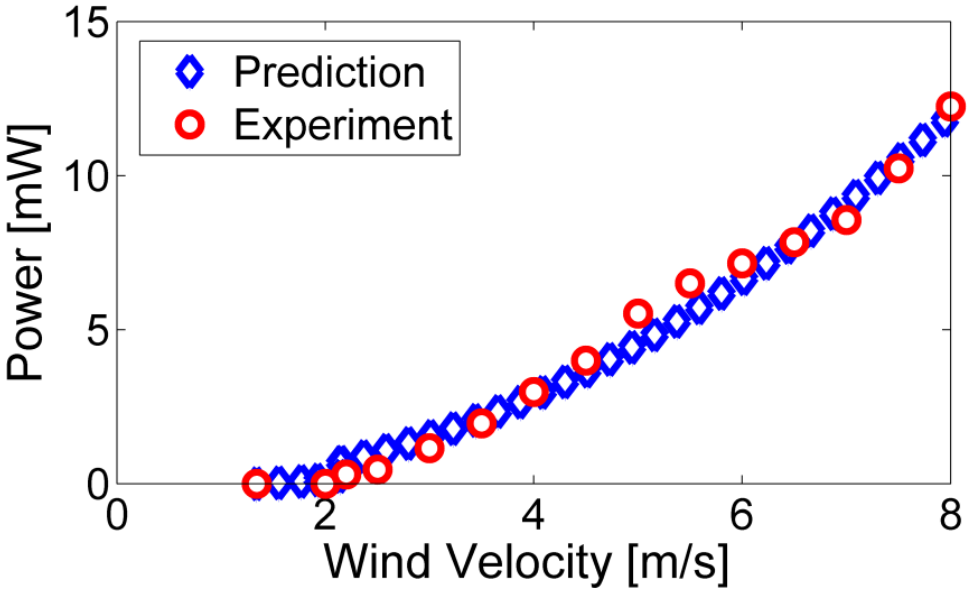

(b)

Figure 5.10: Performance predictions for baseline GPEH; R=100kΩ , V=4m/s: (a) Voltage (b) Power

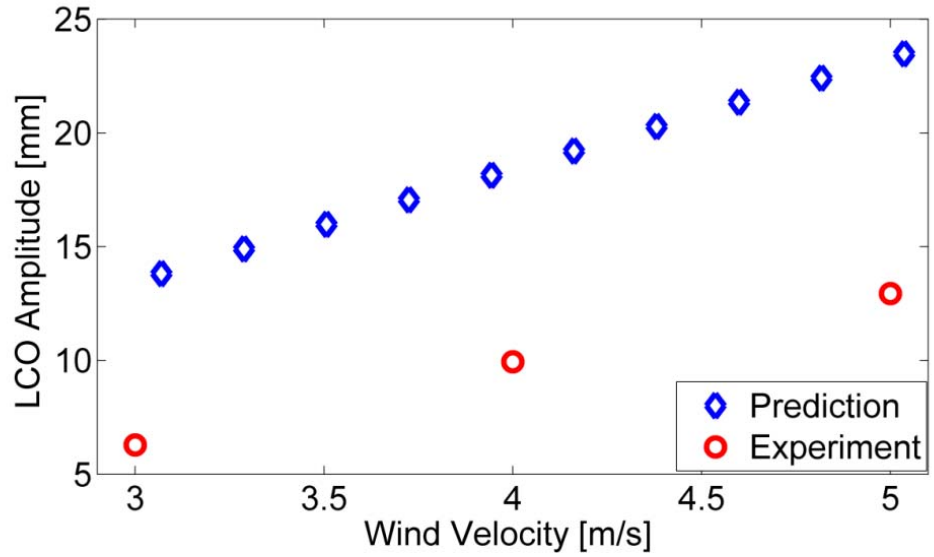

(a)

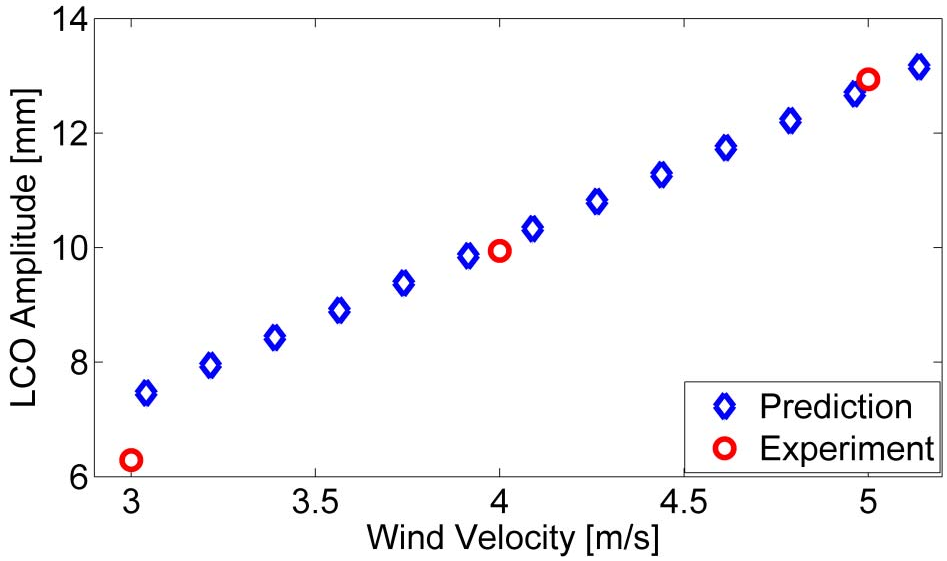

(b)

Figure 5.11: LCO amplitude prediction for baseline GPEH; R=100kΩ, GPEH Model with: (a) Linear assumptions (b) Nonlinear assumptions

5.2.2 Validation (Numerical Model)

Measured data for the intermediate GPEH (presented in 6.2.1) is used to validate COMSOL Multiphysics simulation results. Voltage and power results from

the COMSOL Multiphysics model with intermediate GPEH properties are presented in Figure 5.13. Measured data and simulation results are in good agreement while surface plot of voltage is shown in Figure 5.12.

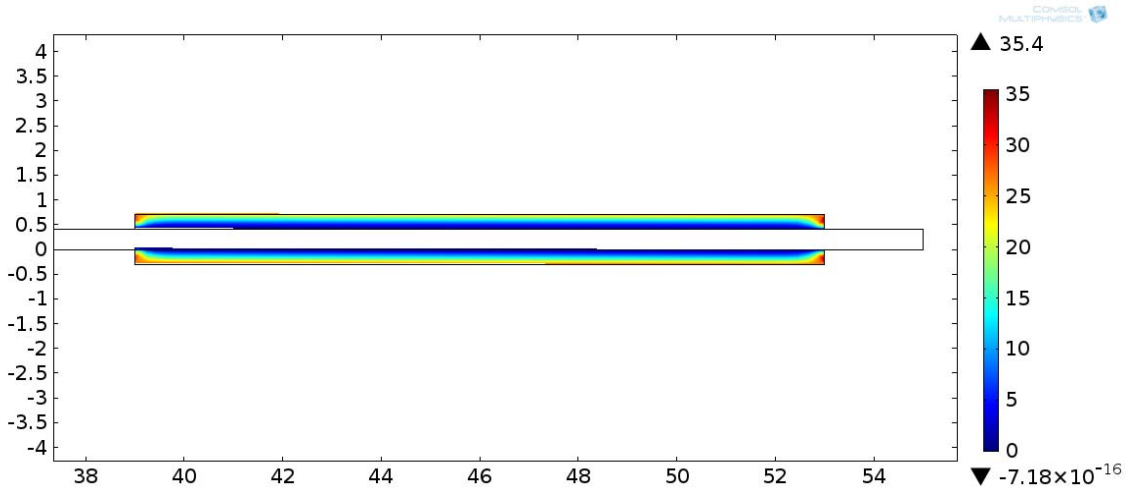

Figure 5.12: Surface plot (voltage) of model with intermediate GPEH properties; R=1MΩ, V=10.5m/s

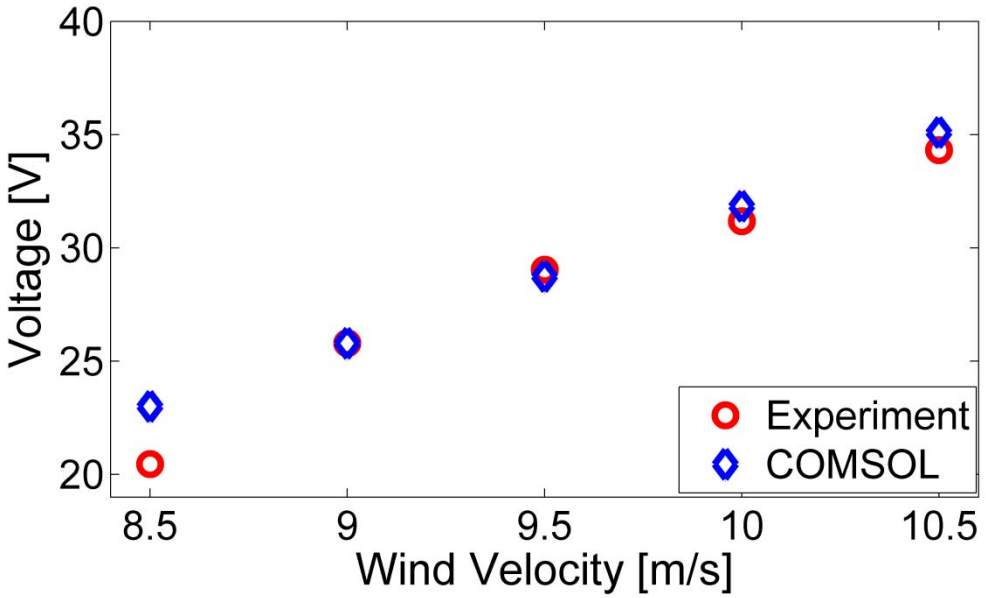

(a)

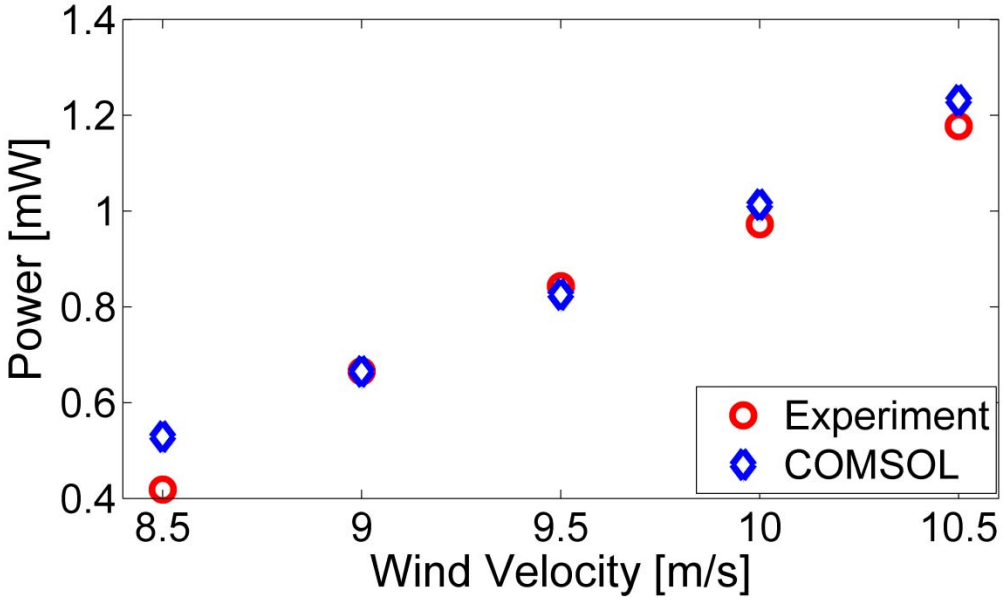

(b)

Figure 5.13: Prediction by COMSOL Multiphysics for Intermediate GPEH, R=1MΩ; (a) Voltage (b) Power

Chapter 6: Applications

Practical applications of the GPEH concept are discussed in this chapter. Two sub-scale GPEH prototypes (denoted by intermediate GPEH and mini GPEH) were fabricated. Wind tunnel tests were conducted to evaluate the system performance for energy harvesting and flow sensing applications. Measured data for the intermediate GPEH were used to validate model predictions and results were compared to baseline GPEH. Furthermore, the intermediate GPEH prototypes with different bio-inspired bluff bodies were tested to demonstrate passive control of the onset of galloping by simply varying the waviness in the bio-inspired bluff body. Finally, a fixture was designed and built to host a rosette of three identical mini GPEHs in order to demonstrate the airflow sensing application.

6.1 Sub-scale GPEH

The phenomenological behavior of the baseline GPEH is scaled with considerations to both size and materials. The benefits of a dimensionless formulation are observed - ease of scaling and performance comparison. The volume of the tip bluff body was scaled to $1/15^{\text{th}}$ and $1/30^{\text{th}}$ of the baseline to give an intermediate GPEH (Figure 6.1) with η=0.03 and a mini GPEH (Figure 6.2) with η=0.01. Other key properties scaled accordingly are given in Table 6.1 and

Figure 6.3 shows all GPEH generations. Details of dimensions and material properties of these prototypes are shown in Table 6.2 and 6.3. The mini GPEH is a unimorph configuration composed of a piezoelectric fiber (diameter = 800µm) glued to an aluminum beam. To ensure a consistent electrical contact during operation the fiber is sandwiched in a coat of polyester.

Table 6.1: Scaling factors for GPEH reduced prototypes

Parameter	**Intermediate GPEH**	**Mini GPEH**
Bluff body mass	1/4	1/16
Bluff body square area	1/6.25	1/6.25
Height of bluff body	1/2.4	1/4.8
Piezoelectric material surface area	1/24	1/(2x95)
Width of substrate	1/2	1/10
Length of substrate	1/4.6	1/5.75

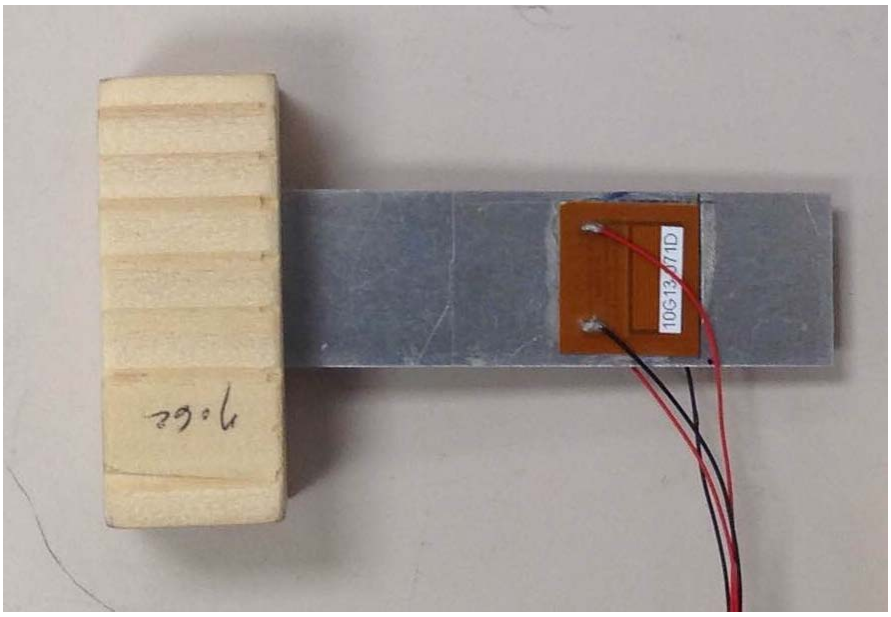

Figure 6.1: Intermediate GPEH

Table 6.2: Intermediate GPEH dimensions and material properties

Aluminum Beam	
Length from clamp (L_b) mm	50
Length MFC from clamp (L_m) mm	2
Width (b) mm	20
Thickness (h_b) mm	0.4
Young's Modulus (E) GPa	70
Density (ρ_b) kg/m^3	2700
MFC (M8528-P2)	
Active Length (L_p) mm	7
Active Width (b_p) mm	14
Thickness (h_p) mm	0.3
Overall Length (mm)	16
Overall Width (mm)	16
Piezoelectric coupling term (Θ) v/m	-2421.03
Capacitance (nF)	15.78
Area Density (g/cm^{-2})	0.16
Tip Bluff Body (Pine Wood)	
Density (g/cm^{-3})	0.39
Length (l) (mm)	50
Width (h) (mm)	20

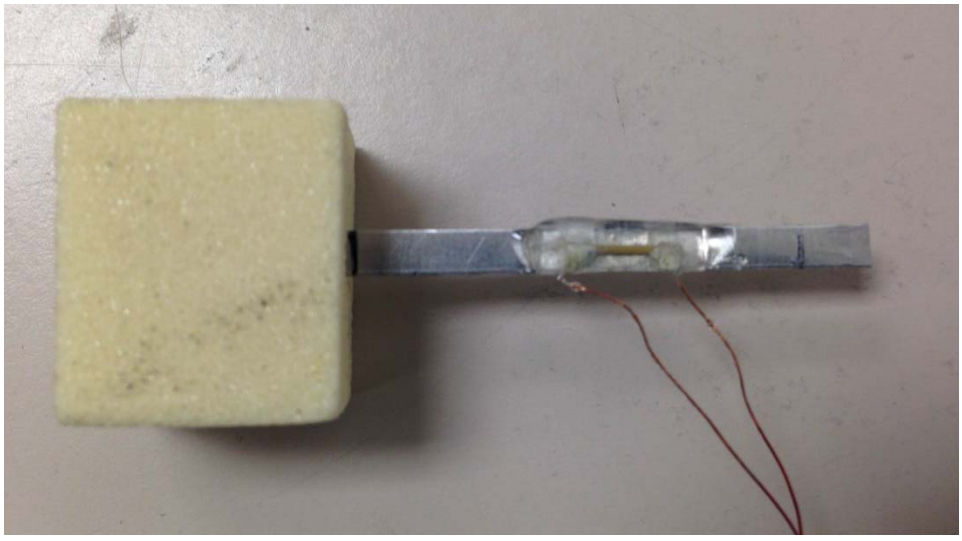

Figure 6.2: Mini GPEH

Table 6.3: Mini GPEH dimensions and material properties

Aluminum Beam	
Length from clamp (Lb) mm	40
Length MFC from clamp (Lm) mm	2
Width (b) mm	4
Thickness (hb) mm	0.4
Young's Modulus (E) GPa	70
Density (ρ_b) kg/m^3	2700
PZT Fiber	
Length (Lp) mm	10
Diameter (bp) mm	0.8
Piezoelectric coupling term (Θ) v/m	-2421.03
Capacitance (pF)	0.0213
Area Density (g/cm^{-2})	0.16
Tip Bluff Body (Polyurathane Foam)	
Density (g/cm^{-3})	0.095
Length (l) (mm)	25
Width (h) (mm)	20

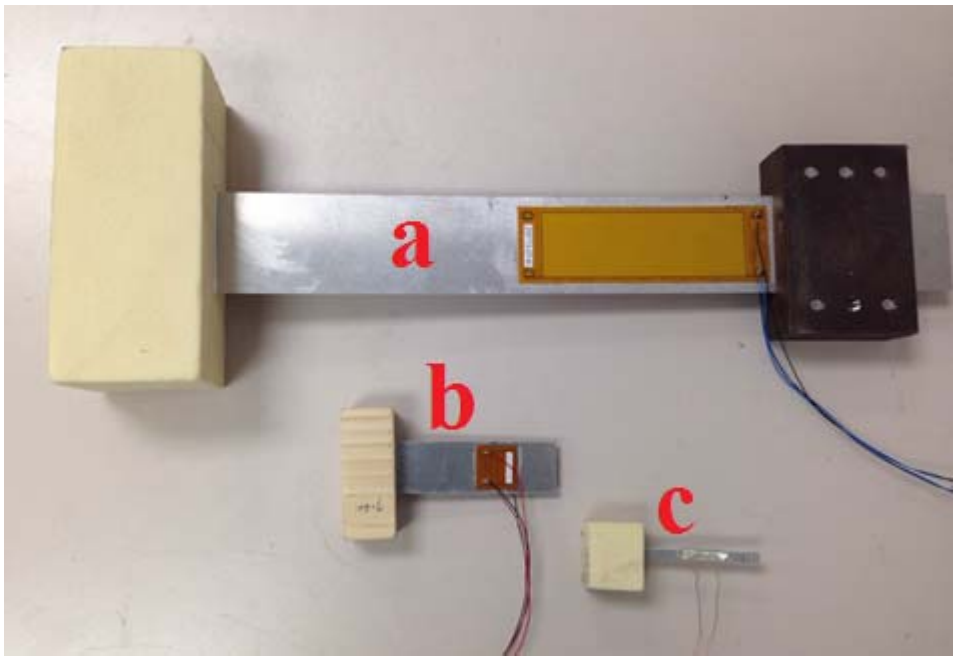

Figure 6.3: GPEH Generations; (a) Baseline (b) Intermediate (c) Mini

6.2 Energy harvesting

6.2.1 Intermediate GPEH

The energy harvesting potential of the scaled prototypes is presented using measured data from wind tunnel tests. The prototypes are characterized to specify optimum operating conditions and harvested energy. Similar to baseline GPEH the trend of LCO amplitude, harvested voltage and power for the intermediate GPEH is given in Figure 6.4. The optimum load resistance is determined from (5.1) to be 552kΩ and GPEH was tested for (120kΩ, 500kΩ, 1MΩ, 5MΩ and open circuit) loads from 8.5 - 10.5m/s wind velocity. Maximum voltage is 40V at open circuit loads and 10m/s wind velocity and 7m/s is the velocity for initiation of galloping. Maximum power of 1.75mW is accrued for 500kΩ loads at 10.5m/s. The intermediate GPEH was used to power an LED bulb at 10m/s and 330kΩ loads connected across. Therefore an array of this self-sufficient prototype can be used to provide constant power for cameras or network sensors at the beach or desert at minimal cost. Also, model predictions for the intermediate GPEH is validated using measured data as shown in Figure 6.6.

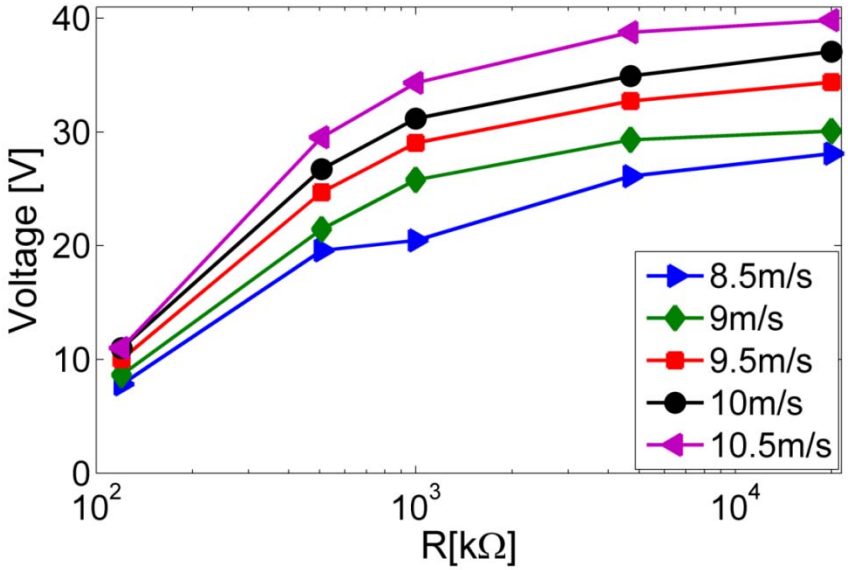

(a)

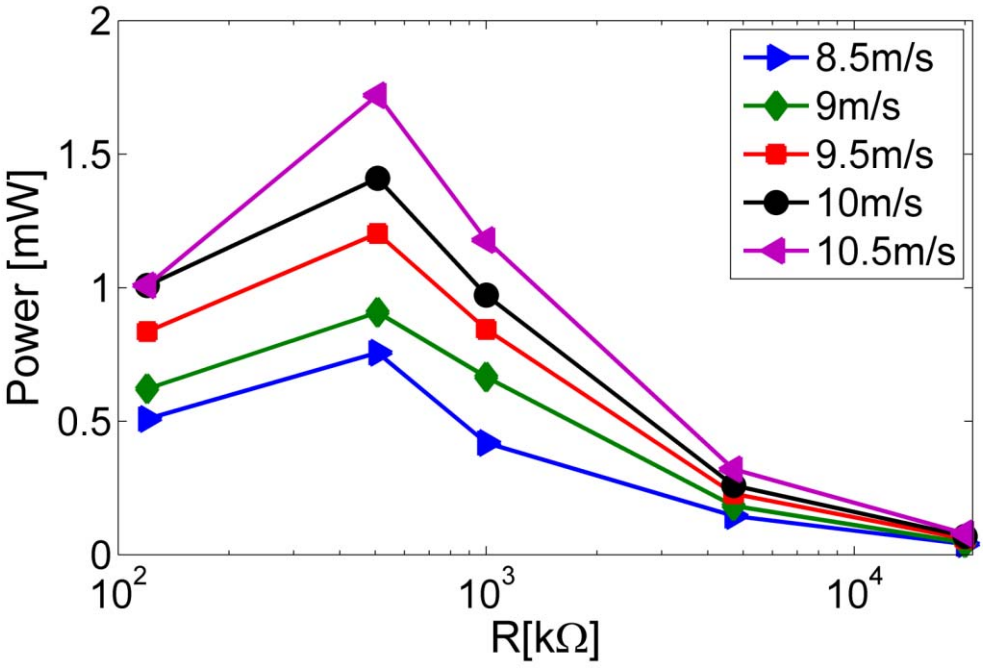

(b)

Figure 6.4: Measured data for intermediate GPEH (a) Voltage (b) Power

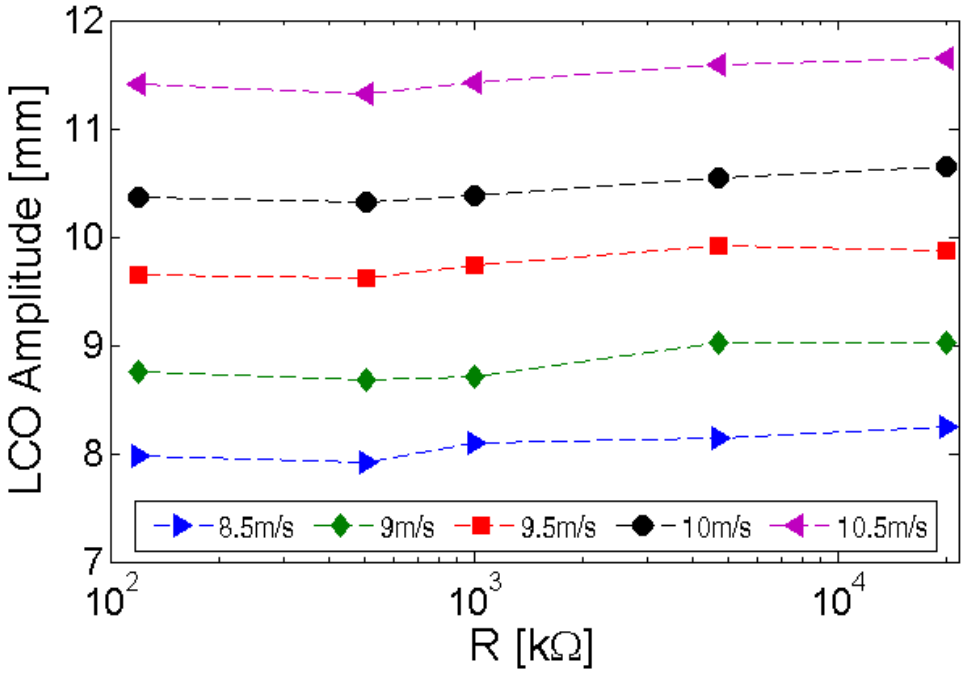

(a)

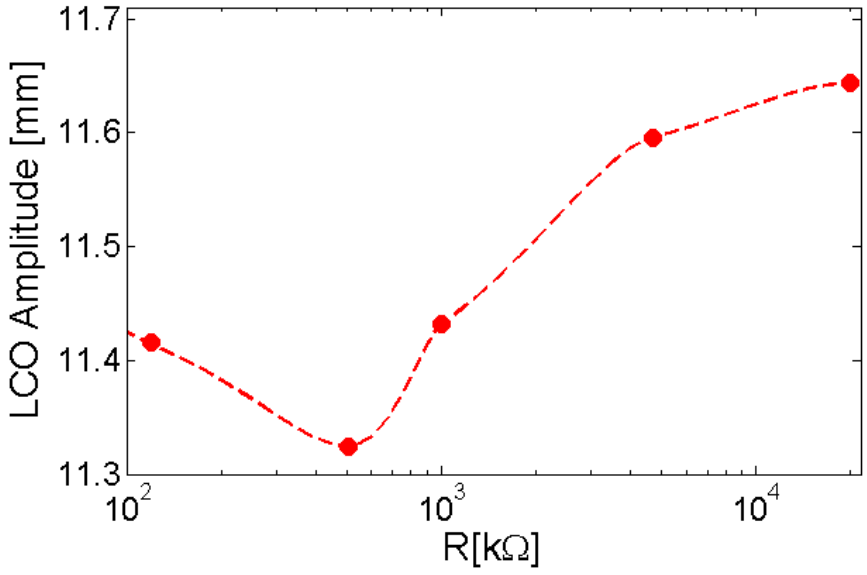

(b)

Figure 6.5: LCO amplitude vs resistance for intermediate GPEH (a) 8.5m/s – 10.5m/s (b) 10.5m/s

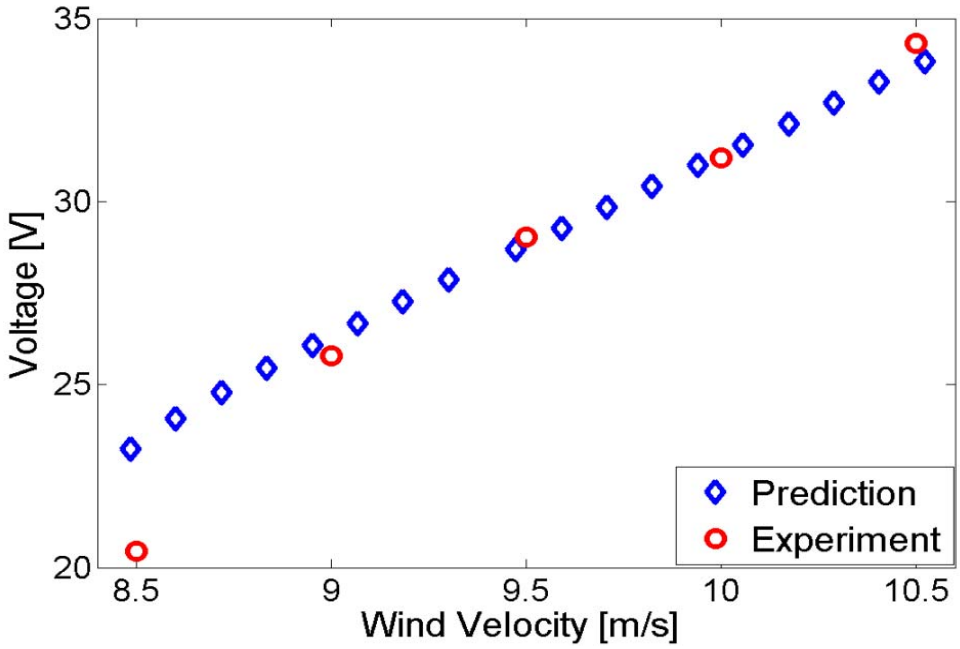
35
30
25
20
Voltage [V]
8.5
9
9.5
10
10.5
Wind Velocity [m/s]
Prediction
Experiment

(a)

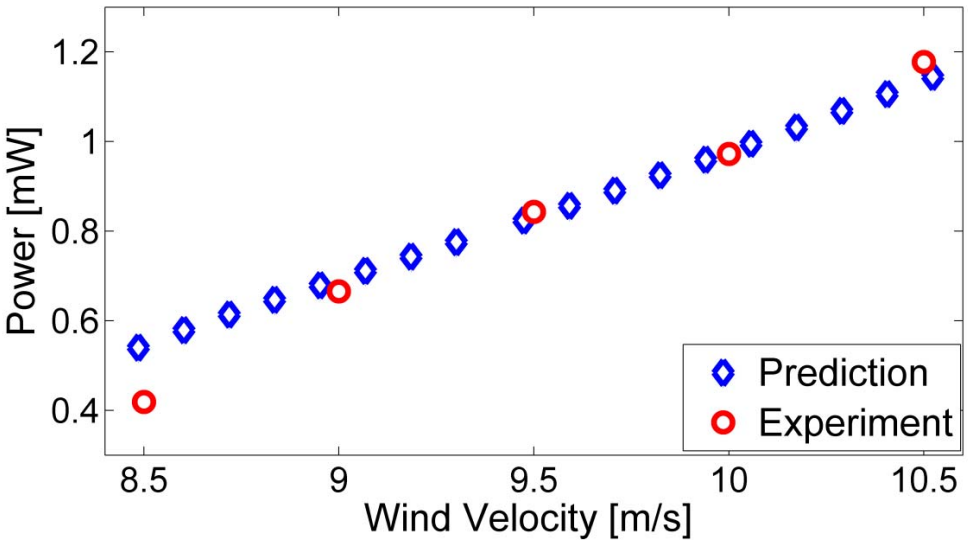
1.2
1
0.8
0.6
0.4
Power [mW]
8.5
9
9.5
10
10.5
Wind Velocity [m/s]
Prediction
Experiment

(b)

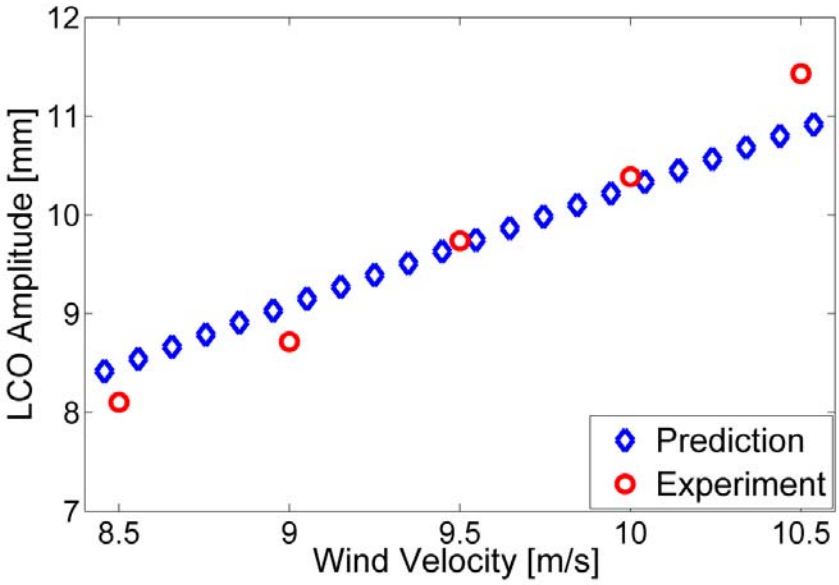

(c)

Figure 6.6:Intermediate GPEH validation (a) Voltage (b) Power (c) LCO Amplitude

Table 6.4: GPEH generations comparison

Property	Baseline	Intermediate	Mini
Initiation Velocity	$<$ 2m/s	8.5m/s	4 m/s
Max Voltage (V)	50 @ 8m/s	40 @ 10.5m/s	7 @ 6m/s
Max Power (mW)	13 @ 8m/s	1.75 @ 10.5m/s	N/A
Power Density* (mW/cm^3)	2.3 @ 8m/s	3.8 @ 10.5m/s	N/A

*Volume of piezoelectric sheet

6.2.2 Mini GPEH

Two kinds of mini GPEHs were tested with bluff body height l=25mm and 50mm. LCO amplitude harvested voltage for the mini GPEH is given in Figure 6.9 for l=50mm.

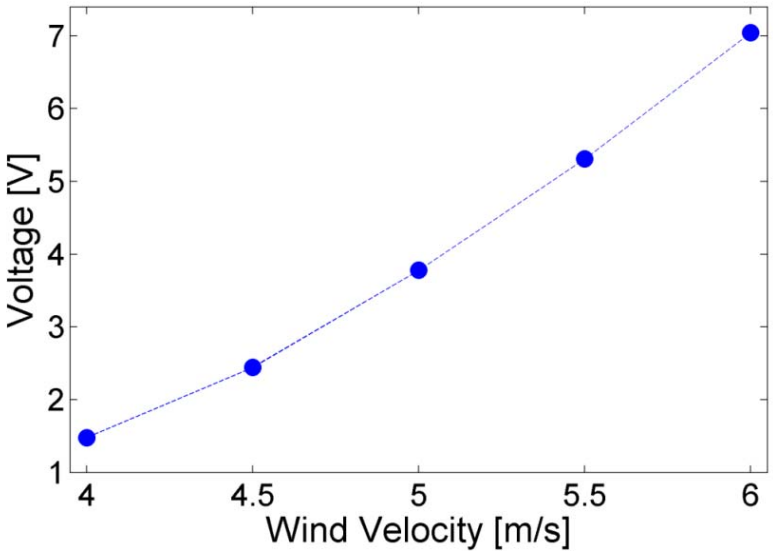

(a)

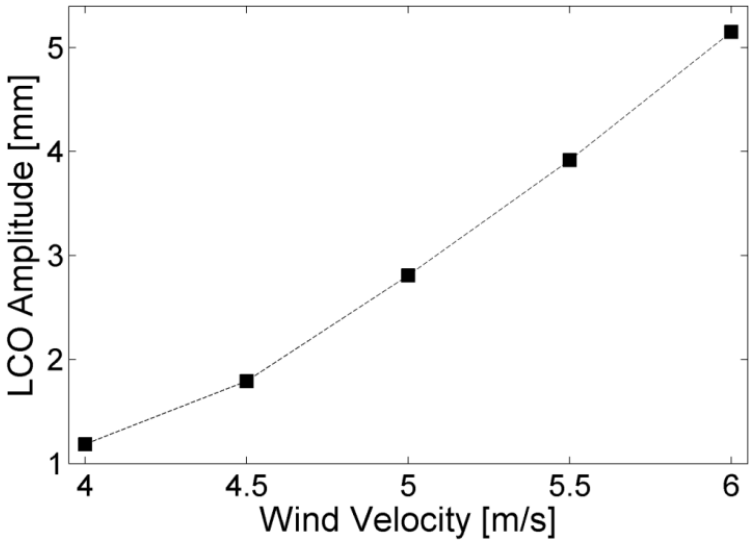

(b)

Figure 6.7: Mini GPEH (a) voltage vs wind velocity (b) LCO amplitude vs wind velocity

Tests were for open circuit loads from 4 - 6m/s wind velocity. Maximum voltage acquired is 7V at open circuit loads and 6m/s wind velocity. The mini GPEH will be viable as a flow sensing tool rather than energy harvesting. Moreover in Table 6.4 comparison of system properties for the different generations is given. Since

voltage was acquired at open circuit loads for the Mini GPEH the power density for the Mini GPEH does not suffice. Power density for the intermediate GPEH was highest (3.8mW/cm^3) indicating an array of miniature GPEHs is the better configuration for energy harvesting applications.

6.3 Flow sensing scheme

6.3.1 Passive control

The bio-inspired bluff body concept is introduced and further investigated to determine if there could be physical consequences due to miniaturization. Tip bluff bodies with wavy leading edges according to Table 6.5 and 6.6 are used to examine the effects of number of waves and wave amplitude on GPEH performance. Measured LCO amplitude and voltage are presented in Figure 6.8 and 6.9 respectively. The results show that the wavy leading edge can be used to determine the velocity for initiation of galloping for a GPEH. Figure 6.8 is a plot of GPEH with baseline and bluff bodies with properties in Table 6.5. Compared to the baseline bluff body; there is progressive reduction in lift and drag with reducing λ/h as noticed from the voltage and LCO amplitude plots. Interestingly, for $2.5 \leq \lambda/h \leq 1.25$ and $0.2 \leq A/\lambda \leq 0.1$ GPEH begins to gallop before baseline bluff body which implies an increased $A_{1;}$ while for $0.833 \leq \lambda/h \leq 0.625$ and $0.4 \leq A/\lambda \leq 0.3$

the velocity for initiation of galloping is higher than baseline. A similar trend is observed from results for bluff bodies in Table 6.6 where $\lambda/h = 1.25$ (2 full waves) is kept constant and wave amplitude is varied. It is seen from Figures 6.8 and 6.9 that for a GPEH with the same properties, we get 8 different U_0 by adjusting only the wavy leading edge of the bluff bodies. Furthermore, a good combination of wave steepness (A/λ) and wavelength (λ/h) will be required to achieve the desired U_0. For example, if $A/\lambda = 0.4$ the system shuts down at constant $\lambda/h = 1.25$ for wind velocity 10 m/s and 10.5 m/s (Figure 6.10b); whereas for reduced $\lambda/h = 0.625$ the GPEH will gallop at $A/\lambda = 0.4$ (Figure 6.10a).

Table 6.5: Bio-inspired Bluff Body Properties with constant amplitude

Length Parameters	Sine I	Sine II	Sine III	Sine IV
λ/h	2.5	1.25	0.833	0.625
A/λ	0.1	0.2	0.3	0.4

[M=7.7g, Sine # = number of full waves]

Table 6.6: Bio-inspired Bluff Body Properties with constant wavelength

Length Parameters	Sine II-3	Sine II-5	Sine II-7	Sine II-10
λ/h	1.25	1.25	1.25	1.25
A/λ	0.12	0.2	0.28	0.4

[M=7.7g, Sine #-# = number of full waves - wave amplitude in mm]

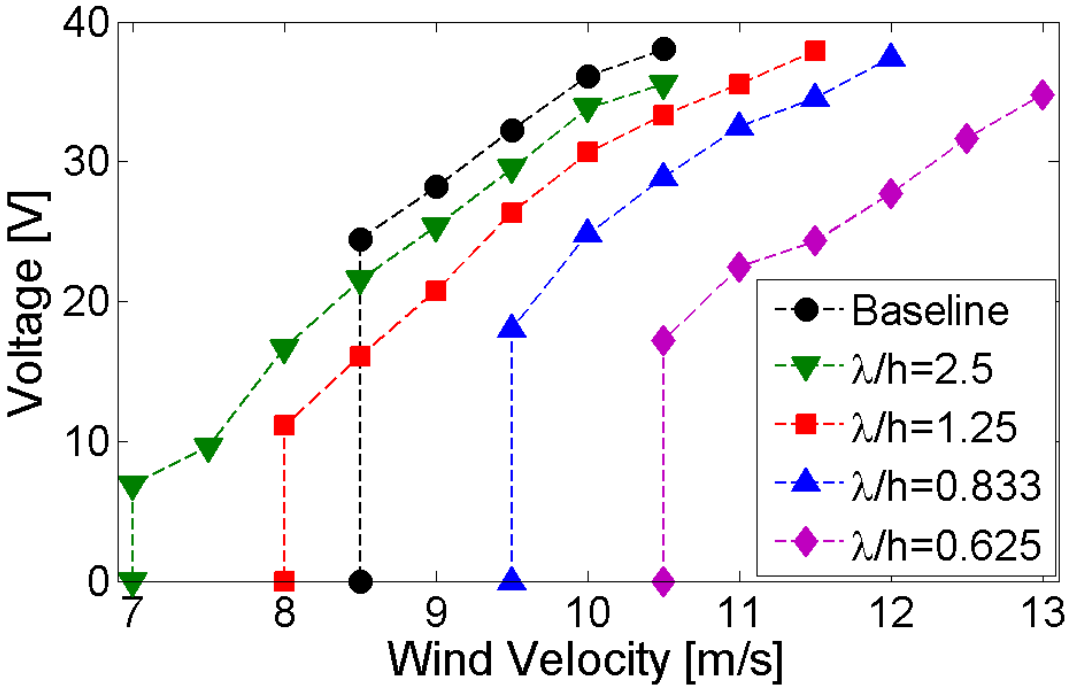

(a)

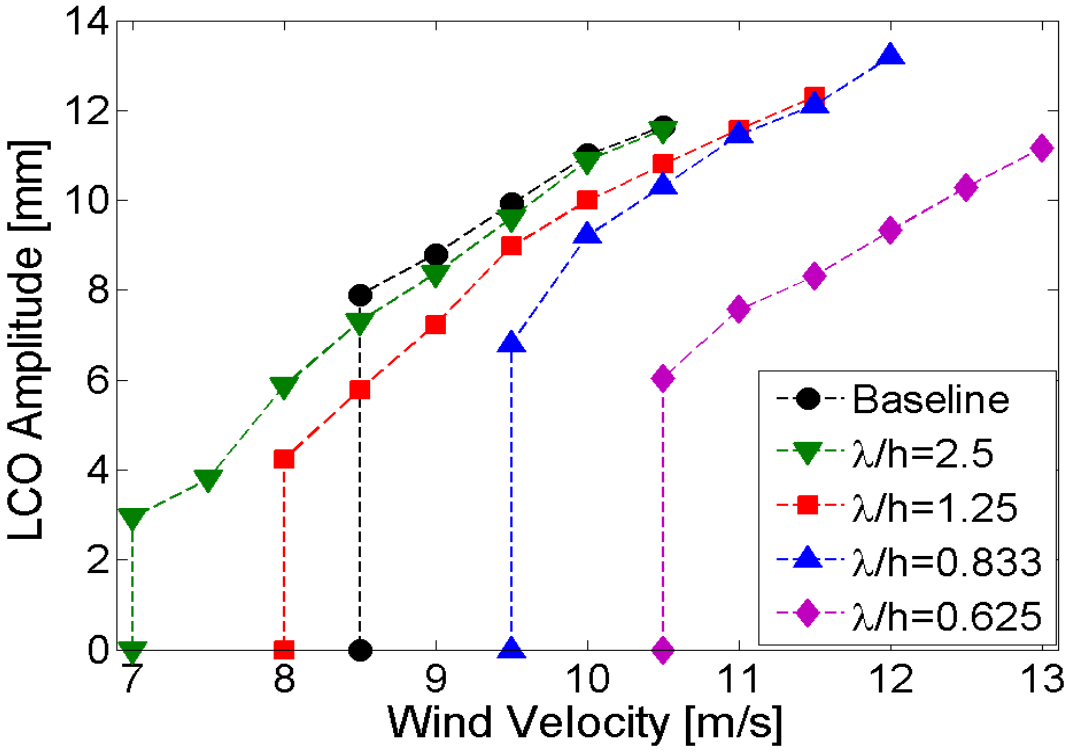

(b)

Figure 6.8: Bio-inspired bluff body (constant amplitude) (a) Voltage vs wind velocity (b) LCO vs wind speed

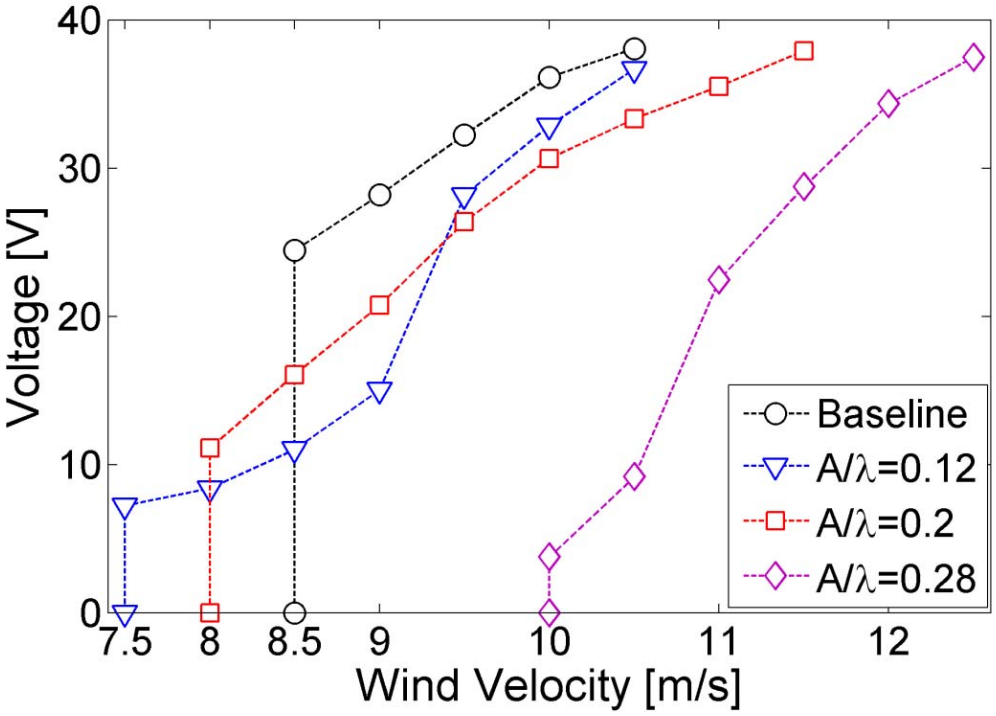

(a)

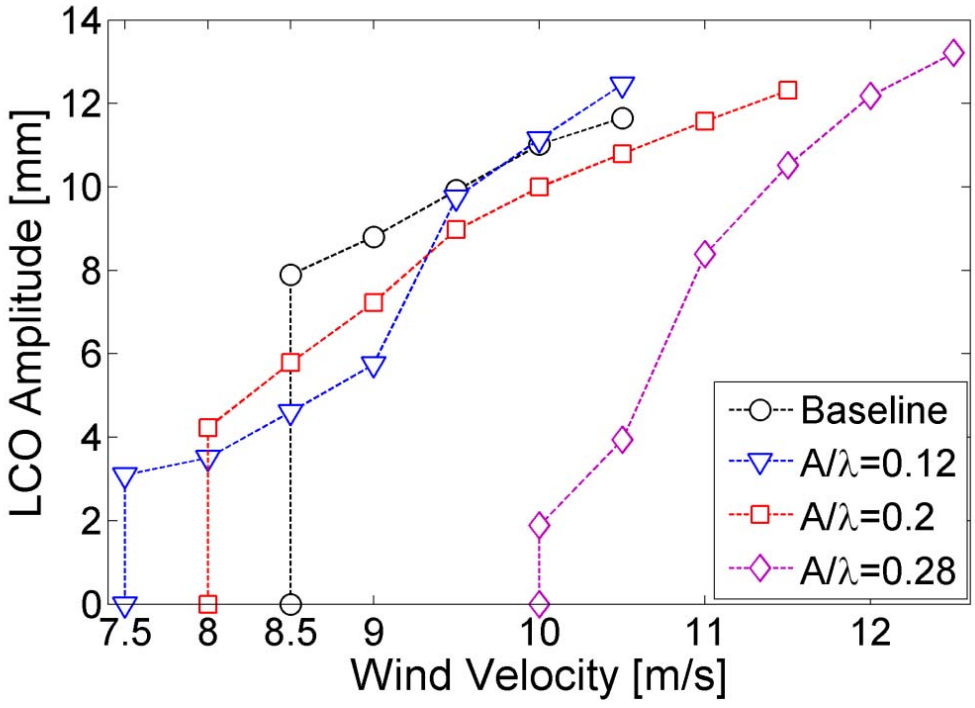

(b)

Figure 6.9: Bio-inspired bluff body (constant wavelength) (a) Voltage vs wind velocity (b) LCO vs wind speed

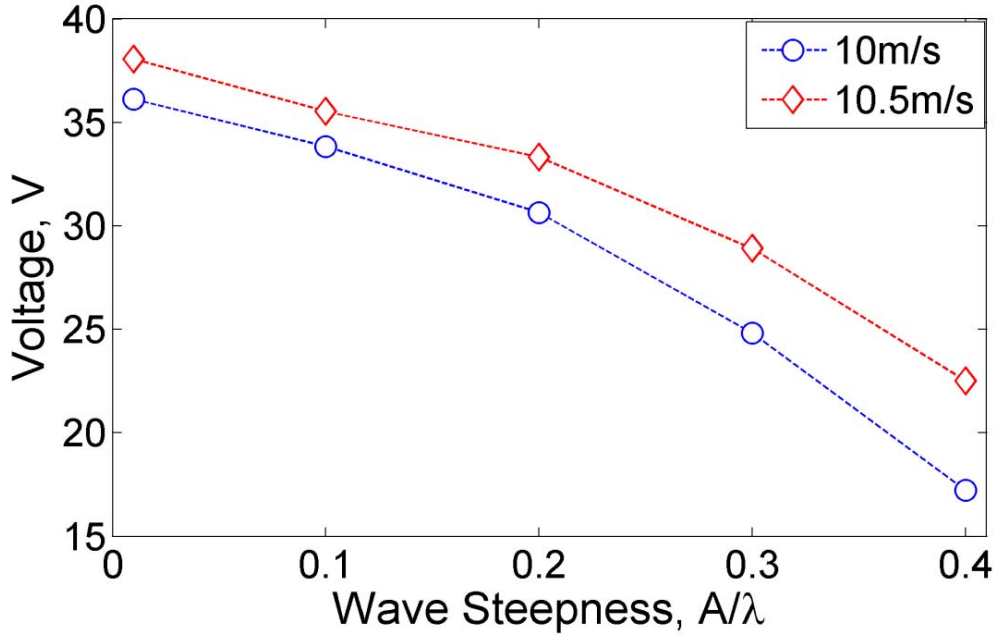

(a)

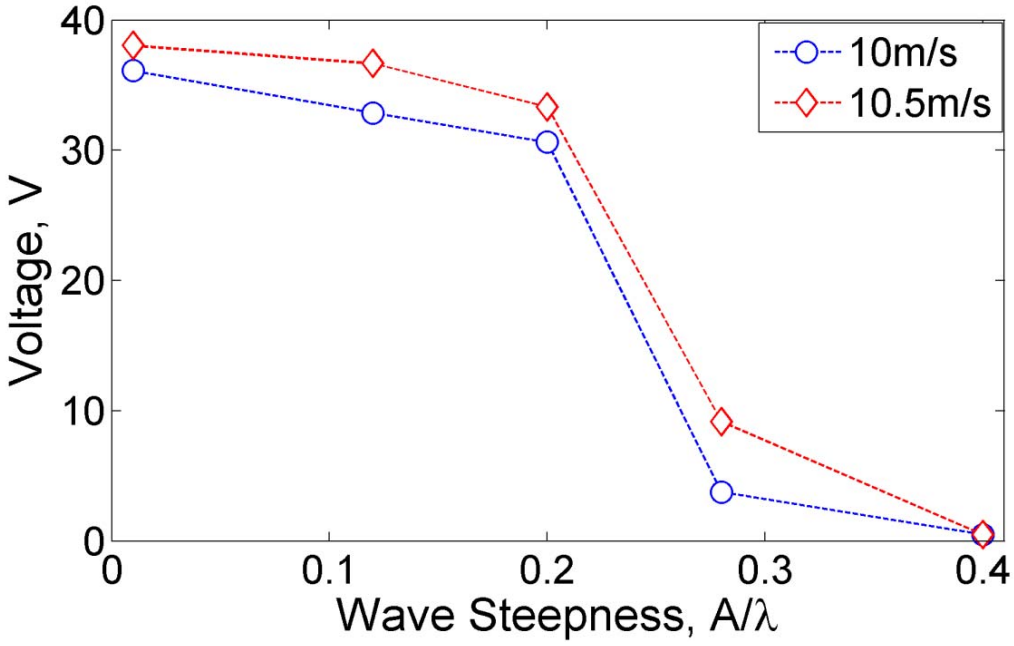

(b)

Figure 6.10: Measured data for bluff bodies variation with wave steepness (a) Varying λ/h (b) Constant λ/h

6.3.2 Airflow Sensing (Magnitude and Direction)

Most airflow measurements rely on some physical effect arising from motion. Three of such effects found suitable include; pressure changes with motion (pitot tube), consequent mechanical effects (wind vane anemometer, GPEH) and the rate of cooling of a hot body (hot wire anemometry) [100]. Generally, these instruments will have to be calibrated in an airstream whose speed can be measured and controlled by independent means. Therefore to apply the GPEH as an airflow measurement instrument, it has to be calibrated in the wind tunnel. Acquired voltage signal only is sufficient to relate the different wind velocity magnitude; therefore the mini GPEH is best suitable for low wind speed application. Since wind velocity is a vector, theoretically two sensors are sufficient to determine its magnitude and direction. A rosette of three sensors will be used to adequately determine the direction of the airflow (Figure 6.11). At equilibrium, each sensor at its referenced local coordinate is at a zero angle of attack with the incoming wind which induces maximum LCO amplitude. The angle θ is used to relate the sensed direction to the global coordinate of the array and the arrangement ensures a unique identity for the signals. To determine the wind direction a simple comparison of magnitude is done by each sensor with its adjacent sensors. Table 6.7 shows a case of magnitude comparison and the sensed direction according to

Figure 6.11 with the north sensor (N) as center. This enables the whole flow field to be captured with a resolution dependent on the value of θ which can be adjusted to fit the desired application. The stability of a square bluff body initially partially unstable at 0^o will become unstable at increased mean angle of attack until after 13.5^o when it becomes stable [82]. Therefore, a resolution of θ=15^o will ensure an adequate directional sensing using the GPEH rosette.

A fixture made to hold three mini GPEHs and allows for rotation is shown in Figure 6.12. The flow sensor array like its model must be sensitive enough to detect flow levels and distinguish from noise. To do this the system must have forms (Lock-in amplifier) of mechanical amplification and filtering to "lock" to the signal and "zoom in" to the source; also, arrays with identical elements can be used to suppress undesired signals. However, the UAH subsonic wind tunnel test section is small and not sufficient to carry out the directional flow sensing tests. Although, three identical Mini GPEHs were tested with all in the 0^o mean direction at 4m/s to show the time domain signals and frequency content (Figure 6.13). Such initial checks are required to determine the signal lock frequency, filtering and amplification needed.

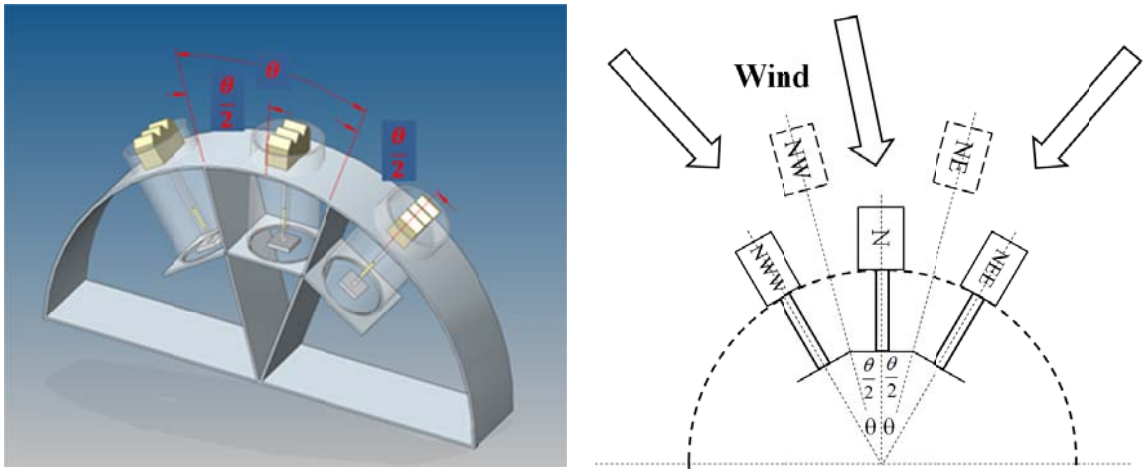

(a) (b)

Figure 6.11: Airflow direction sensing; (a) 3D CAD model (b) Schematic

Table 6.7: Air Velocity Measurement Scheme

Sensor	NWW	N	NEE	Sensed Direction
Magnitude	LOW	MAX	LOW	N
	LOW	MAX/MID	MID/MAX	NE
	LOW	LOW	MAX	NEE
	MID/MAX	MAX/MID	LOW	NW
	MAX	LOW	LOW	NWW

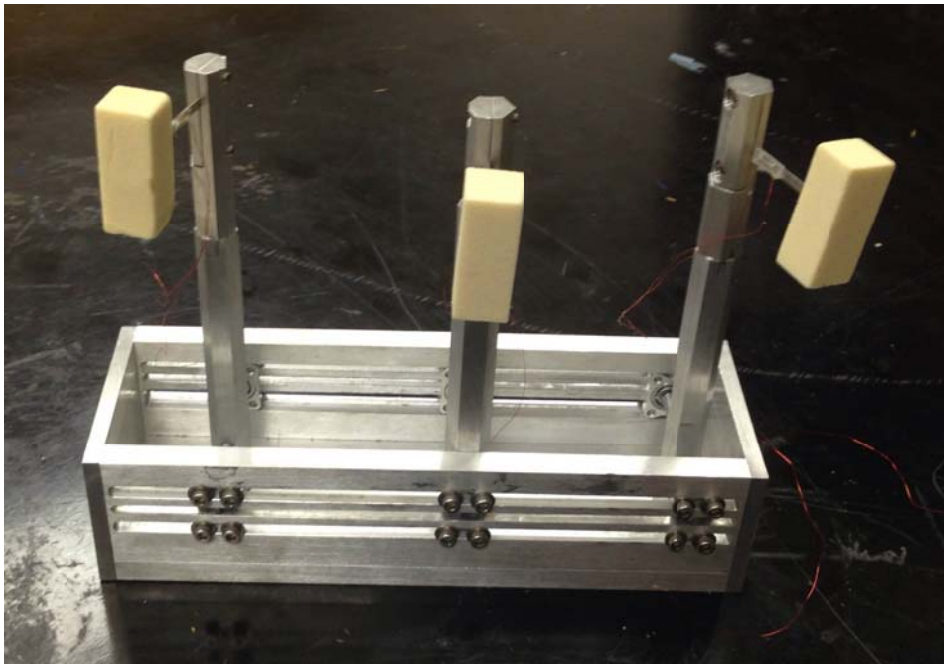

Figure 6.12:Mini GPEH rosette on fixture

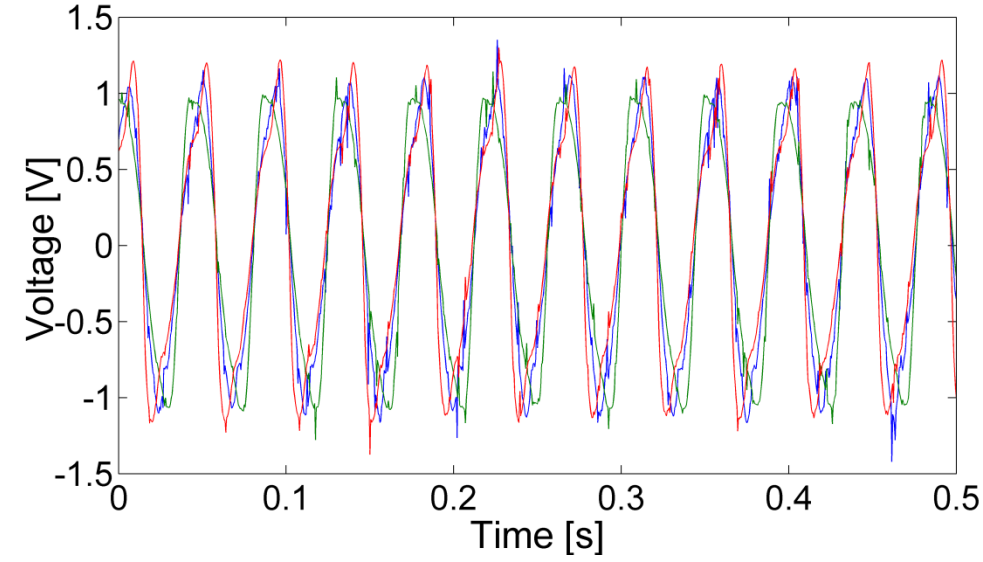

(a)

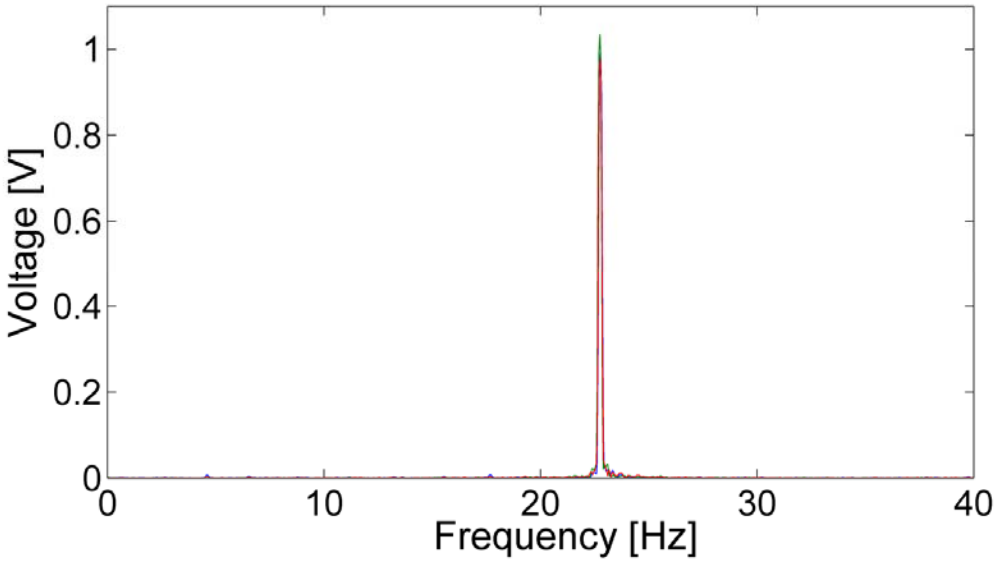

(b)

Figure 6.13: Acquired voltage signal for mini GPEH rosette; (a) Time domain (b) FFT

Chapter 7: Conclusion and Recommendation

This research work focused on the use of flow-induced vibration as a reliable alternative source of vibration for piezoelectric energy harvesters. A combination of analytical, numerical, and experimental efforts were applied in order to investigate this fully coupled aero-electro-mechanical system. Key conclusions for each aspect are summarized below.

7.1 Analytical and Numerical Model

Nonlinear models with linear motion and linear piezoelectricity assumed, and another with geometrically nonlinear motion and nonlinear piezoelectric constitutive relationship were developed. The asymptotic technique - Krylov–Bogoliubov first approximation method - was employed to obtain analytical approximate solutions. The GPEH performance in terms of the galloping velocity, LCO amplitude, voltage, current, and power was predicted for loads varying from short circuit to open circuit. LCO amplitude, voltage and power vary monotonically with wind velocity. Galloping velocity is highest and LCO amplitude lowest at matching loads due to additional positive damping. The hysteresis range is observed to occur at lower wind velocity than for a beam without piezoelectric sheets. Dimensionless formulation was used so that it is convenient to conduct

design, sizing, and performance evaluation for different GPEHs. Build up time to stationary oscillations vary inversely with initial wind speed. Voltage and power predictions were in good agreement with experiments. Some discrepancy in the prediction of LCO amplitude by the GPEH model with linear motion and linear piezoelectricity was noticed. The GPEH model with geometrical nonlinear motion and nonlinear piezoelectricity corrected this discrepancy due to additional damping introduced from piezoelectric material nonlinearity. Additionally, 2D numerical models to determine voltage for a GPEH, the vertical aerodynamic force coefficient and impact stresses on a piezoelectric beam impacting a bump stop were made with the FEA software COMSOL Multiphysics. Voltage results are in good agreement with experiments conducted and results for the aerodynamic model are consistent with experiments in literature. Only one inflexion point was noticed for the C_{FY} curve (I_T=0.05%) and it is observed that the C_{FY} curve loses its inflexion points with reduced peak amplitude occurring at lower angles of attack with increasing turbulence intensity.

7.2 Experimental Evaluations

Comprehensive tests on fabricated baseline GPEH and improved prototypes were conducted in the UAH subsonic wind tunnel. Peak 13mW power at 100kΩ optimal loads was acquired. System damping and LCO amplitude increase

monotonically with wind velocity but follow opposite trends with electrical resistance. Transient period was estimated and the state space plot of the response is discussed. Fatigue damage noticed after about 600k cycles of baseline GPEH oscillations prompted the addition of a bump stop to reduce large deflections noticed. Tests were then conducted by varying three bump stop design parameters – gap size, stop location and contact surface area. The optimal stop configuration was identified with substantial (70%) reduction in LCO amplitude and small (20%) trade off in voltage. Borrowing from tubercles on the leading edge of a humpback whale flipper, a square cross-section bluff body with sinusoidal waviness along the span of its leading edge was fabricated to evaluate the influence on the GPEH. Two dimensionless length scales – wave steepness (A/λ) and spanwise vertical ratio (λ/L) were varied during tests conducted. It was noticed that the bio-inspired bluff body can be used as passive control to tune galloping velocity. Therefore, for GPEH's with similar properties the velocity for the onset of galloping can be altered to fit desired wind speeds. Hitherto, this critical velocity depended on system mechanical damping and shape of the bluff body cross-section.

7.3 Applications

Using dimensionless variables an intermediate and mini GPEH were fabricated and tested to estimate system properties and analyze its viability as an array of sensors for various engineering applications. Their energy harvesting potential was compared to baseline GPEH and the measured data was used to validate model prediction. Power density for the intermediate GPEH was highest ($3.8 mW/cm^3$) indicating an array of miniature GPEHs is the better configuration for energy harvesting applications. Furthermore, the intermediate GPEH was used to demonstrate passive control; a GPEH was shown to start at 8 different wind speeds just by varying the dimensionless length scales of the bio-inspired bluff body. This is very important in the design of a GPEH as a flow sensor. Calibrated signals of a single GPEH can be used to relate airflow magnitude whereas a rosette design for airflow directional measurement is presented.

In summary, the GPEH concept developed in this effort provides a practical solution to harvest electricity from wind-induced vibration. It also provides a low-cost alternative to measure airflow magnitude and direction. To this end the objectives of this research work has been achieved.

7.4 Recommendations for Future Research

Essentially, experimental evaluations conducted in this study provides a background for further research into the development of models for the coupled aero-electro-mechanical system especially with the added complexities of the improved GPEH designs. The coupled equations for the GPEH with the bio-inspired bluff body will require 3D analysis. Therefore, if the quasi-static hypothesis is employed experiments to determine C_{FY} (i.e. C_L and C_D) curve for a square cross-section bluff body with spanwise sinusoidal waviness will be conducted.

CFD analysis will be carried out to determine the vertical aerodynamic force coefficients and also explore the Kármán vortex wake in the near and intermediate wake structure for the bio-inspired bluff body. A parameter study on the effects of the dimensionless length scales of the bluff body at different mean angle of attack will be useful to further investigate the bio-inspired bluff body as passive control. To optimize the GPEH with a bump stop design, a model to incorporate impact dynamics will be developed, further investigate the effect of impact stresses on harvested energy and conduct a parametric study of the bump stop design parameters.

To exploit an array of GPEH to harvest wind energy, the effect on the aerodynamics due to interaction between adjacent prototypes will have to be explored. For example what is the minimum allowable distance between prototypes and what is the influence on the onset of galloping? Further investigations and optimization can be carried out to improve the power density of the GPEH, such as a composite bluff body to exploit bluff body inertial and composite piezoelectric beam with sandwiched piezoelectric materials.

REFERENCES

[1] S. Roundy and P. K. Wright, "A piezoelectric vibrational based generator for wireless electronics," *Smart Mater. Struct,* vol. 13, pp. 1131-42, 2005.

[2] D. J. Inman and B. L. Grisso, "Towards autonomous sensing," in *Proceedings of SPIE Smart Structures Materials Conference*, San Diego, CA 61740T, 2006.

[3] P. Muralt, "Ferroelectric thin films for micro-sensors and actuators: a review," *J. Micromech. Microeng.,* vol. 10, p. 136–46, 2000.

[4] H. A. Sodano, G. Park and D. J. Inman, "Estimation of electric charge output for piezoelectric energy harvesting," vol. 40, pp. 49-58, 2004a.

[5] H. A. Sodano , G. Park and D. J. Inman, "A review of power harvesting from vibration using piezoelectric materials," *Shock Vib. Dig.,* vol. 36, p. 197–206, 2004b .

[6] A. Erturk and D. J. Inman, Piezoelectric Energy Harvesting, New York: UK: Wiley, 2011.

[7] R. Blevins, Flow-Induced Vibration, Malabar, FL: Krieger Publishing Company., 2001.

[8] D. L. Devoe and A. P. Pisano, "Modeling and optimal design of piezoelectric cantilever microactuators," *Journal of Microelectromechanical Systems,* vol. 6, no. 3, p. 266–270, 1997.

[9] N. E. DuToit, B. L. Wardle and S. Kim, "Design considerations for MEMS-scale piezoelectric mechanical vibration energy harvesters," *Integrated Ferroelectrics,* vol. 71, no. 1, p. 121–160, 2005.

[10] W. J. Choi et al., "Energy harvesting MEMS device based on thin film piezoelectric cantilevers," *Journal of Electroceramics,* vol. 17, no. (2–4), p. 543–548, 2006.

[11] K. A. Cook-Chennault et al., "Powering MEMS portable devices—a review of nonregenerative and regenerative power supply systems with emphasis on piezoelectric energy harvesting systems," *Smart Materials and Structures,* vol. 17: 043001, 2008.

[12] G. K. Ottman et al., "Adaptive piezoelectric energy harvesting circuit for wireless remote power supply," *IEEE Transactions on Power Electronics,* vol. 17, no. 5, p. 669–676, 2002.

[13] A. Badel et al., "Efficiency enhancement of a piezoelectric energy harvesting device in pulsed operation by synchronous charge inversion," *Journal of Intelligent Material Systems and Structures,* vol. 16, no. 10, p. 889–901, 2005.

[14] J. Ajitsaria et al., "Modeling and analysis of a bimorph piezoelectric cantilever beam for voltage generation," *Smart Materials and Structures,* vol. 16, pp. 447-454, 2007.

[15] F. Goldschmidtboeing and P. Woias, "Characterization of different beam shapes for piezoelectric energy harvesting," *J. Micromech. Microeng,* vol. 18, no. 104013(7pp), 2008.

[16] A. Erturk and D. J. Inman, "On mechanical modeling of cantilevered piezoelectric vibration energy harvesters," *Journal of Intelligent Materials Systems and Structures,* vol. 19, pp. 1311-15, 2008.

[17] S. N. Chen, G. J. Wang and M. C. Chien, "Analytical modeling of piezoelectric vibration-induced micro power genarator," *Mechatronics,* vol. 16, no. 7, pp. 379-387, 2006.

[18] J. H. Lin et al., "Modeling and simulation of piezoelectric MEMS energy harvesting device," *Integrated Ferroelectrics,* vol. 95, no. 1, pp. 128-141, 2007.

[19] F. Lu, H. P. Lee and S. P. Lim, "Modeling and analysis of micro piezoelectric power generators for micro-electromechanical-systems applications," *Smart Materials and Structures,* vol. 13, no. 1, pp. 57-63, 2004.

[20] Z. K. Kusculuoglu, B. Fallahi and T. J. Royston, "Finite element model of a beam with piezeolectric patch actuator," *Journal of Sound and Vibration,* vol. 276, no. (1-2), pp. 27-44, 2004.

[21] A. Benjeddou , M. A. Trindade and R. Ohayon, "A unified beam finite element model for extension and shear piezoelectric actuation mechanisms," *Journal of Intelligent Material Systems and Structures,* vol. 8, no. 12, pp. 1012-1025, 1997.

[22] G. Wang, "Analysis of bimorph piezoelectric beam energy harvester using Timoshenko and Euler-Bernoulli beam theory," *Journal of Intelligent Material*

Systems and Structures , vol. 24, no. 2, p. 226–239, 2013.

[23] K. H. Mak et al., "Performance of a cantilever piezoelectric energy harvester impacting a bump," *J. Sound Vib.,* vol. 330, p. 6184–202, 2011.

[24] V. R. Challa et al., "A vibration energy harvesting device with bidirectional resonance frequency tunability," *Smart Materials Structures,* vol. 17, no. 015035, pp. 1-10, January 2008.

[25] S. Zhou et al., "Enhanced broadband piezoelectric energy harvesting using rotatable magnets," *Applied Physics Letters,* vol. 102, no. 17, pp. 1-4, 2013.

[26] H. Xue, Y. Hu and Q.-M. Wang, "Broadband piezoelectric energy harvesting devices using multiple bimorphs with different operating frequencies," *IEEE Transactions on Ultarsonics, Ferroelectrics, and Frequency Control,* vol. 55, no. 9, pp. 2104-2108, 2008.

[27] A. Mehmood, " Piezoelectric energy harvesting from vortex-induced vibrations of circular cylinder," *J. Sound Vib.,* vol. 332, p. 4656–67, 2013.

[28] A. Abdelkefi, M. R. Hajj and A. H. Nayfeh, "Phenomena and modeling of piezoelectric energy harvesting from freely oscillating cylinders," *Nonlinear Dyn.,* vol. 70, p. 1377–88, 2012.

[29] H. D. Akaydin, N. Elvin and Y. Andrepoulos, "The performance of a self-excited fluidic energy harvester," *J. Smart Mater. Struct.,* vol. 21, no. 025007, 2012.

[30] M. Bryant and E. Garcia, "Modeling and testing of a novel aeroelastic flutter energy harvester," *J. Vib. Acoust,* vol. 133, no. 0110005, 2011.

[31] A. Erturk et al., "On the energy harvesting potential of piezoaeroelectric systems," vol. 96, no. 184103, p. Applied Physics Letters, 2010.

[32] C. De Marqui Jr, A. Erturk and D. J. Inman, "Piezoaeroelastic modeling and analysis of a generator wing with continuous and segmented electrodes," *J. Intell. Mater. Syst. Struct.,* vol. 21, p. 983–93, 2011.

[33] S. D. Kwon, "A T-shaped piezoelectric cantilever for fluid energy harvesting," *Appl. Phys. Lett.,* vol. 97, no. 164102, 2010.

[34] S. Li , J. Yuan and H. Lipson, "Ambient wind energy harvesting using cross-flow fluttering," *J. Appl. Phys.,* vol. 109, no. 026104, 2011.

[35] J. Sirohi and R. Mahadik, "Piezoelectric wind energy harvester for low-power sensor," *J. Intell. Mater. Syst. Struct.,* vol. 22, p. 2215–28, 2011.

[36] J. Sirohi and R. Mahadik , "Harvesting wind energy using a galloping piezoelectric beam," *J. Vib. Acoust.,* vol. 134, no. 011009, 2012.

[37] A. Abdelkefi, Z. Yan and M. R. Hajj , "Modeling and nonlinear analysis of piezoelectric energy harvesting for transverse galloping of bluff bodies," *Journal of Smart Materials and Structures,* vol. 22, no. 025016 (10pp), 2013.

[38] A. Abdelkefi, M. R. Hajj and A. H. Nayfeh, "Power harvesting from transverse galloping of a square cylinder," *Nonlinear Dyn.,* vol. 70, p. 1355–63, 2012.

[39] L. Zhao, L. Tang and Y. Yang, "Small wind energy harvesting from galloping using piezoelectric materials," in *ASME Conf. Smart Materials, Adaptive Structures Intelligent Systems proc.*, Georgia, USA, 19–21 September, 2012.

[40] D. M. Bushnell and K. J. Moore, "Drag reduction in nature," *Annual Review of Fluid Mechanics,* vol. 23, p. 65–79, 1991.

[41] Y. F. Lin et al., "Numerical study of flows past airfoils with wavy surfaces," *Journal of Fluid and Structures,* vol. 36, p. 136–148, 2013.

[42] A. F. Abdel Gawad, "Numerical simulation of the effect of leading-edge tubercles on the flow characteristics around an airfoil," in *Proceedings of the ASME 2012 International Mechanical Engineering Congress and Exposition*, Houston Texas, USA, 9-15 Nov. 2012.

[43] P. W. Bearman and J. C. Owen, "Reduction of bluff-body drag and suppression of vortex shedding by the introduction of wavy separation lines," *Journal of Fluids and Structures,* vol. 12, p. 123–130, 1998.

[44] R. M. Darekar and S. J. Sherwin, "Flow past a square-section cylinder with a wavy stagnation face," *Journal of Fluid Mechanics,* vol. 426, pp. 263-295, 2001.

[45] A. Dombre, H. Hangan and B. J. Vickery, "Wake control based on spanwise sinusoidal perturbations," *AIAA Journal,* vol. 44, no. 3, pp. 485-492, 2006.

[46] K. Lam and Y. F. Lin, "Effects of wavelength and amplitude of a wavy cylinder in cross-flow at low Reynolds numbers," *Journal of Fluid Mechanics,*

vol. 620, p. 195–220, 2009.

[47] N. Tombazis and P. W. Bearman, "A study of three-dimensional aspects of vortex shedding from a bluff body with a mild geometric disturbance," *Journal of Fluid Mechanics,* vol. 330, p. 85–112, 1997.

[48] J. Curie and P. Curie, "Development, via compression, of electric polarization in hemihedral crystals with inclined faces," *Bulletin de la Societe de Minerologique de France,* vol. 3, pp. 90-93, 1880.

[49] T. Ikeda, Fundamentals of Piezoelectricity, New York: Oxford University Press, 1990.

[50] W. G. Cady, Piezoelectricity, New York: Dover, 1964.

[51] W. P. Mason, Crystal physics of interaction processes, New York: Academic Press, 1966.

[52] L. F. Brown and G. R. Harris, "Introduction to the Special Issue on the 30th Anniversary of the Discovery of Piezoelectric PVDF," *IEEE transactions on ultrasonics, ferroelectrics, and frequency control,* vol. 47, no. 6, pp. 1275-1276, November 2000.

[53] B. Jaffe, R. S. Roth and S. Marzullo, "Properties of piezoelectric ceramics in the solid-solution series lead titanate-lead zirconate-lead oxide: Tin oxide and lead titanate-lead hafnate," *Journal of Research of the National Bureau of Standards,* vol. 55, p. 239, 1955.

[54] M. Umeda, K. Nakamura and S. Ueha, "Analysis of transformation of mechanical impact energy to electrical energy using a piezoelectric vibrator," *Japanese Journal of Applied Physics,* vol. 35, p. 3267–3273, 1996.

[55] J. Kymissis et al., "Parasitic power harvesting in shoes," in *Second IEEE International Symposium on wearable Computers*, Pittsburg, PA, October 19-20th 1998.

[56] M. Kimura, "Piezoelectric Generation Device". U.S. Patent 5801475, 1 September 1998.

[57] T. Starner, "Human-Powered Wearable Computing," *IBM Systems Journal,* vol. 35, pp. 618-629, 1996.

[58] M. Umeda, K. Nakamura and S. Ueha, "Energy Storage Characteristics of a PiezoGenerator Using Impact Induced Vibration," *Japanese Journal of Applied Physics,* Vols. Vol. 35, Part 1, no. 5B, pp. 3146-3151, 1997.

[59] H. A. Sodano , G. Park and D. J. Inman, "Estimation of electric charge output for piezoelectric energy harvesting," *Strain,* vol. 40, p. 49–58, 2004c.

[60] H. F. Tiersten, Linear Piezoelectric Plate Vibrations, New York: Plenum Press, 1969.

[61] IEEE, "IEEE standard on Piezoelectricity," *ANSI/IEEE std,* vol. 176, 1987.

[62] U. von Wagner and P. Hagedorn, "Piezo-beam systems subjected to weak electric field: Experiments and modeling of non-linearities," *Journal of Sound and Vibration,* vol. 256, no. 5, p. 861–872, 2002.

[63] M. N. Nguyen, "Nichtlineares dynamisches Verhalten von Piezo-Balken-Systemen bei schwachem elektrischem Feld," Doctoral Dissertation, Technische Universit¨at Darmstadt, 1999, GCA Verlag, Herdecke, Germany, 2000.

[64] S. Stanton et al., "Nonlinear piezoelectricity in electroelastic energy harvesters: modeling and experimental identification," *Journal of Applied Physics,* vol. 108, no. 074903, 2010.

[65] G. R. Cowper, "On the accuracy of Timoshenko's beam theory," *Journal of the Engineering Mechanics Division,* vol. 94, pp. 1447-1453, 1968.

[66] S. M. Han, H. Benaroya and T. Wei, "Dynamics of transversely vibrating beams using four engineering theories," *Journal of Sound and Vibration,* vol. 225, no. 5, pp. 935-988, 1999.

[67] S. P. Timoshenko, "On the correction for shear of the differential equation for transverse vibrations of prismatic bars," *Philosophical Magazine and Journal of Science,* vol. 41, pp. 744-747, 1921.

[68] G. R. Cowper, "The shear coefficient in Timoshenko's beam theory," *Journal of Applied Mechanics,* vol. 33, pp. 335-340, 1966.

[69] I. H. Shames and C. L. Dym, Energy and Finite Element Methods in Structural Mechanics, New York: McGraw-Hill, 1985.

[70] K. D. Hjelmstad, Fundamentals of Structural Mechanics, 2nd ed., New York: Springer, 2005.

[71] S. N. Mahmoodi, M. F. Daqaq and N. Jalili, "On the nonlinear-flexural response of piezoelectric driven microcantilever sensors," *Sensors and Actuators A,* vol. 153, pp. 171-179, 2009.

[72] M. I. Friswell et al., "Nonlinear piezoelectric vibration energy harvesting from a vertical cantilever beam with tip mass," *Journal of intelligent material systems and structures,* vol. 23, no. 13, pp. 1505-1521, 2012.

[73] M. P. Paidoussis, Fluid-Structure Interactions: Slender Structures and Axial Flow, vol. 1, San Diego: Academic Press, 1998.

[74] A. Roshko, "On the drag and vortex shedding frequency of two-dimensional bluff bodies," National Advisory Committee for Aeronautics Report NACA TM 3159, 1954.

[75] A. Roshko, "Experminents on the flow past a circular cylinder at very high reynolds number," *Journal of Fluid Mechanics,* vol. 10, pp. 345-356, 1961.

[76] O. M. Griffin, "Universal similarity in the wakes of stationary and vibratiing bluff stuctures," *Journal of Fluids Engineering,* vol. 103, pp. 52-58, 1981.

[77] T. Sarpkaya, "Vortex-induced Oscillations," *Journal of Applied Mechanics,* vol. 46, pp. 241-258, 1979.

[78] R. W. Miller, Flow measurement Engineering Handbook 2d ed.,, New York: McGraw-Hill, 1989.

[79] T. T. Yeh, B. Robertson and W. M. Mattar, "LDV measurements near a vortex shedding strut mounted in a pipe," *Journal of Fluids Engineering,* vol. 105, pp. 185-194, 1983.

[80] M. J. Casarella and M. Parsons, "A survey on investigations on the configuration and motion of cable systems under hydrodynamic loading," *Marine Technology Society Journal,* vol. 4, no. 4, pp. 27-44, 1970.

[81] E. Konstantinidis and D. Bouris , "Bluff Body Aerodynamics and Wake Control," in *Applied Aerodynamics*, Rijeka Croatia, InTech, 2012, pp. 63-78.

[82] S. C. Luo et al., "Stability of translational galloping vibration of cylinders at different mean angles of attack," *Journal of Sound and Vibration,* vol. 215,

pp. 1183-1194, 1998.

[83] G. V. Parkinson, "Mathematical models of flow-induced vibration of bluff bodies," in *IUTAM-IAHR Symposium - Flow-Induced Structural Vibration*, Karlsruhe Germany, 1972.

[84] M. Novak and H. Tanaka, "Effect of turbulence on galloping instability," *Journal of the Engineering Mechanics Division,* vol. 100, pp. 27-47, 1974.

[85] J. P. Den Hartog, Mechanical Vibrations, New York: Dover Publications Inc, 1956.

[86] G. Alonso , J. Meseguer and I. Perez-Grande, "Galloping stability of triangular cross-sectional bodies: A systematic approach," *Journal of Wind Engineering and Industrial Aerodynamics,* vol. 95, pp. 928-940, 2007.

[87] F. Ewere and G. Wang, "Performance of galloping piezoelectric energy harvesters," *Journal of Intelligent Material Systems and Structures,* vol. 25, no. 14, pp. 1693-1704, 2013.

[88] F. Ewere, G. Wang and B. Cain, "Experimental investigation of galloping piezoelectric energy harvesters with square bluff bodies," *Smart Materials and Structures,* vol. 23, no. 104012, 2013.

[89] G. V. Parkinson and J. D. Smith, "The Square Prism as an Aeroelastic Nonlinear Oscillator," *Quart. J. Mech. Appl. Math,* vol. 17, no. 2, pp. 225-239, 1964.

[90] M. Novak , "Aeroelastic Galloping of Prismatic Bodies," *Journal of the Engineering Mechanics Division,* vol. 95, no. 1, pp. 115-142, 1969.

[91] S. C. Luo, Y. T. Chew and Y. T. Ng, "Hysteresis phenomenon in the galloping oscillation of a square cylinder," *Journal of Fluids and Structures,* vol. 18, pp. 103-118, 2003.

[92] A. Barrero-Gil, A. Sana-Andres and G. Alonso, "Hysteresis in Transverse Galloping: The Role of the Inflection Points," *Journal of Fluids and Structures,* vol. 25, no. 6, pp. 1007-1020, 2009.

[93] A. Barrero-Gil , G. Alonso and A. Sanz-Andres , "Energy harvesting from transverse galloping," *Journal of Sound and Vibration,* vol. 329, no. 14, p. 2873–2883, 2010.

[94] P. P. Sullivan, "Aeroelastic galloping of tall structures in simulated winds," M.A.Sc. Thesis, Dept. of Mechanical Engineering, Univ. of British Columbia, Canada, 1977.

[95] N. Krylov and N. Bogoliubov, Introduction to Nonlinear Mechanics., Princeton, NJ: Princeton University Press, 1947.

[96] S. Stanton et al., "Resonant manifestation of intrinsic nonlinearity with electroelastic micropower generators," *Applied Physics Letters,* vol. 97, no. 254101, 2010.

[97] SirohiJ and I. Chopra, "Fundamental understanding of piezoelectric strain sensors," *Journal of Intelligent Materials Systems and Structures ,* vol. 11, pp. 246-257, 2001.

[98] M. A. Wawzonek, "Aeroelastic behavior of square section prisms in uniform flow," M.A.Sc Thesis, Department of Mechanical Engineering, University of British Columbia Canada, 1979.

[99] A. Laneville, "Effects of turbulence on wind induced vibrations of bluff cylinders," Ph.D. Thesis, Dept. of Mechanical Engineering , Univ. of British Columbia, Vancouver, Canada, 1973.

[100] E. Ower and R. C. Pankhurst, The measurement of air flow, 4th ed., Oxford, Great Britain: Pergamon Press Ltd, 1966.